HETEROGENEOUS ICE NUCLEATION

LABORATORY FREEZING RESULTS AND TESTING DIFFERENT SCHEMES TO DESCRIBE ICE NUCLEATION IN ATMOSPHERIC MODELS

by

MICHAEL JAMES WHEELER

B. Sc. Honours, Acadia University, 2006

A THESIS SUBMITTED IN PARTIAL FULFILLMENT
OF THE REQUIREMENTS FOR THE DEGREE OF

DOCTOR OF PHILOSOPHY

in

THE FACULTY OF GRADUATE AND POSTDOCTORAL STUDIES
(Chemistry)

THE UNIVERSITY OF BRITISH COLUMBIA
(Vancouver)

July 2015

Abstract

Ice nucleation occurs throughout the atmosphere. Some atmospheric ice particles are formed through nucleation on insoluble atmospheric aerosols known as ice nuclei (IN). The abundance and chemical composition of these IN affect the properties of clouds and in turn the radiative balance of the Earth through the indirect effect of IN on climate. The indirect effect of IN on climate is one of the least understood topics in climate change. A better understanding of ice nucleation and better capabilities to parameterize ice nucleation are needed to improve the predictions of the effect of IN on climate.

Using a temperature and humidity controlled flow cell coupled to an optical microscope, the ice nucleation properties of three different mineral dust particles are examined in two different freezing modes. Results showed that the freezing ability of supermicron dust particles is lower than that of submicron dust particles of the same type. These freezing results along with literature freezing results of nine biological aerosol particles are used to evaluate different schemes used to parameterize ice nucleation in atmospheric models. These schemes are evaluated based on the ability to reproduce the laboratory freezing results. It was found that a single parameter scheme based on classical nucleation theory was unable to reproduce the freezing results of all particles studied. However, more complex schemes were able to reproduce the freezing results.

The results in this thesis can be used by atmospheric modellers to improve predictions of mixed-phase and ice clouds and climate change.

Preface

Chapters 3 & 4 are co-authored peer-reviewed journal articles and the results from Chapter 5 are being prepared for submission to a peer-reviewed journal as a co-authored article. The details of my contribution to each chapter is provided below.

Chapter 3 (first author on published journal article): M. J. Wheeler and A. K. Bertram. Deposition nucleation on mineral dust particles: A case against classical nucleation theory with the assumption of a single contact angle. *Atmospheric Chemistry and Physics*, 12(2):1189–1201, January 2012. doi: 10.5194/acp-12-1189-2012. URL http://www.atmos-chem-phys.net/12/1189/2012/

- Formulated the research question and designed the research project with my supervisor.
- Performed all of the ice nucleation experiments.
- Performed all of the size measurements of the dust particles.
- Performed all of the data analysis.
- Developed algorithms to fit experimental data to the four schemes used in the chapter.
- Performed the fitting of the experimental data.
- Prepared all of the figures for the publication.
- Shared writing of the text in the publication with my supervisor.

Chapter 4 (first author on published journal article): M. J. Wheeler, R. H. Mason, K. Steunenberg, M. J. Wagstaff, C. Chou, and A. K. Bertram. Immersion freezing of supermicron mineral dust particles: Freezing results, testing different schemes for describing ice nucleation results, and ice nucleation active site densities. *Journal of Physical Chemistry A*, 119(19): 4358–4372, 2015b. doi: 10.1021/jp507875q

- Formulated the research question and designed the research project with my supervisor.
- Performed the ice nucleation experiments with R. H. Mason, K. Steunenberg, and M. J. Wagstaff.
- Performed analysis of ice nucleation experiments with R. H. Mason, K. Steunenberg, and M. J. Wagstaff.
- Adapted fitting algorithms from Chapter 3 for immersion freezing and performed all fitting of experimental data.
- Prepared all the figures for the publication.
- Shared the writing of the text in the publication with Dr. C. Chou and my supervisor.
- Additional contributions:
  - D. Horne provided scanning electronc microscopy (SEM) imaging of dust particles

Chapter 5 (first author on article under preparation for submission to peer-reviewed journal): M. J. Wheeler, D. I. Haga, R. H. Mason, V. E. Irish, M. J. Wagstaff, R. Iannone, and A. K. Bertram. Testing different schemes for describing immersion freezing of water drops containing primary biological aerosol particles. 2015a

- Formulated the research question and designed the research project with my supervisor.
- Performed fitting analysis of ice nucleation data.
- Prepared the figures for the publication.

- Shared the writing of the text with my supervisor.
- Additional contributions from co-authors:
  - Dr. D. I. Haga, R. H. Mason, M. J. Wagstaff, Dr. R. Iannone and I performed ice nucleation experiments on fungal spores and bacteria used in the analysis here.
  - Dr. D. I. Haga and M. J. Wagstaff performed data analysis of ice nucleation experiments from Haga et al. [2013].
  - Dr. D. I. Haga, M. J. Wagstaff and V. E. Irish performed data analysis of ice nucleation experiments from Haga et al. [2015].

Table of contents

List of tables

List of figures

List of symbols

A surface area of heterogeneous IN

A_1 fitting parameter for deterministic scheme

A_2 fitting parameter for deterministic scheme

A_α area of active site with contact angle α

A_{avg} surface area of an average particle

A_{hom} homogeneous nucleation pre-exponential factor

A_p surface area of a particle

A_{single} area of a single active site

A_{total} total surface area available for nucleation

α contact angle

$\Delta\alpha$ width of an individual active site bin

α_i contact angle of single active site

b fitting parameter for active site scheme

β_1 fitting parameter for active site scheme

β_2 fitting parameter for active site scheme

χ^2_{red} reduced chi-squared

D particle diameter

$\bar{D}_g$ geometric mean diameter

f_d fraction of drops frozen

$f_{\text{het}}(\alpha)$ contact parameter for heterogeneous nucleation/freezing

ΔF_{diff} diffusion free energy

ΔG_{act} critical free energy to cluster formation

ΔG_{cl} free energy of cluster formation

ΔG_s free energy of new surface formation

ΔG_v free energy of bulk water/ice formation

h Planck's constant

j_0 pre-exponential factor for heterogeneous nucleation

j_{het} heterogeneous nucleation rate

j_{hom} homogeneous nucleation rate constant

k Boltzmann constant

μm micrometer

μ_α mean of normal distribution of contact angles

μ_i chemical potential of the ice phase

μ_v chemical potential of the vapour phase

n number of particles per drop

n_{ice} number density of water molecules at the ice-water interface

n_{cl} number of molecules in a cluster

n_d number of drops

n_i number of active sites on a single particle

$\bar{n}_i$ average number of active sites

n_{max} maximum number of particles observed per drop

n_s surface density of active sites

n_{site} number of active sites on a particle

N_{total} total number of particles

N_u number of unfrozen particles/drops

N_0 total number of particles/drops

N_f number of frozen particles/drops

$\frac{N_f}{N_0}$ fraction of particles/drops nucleated

N_i molecular concentration of ice

nm nanometer

v_i molecular volume of ice

ω number of nucleation events

$P(A_i)$ probability of a drop containing surface area A_i

$p(\alpha)$ probability density function of normal distribution

$\bar{P}_{\text{site}}(\alpha_i)$ probability that an active site with contact angle α_i does not nucleate

P_{freeze} probability of a drop freezing

$P(n)$ fraction of drops containing n particles

p_{num} number distribution of particles

$P_{\text{particle}}(S_{\text{ice}})$ probability of a single particle nucleating at S_{ice}

$P_{\text{site}}(\alpha)$ probability of nucleation of a single active site with contact angle α

r rate of nucleation

r_{cl} radius of cluster

r^*_{cl} ice cluster critical radius

$\rho(\alpha)$ surface density of active sites

S_{ice} saturation ratio with respect to ice

$S_{\text{ice,onset}}$ onset saturation over ice

$S_{\text{ice,previous}}$ S_{ice} measured immediately before $S_{\text{ice,onset}}$

$S_{\text{ice,r=0.05}}$ S_{ice} at which the nucleation rate equals 0.05s^{-1}

s_{site} surface area of an active site

σ_α standard deviation of normal distribution of contact angles

σ_g geometric standard deviation

$\sigma_{i/v}$ ice-vapour interfacial energy

Δt time step of experiment

T temperature

List of abbreviations

ATD Arizona Test Dust

CCN cloud condensation nucleus

CMS Clay Minerals Society

CNT classical nucleation theory

CRM cloud resolving model

GCM general circulation model

IN ice nucleus

INAS ice nucleation active site

PBAP primary biological aerosol particle

PCTFE polychlorotrifluoroethylene

RTD resistance temperature detector

SEM scanning electronc microscopy

SOA secondary organic aerosol

WSSR weighted sum of squared residuals

Acknowledgements

The completion of a PhD dissertation is an immense undertaking that requires support from a multitude of people. First I would like to thank Dr. J Roscoe for instilling in me a love of Chemistry and research. To my supervisor, Allan Bertram, thank you for your guidance and support without which I would not have been able to complete this undertaking. Allan, the mentorship and instruction you have provided me throughout my degree have made me into the scientist I am today. Your kindness and understanding have made the process more enjoyable and have created an excellent research environment.

Which brings me to the Bertram group. The work presented here would not have been possible without the help and support of all of the members of the Bertram group. Whether providing help in the lab, answering questions or socializing outside of the lab, you have all contributed to a fun and constructive working environment. I would like to thank all members, past and present, of the Bertram group: Matt, Mike, Daniel, Pedro, Lori, Simone, Emily, Sarah, Donna, Sebastian, Aidan, Song, Jason, Rich, Ryan, James, Yuan, Lindsay, Matt, Kristina, Amir, Meng, Yuri, Cédric, and Vickie. Thank you for all of the support and enjoyment you've provided me. Pedro and Aidan, thank you for all the late night discussions/arguments, I wouldn't trade them for anything. A very special thank you to Donna. You've been a wonderful friend and added enjoyment to long days and late nights waiting for ice to form.

I would also like to thank all of the members of the Chemistry department facilities who helped me throughout my degree. To all members of the Bioservices laboratory, Mechanical Engineering, Electrical Engineering, Glassblowing and IT, your technical support and friend-

ship were invaluable to me.

To all of my friends and family, I want to thank you for being there for me. I am so fortunate to have each one of you in my life. Finally, I want to thank my parents. Mom and Dad, I want to thank you for your unconditional love and support. You always made me believe that I could achieve anything I put my mind to. You have always been there for me and taught me the value of hard work. I am forever indebted to you for everything you have done for me.

To my parents, Jim and Doreen Wheeler

Chapter 1

Introduction

1.1 Atmospheric aerosols

An aerosol is a suspension of solid or liquid particles in a gas. Aerosol particles in the atmosphere cover a broad range of sizes from several nanometers (nm) to tens of micrometers (μm). The lifetime or residence time of aerosols in the atmosphere can vary significantly depending on multiple factors such as diameter and removal process. Atmospheric aerosol particles contribute to many different processes including the Earth's radiative balance, precipitation, spread of pathogens, and human health.

Atmospheric aerosols can have both primary and secondary sources. Primary sources refer to direct injection of aerosols into the atmosphere. This includes wind-blown dust, volcanic ash, sea-spray, and soot from biomass burning. In addition to these primary emissions of aerosols, some aerosols are produced through secondary processes, which transform atmospheric gasses into liquid or solid particles. One common type of aerosol formed through secondary processes is secondary organic aerosol (SOA), which is generated by the oxidation of organic precursors [Seinfeld and Pandis, 2006].

Atmospheric aerosols can also be divided into natural or anthropogenic sources. Naturally occurring aerosols include sea-spray particles, particles from dust storms, fungal spores, and bacteria. Human activity results in the release of aerosol particles through processes such as

fossil fuel combustion and biomass burning. It is often difficult to attribute the source of an aerosol as being from only a natural or an anthropogenic source. Mineral dust particles, for example, have both a natural and anthropogenic source. Natural activity such as wind action causes mineral dust to become suspended. However, human activities like agriculture and changes in surface water have led to increases in mineral dust aerosol concentrations [Forster et al., 2007].

The focus of this thesis is on two types of primary aerosol, mineral dust and primary biological aerosol particles (PBAPs). A more detailed discussion of the types of aerosol particles studied here follows.

1.1.1 Mineral dust aerosols

Mineral dust make up a significant portion of atmospheric aerosols. Annual estimates of the emission rate of mineral dust particles into the atmosphere range from 1000 – 4000 $\mathrm{Tg\,yr^{-1}}$ [Boucher et al., 2013].

Mineral dust particles become suspended primarily through wind action. Mineral dust emissions occur anywhere soil may become eroded by wind action, though arid regions are responsible for the majority of mineral dust particles emitted into the atmosphere. The vast majority of mineral dust aerosols originate in the Northern Hemisphere. Emissions from North Africa including the Saharan desert comprise the largest contribution, making up nearly 60% of all mineral dust emitted into the atmosphere [Tanaka and Chiba, 2006]. Regions in Asia, including the Arabian Peninsula and the Gobi desert, also contribute significant quantities of mineral dust aerosol to the atmosphere [Engelbrecht and Derbyshire, 2010; Tanaka and Chiba, 2006].

1.1.1.1 Clay minerals

The mineral dust particles studied in this thesis are classified as clay minerals. This important class of aluminosilicate minerals are comprised of alternating layers of alumina (Al_2O_3) and silica (SiO_2) with other impurities contained in the layers.

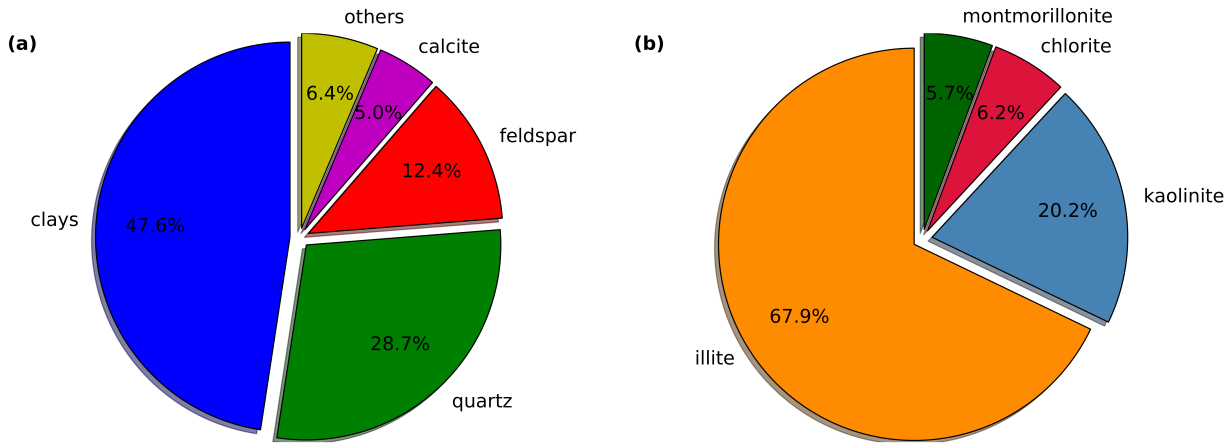

Figure 1.1: Average composition of mineral dust aerosols by mass determined from 15 separate studies. Mineral composition was determined from analysis of collected atmospheric aerosols and bulk analysis of soil samples collected from source regions. Samples were obtained from various locations in North Africa, the Americas, and across the Pacific representing both remote and near source regions. **(a)** shows the overall composition of the aerosol and **(b)** shows the composition of the clay fraction. Adapted from Murray et al. [2012].

Figure 1.1 shows the composition of mineral dusts measured from multiple field studies [Murray et al., 2012]. Of the total mineral dust composition, nearly 50% is contained in the clay fraction with the next largest fraction being composed of quartz. The prevalence of clay particles in the atmosphere is due to the small sizes these minerals typically produce ($< 2\,\mu$m). The small size of clay particles makes them easier to suspend in air and leads to longer atmospheric lifetimes than larger particles which settle out after a short time.

1.1.2 Primary biological aerosol particles (PBAPs)

Another commonly observed class of aerosol particles are primary biological aerosol particles (PBAPs) [Després et al., 2012]. These PBAPs include a large variety of different particle types with varying chemical and physical properties. PBAPs can include fungal spores, bacteria cells, pollen, viruses, or any suspended material of biological origin. Estimates of the total emission rates of PBAPs range from 10–1000 $\mathrm{Tg\,yr^{-1}}$ [Boucher et al., 2013; Després et al., 2012; Jaenicke, 2005].

Work in this thesis examines two sources of PBAPs: bacteria and fungal spores. Figure 1.2

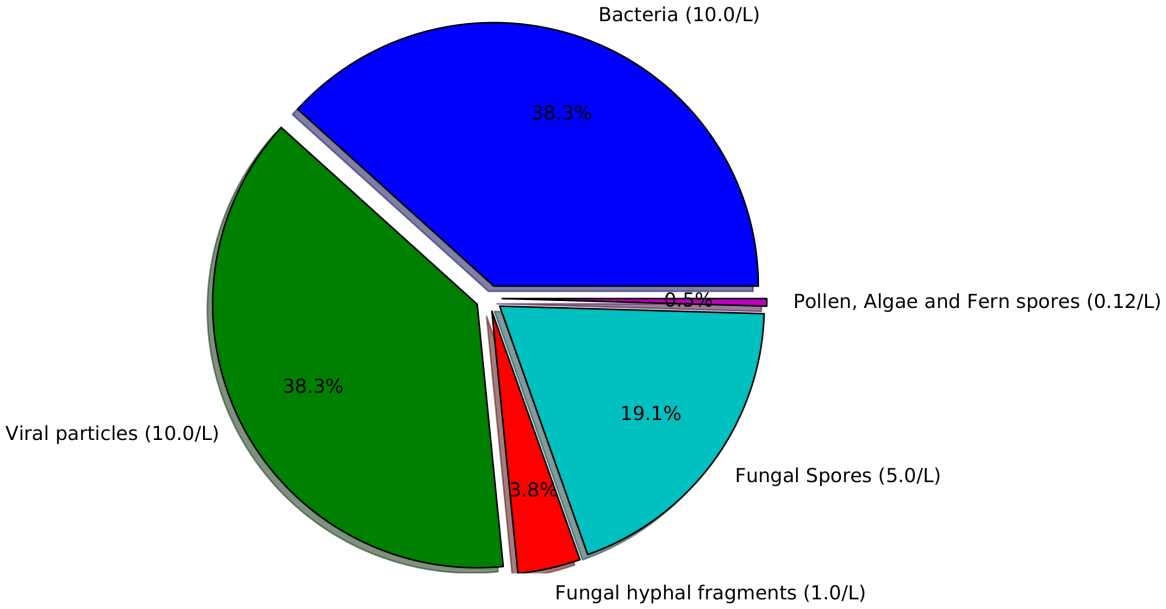

Figure 1.2: PBAP composition distribution based on typical number concentrations determined over vegetated regions. The values next to each PBAP type represent the typical number concentration per litre of air observed. Adapted from Table 4, Després et al. [2012].

shows the relative contribution of different PBAP sources to the total PBAP number concentration determined over vegetated areas [Després et al., 2012]. Typical concentrations are based on measurements and modelling from multiple sources. Viral particles and bacteria combined are estimated to make the largest contribution to the total PBAP concentrations. Fungal spores make up the majority of the remaining particles with other PBAPs contributing only a small percentage to the total concentration.

While the measurements above represent ground-level concentrations of PBAPs, the question remains as to the ability of these particles to reach altitudes in the atmosphere where they can induce ice nucleation. A recent study by DeLeon-Rodriguez et al. [2013] measured concentrations of bacteria and fungal spores at altitudes up to 10 km. Results showed that bacteria cells make up on average 20% by number of all aerosol particles 0.25 – 1 μm in diameter with individual measurements varying between 4 and 95%, indicating a large variability of PBAP concentrations. Haga et al. [2013] showed through dispersion modelling that between 6 and

9% of fungal spores emitted at specific locations in the Northern Hemisphere are able to reach altitudes high enough to influence ice nucleation. Hoose et al. [2010a] showed using a global circulation model that PBAPs exist at altitudes necessary for ice nucleation to occur. While results presented by Hoose et al. [2010a] suggest that PBAPs do not influence atmospheric ice nucleation on a global scale, results from other studies suggest that PBAPs may influence ice nucleation on a local or regional scale [Costa et al., 2014; Després et al., 2012; Gonçalves et al., 2012; Hazra, 2013; Phillips et al., 2008].

1.2 Atmospheric ice nucleation

This thesis focuses on the nucleation of ice in the atmosphere. Despite being thermodynamically favoured, pure water drops will not freeze near $0\,^{\circ}\mathrm{C}$. Instead, pure water drops in the atmosphere typically freeze, depending on drop volume, at around $-37\,^{\circ}\mathrm{C}$. This is referred to as the homogeneous freezing temperature of pure water. Colder homogeneous freezing temperatures occur if the drops contain solutes such as sulphuric acid (H_2SO_4) or ammonium sulphate ($(NH_4)_2SO_4$), due to the depression of the freezing point by the solutes.

The freezing of drops at temperatures above $-37\,^{\circ}\mathrm{C}$ are due to the presence of insoluble ice nuclei (IN). These IN are responsible for a reduction in the energy barrier to ice nucleation resulting in ice formation at warmer temperatures. The nucleation of ice due to the presence of insoluble IN is termed heterogeneous nucleation.

Heterogeneous nucleation can occur by four distinct modes [Vali, 1985]: deposition nucleation, immersion freezing, contact freezing, and condensation freezing. Figure 1.3 shows a schematic representation of these modes. The first, deposition nucleation, is the only mode which does not involve the liquid phase. In deposition nucleation, ice forms on IN directly from the vapour phase. Immersion freezing involves the nucleation of ice on IN immersed in supercooled drops. Contact freezing involves the freezing of a supercooled liquid drop upon coming into contact with an IN. Finally, condensation freezing involves the condensation of liquid water on IN under supercooled conditions followed immediately by the nucleation of an

ice phase.

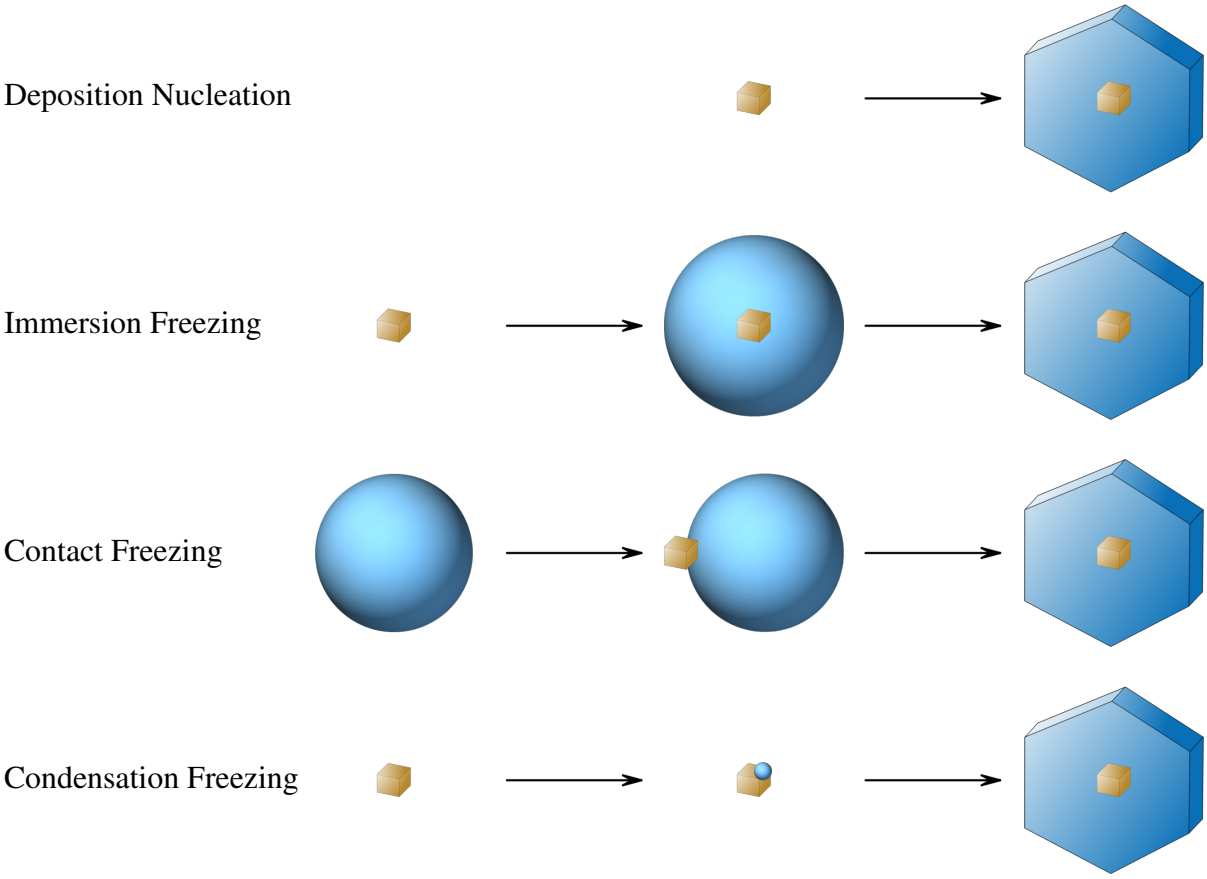

Figure 1.3: Schematic of the four different heterogeneous ice nucleation modes as described by Vali [1985]. IN are shown as brown cubes, liquid water is represented by blue spheres and ice crystals are shown as hexagonal polygons.

Two of the ice nucleation modes, deposition nucleation and immersion freezing, are examined in this thesis. A more detailed discussion of the two modes follows.

1.2.1 Deposition nucleation

As mentioned above, deposition nucleation is unique from the other three modes in that it does not involve a liquid phase. Under atmospheric conditions, ice does not form homogeneously directly from water vapour due to the high energy barrier required for homogeneous nucleation from the vapour phase [Pruppacher and Klett, 1997]. The addition of an ice nucleus, however, greatly reduces the energy barrier to nucleation and the formation of an ice phase becomes

feasible.

1.2.2 Immersion freezing

Immersion freezing occurs within supercooled drops. Homogeneous freezing of pure water, as mentioned above, requires temperatures around $-37°C$. The introduction of insoluble nuclei into water drops reduces the energy barrier to nucleation which allows for the formation of ice at temperatures warmer than $-37°C$. Similarly, the freezing temperature of solution drops can be increased due to the presence of IN. Studies have shown the observation of ice particles in mid-level clouds to be preceded by the formation of liquid water [Ansmann et al., 2008, 2009; De Boer et al., 2011; Westbrook and Illingworth, 2011]. This suggests that immersion freezing is an important mode of ice nucleation in the atmosphere. In clouds which contain both liquid drops and liquid drops with insoluble IN, mixed-phase clouds can form which are a mixture of both liquid drops and ice particles.

1.2.3 Mineral dust as IN

Mineral dust particles have long been known to be involved in atmospheric ice nucleation. Clay minerals are observed to be more abundant compared to other types of particles at the centre of snow crystals [Isono, 1955; Kumai, 1961; Kumai and Francis, 1962; Pruppacher and Klett, 1997]. Other field measurements have also shown that mineral dust particles play an important role in ice nucleation in the atmosphere, primarily in the immersion and deposition modes [e.g. Ansmann et al., 2008; Cziczo et al., 2004, 2013; DeMott et al., 2003b,a; Ebert et al., 2011; Heintzenberg et al., 1996; Isono et al., 1959; Klein et al., 2010; Kumai, 1961; Li and Min, 2010; Min et al., 2009; Prenni et al., 2009; Pruppacher and Klett, 1997; Richardson et al., 2007; Sassen, 2002; Sassen et al., 2003; Seifert et al., 2010; Targino et al., 2006; Twohy and Poellot, 2005]. Additionally, a multitude of laboratory studies have shown that mineral dust particles are effective IN in all four modes described above [see Hoose and Möhler, 2012, and references therein].

In this thesis the ice nucleation ability of three different mineral types is investigated: kaoli-

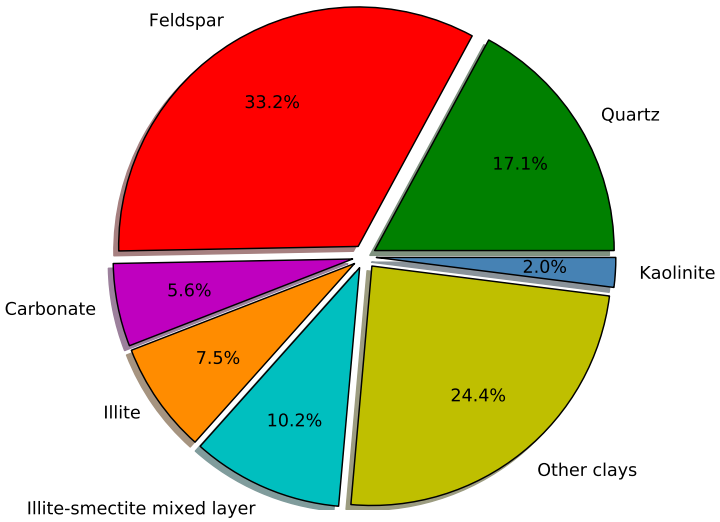

Figure 1.4: Mineral composition of ATD determined by X-ray diffraction. Shown are the relative amounts of each mineral type contained in a sample of ATD. Adapted from Table 1 from Broadley et al. [2012].

nite, illite, and Arizona Test Dust (ATD). All three of these minerals have been shown to be effective IN [Hoose and Möhler, 2012; Pruppacher and Klett, 1997, and references therein]. Kaolinite and illite are both clay minerals. As shown in Fig. 1.1a, the clay minerals make up the largest fraction of atmospheric mineral dust particles and kaolinite and illite make up the majority of the clays observed in the atmosphere (Fig. 1.1b). ATD is a commercially available mixture of various minerals including both clays and other mineral types. The chemical composition of ATD is shown in Fig. 1.4. This mixture is commonly used as a surrogate for natural atmospheric mineral dust and many studies have been conducted on the ice nucleation efficiency of ATD [Hoose and Möhler, 2012; Murray et al., 2012, and references therein].

1.2.4 PBAPs as IN

Some PBAPs have been shown to be effective IN. Many field studies have identified ice nucleation active PBAPs [Bowers et al., 2009; Christner et al., 2008a,b; Constantinidou et al., 1990; Garcia et al., 2012; Huffman et al., 2013; Jayaweera and Flanagan, 1982; Lindemann et al.,

1982; Maki and Willoughby, 1978; Morris et al., 2008; Pratt et al., 2009; Prenni et al., 2009, 2013]. One of the first species identified to have IN activity was the bacteria *Pseudomonas syringae* [Maki and Galyan, 1974; Vali et al., 1976] which was observed to cause ice nucleation at temperatures as warm as $-2\,^{\circ}\mathrm{C}$. There have been many subsequent laboratory studies which have investigated the freezing properties of *P. syringae* and other IN-active PBAPs, particularly bacteria, fungal spores and pollen [Després et al., 2012; Hirano and Upper, 2000; Möhler et al., 2007, and references therein]. The majority of these studies have been conducted in the immersion freezing mode with fewer studies investigating the deposition nucleation, condensation freezing, and contact freezing modes. This thesis focuses on the ice nucleation ability of multiple species of fungal spores and bacteria cells. As seen in Fig. 1.2 above, both bacteria and fungal spores make up a significant fraction of the number concentration of PBAPs in the atmosphere.

1.3 The direct and indirect effect of aerosols on climate

Atmospheric aerosols play an important role in the climate and hydrological cycle of the Earth. Aerosol particles scatter solar radiation which affects both visibility as well as climate. By reflecting incoming solar radiation, aerosols result in a cooling of the atmosphere [Jacob, 1999]. Conversely, certain aerosol particles, such as black carbon, can absorb solar radiation which can offset the cooling effect of scattering by particles [Seinfeld and Pandis, 2006]. This scattering and absorption of radiation is termed the aerosol "direct effect" on climate.

In contrast to the direct effect, aerosols also influence climate in an indirect way through the modification of cloud properties, termed the "indirect effect" on climate. Certain aerosol particles can act as either cloud condensation nuclei (CCN) or IN. These CCN and IN are responsible for the nucleation of liquid drops or ice in the atmosphere. Modifications of the concentration and chemical composition of these CCN or IN can result in various indirect effects on climate. Below, the indirect effect of CCN on climate is first discussed which involves only warm clouds. Then, the indirect effect of IN on climate is discussed which involves both

mixed-phase and ice clouds.

1.3.1 The indirect effect of CCN on climate

The indirect effect of CCN on climate can occur by two different mechanisms: the cloud albedo effect and the cloud lifetime effect. As with the direct effect described above, cloud drops also scatter incoming solar radiation. If the liquid water content of a cloud is assumed to remain constant, then increases in CCN concentrations will result in a larger number of smaller cloud drops. This has the effect of increasing the reflectivity of the cloud and is referred to as the "cloud albedo effect" [Twomey, 1974]. The increase in cloud reflectivity (albedo) results in a cooling of the atmosphere since less solar radiation is able to reach the Earth's surface. In addition to the increased albedo of clouds due to the cloud albedo effect, increases in CCN concentrations may result in increased cloud lifetimes [Albrecht, 1989]. A reduction in precipitation efficiency caused by decreases in droplet size results in longer lived clouds. These longer lived clouds result in an overall increase in the fractional cloudiness of the atmosphere which also increases the overall cloud albedo. This effect, which is estimated to be as significant as the cloud albedo effect [Lohmann and Feichter, 2005], is referred to as the "second indirect effect" or "cloud lifetime effect".

1.3.2 The indirect effect of IN on climate

Depending on environmental conditions, some clouds may be composed entirely of ice particles (ice clouds) or a mixture of liquid drops and ice particles (mixed-phase clouds). The indirect effect of IN on climate involves both ice clouds and mixed-phase clouds. The indirect effect of IN on climate is less understood than the indirect effect of CCN on climate [Denman et al., 2007; Lohmann and Feichter, 2005]. The indirect effect of IN on climate is thought to be different depending on cloud type. Below, the indirect effect of IN on climate is first discussed in the context of mixed-phase clouds and then in the context of ice clouds.

Ice particles formed in mixed-phase clouds deplete the liquid water due to the lower vapour pressure of water over ice compared to over liquid water. This process, referred to as the

Wegener-Bergeron-Findeisen process [Pruppacher and Klett, 1997], results in the growth of large ice crystals which form precipitation. Increases in the number of IN will result in the depletion of smaller water drops in favour of the formation of large ice crystals. If the total amount of water in a cloud remains constant then the surface area available for scattering decreases. This will result in a decrease of the scattering of radiation from these clouds. Increases in IN concentrations will also result in an increase in the amount of precipitation from these clouds. Increased precipitation of clouds will result in shorter lifetimes due to the depletion of water. This is referred to as the "glaciation indirect effect" [Lohmann, 2002] and has the effect of offsetting some of the cooling caused by the cloud albedo effect.

Unlike mixed-phase clouds which result in a net cooling of the Earth-atmosphere system by reflecting solar radiation, ice clouds are responsible for a net warming of the atmosphere due the absorption of outgoing terrestrial radiation (the greenhouse effect). All clouds will contribute with different magnitudes to the cooling of the Earth-atmosphere system through the reflection of solar radiation. Similarly, all clouds will, to differing degrees, contribute to the greenhouse effect by absorbing terrestrial radiation and emitting it back to the Earth's surface. For clouds closer to the Earth's surface, such as mixed-phase clouds, the temperature of the cloud is similar to that of the Earth's surface and there is only a small absorption of terrestrial radiation [Jacob, 1999; Seinfeld and Pandis, 2006]. The result is that the cooling caused by the indirect effect is more significant than the warming produced by the greenhouse effect. However, for ice clouds which occur at high altitudes, such as cirrus clouds, the temperature of the clouds is significantly different than that of the Earth's surface and the warming caused by the greenhouse effect is stronger than the cooling produced by the reflection of solar radiation [Jacob, 1999; Seinfeld and Pandis, 2006]. As a result, the overall effect of these ice clouds is warming of the Earth-atmosphere system. The effect of increasing IN concentrations in ice clouds is not well understood. Studies have suggested that increased IN concentrations may lead to decreases in the ice crystal concentration of these clouds due to a shift in the freezing mechanism from homogeneous freezing of supercooled concentrated solution drops

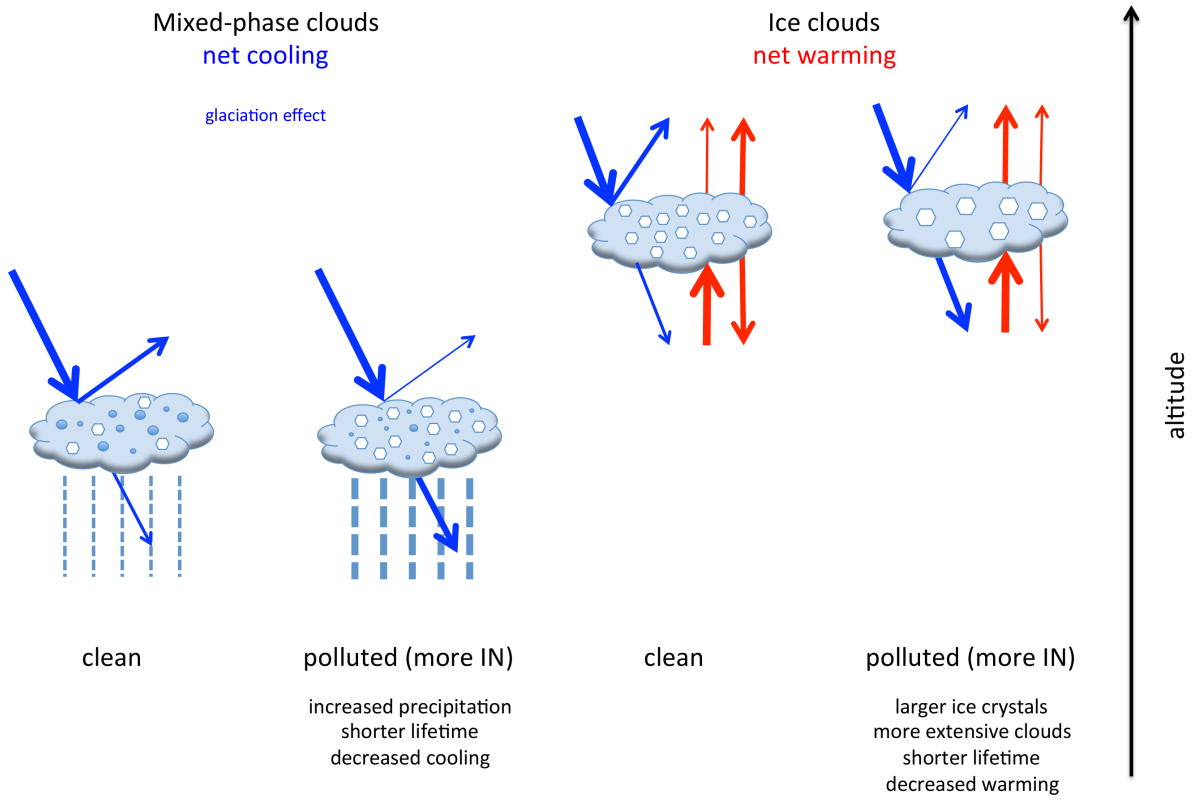

Figure 1.5: Schematic representation of indirect effects of IN on climate. A comparison is shown between the solar radiation (blue arrows), terrestrial radiation (red arrows) and precipitation (dashed lines) between clean and polluted air masses for the indirect effects of IN described in the text. The thickness of the arrows represents relative intensity of solar or terrestrial radiation and the thickness of the dashed lines represents relative amounts of precipitation. Cloud drops are shown as blue circles and ice particles are shown as white hexagons. Increases in IN concentration in low altitude clouds results in increases in precipitation, shorter lifetimes and decreased overall cooling. Increases in IN concentration in high altitude clouds results in larger ice crystals, more extensive clouds, shorter lifetimes and decreased net warming. Adapted from DeMott et al. [2010].

to heterogeneous freezing by IN [DeMott et al., 2010; Kärcher and Lohmann, 2003]. The earlier onset of nucleation by IN will prevent the homogeneous nucleation of liquid drops. The switch from homogeneous to heterogeneous nucleation will result in the formation of fewer but larger ice crystals and will lead to a decrease in the warming caused by these clouds. Shown in Fig. 1.5 is a schematic representation of the indirect effect of IN on climate in the context of both mixed-phase and ice clouds.

1.3.3 Modelling atmospheric ice nucleation

In order to better understand the indirect effect of IN on climate, a better understanding of ice nucleation by atmospheric particles is required. Atmospheric models including large scale general circulation models (GCMs) and smaller scale cloud resolving models (CRMs) are used to evaluate the indirect effect of IN on climate. However, in order to accurately evaluate the indirect effect of IN on climate, the ice nucleation ability of atmospheric aerosols needs to be understood and accurately parameterized and incorporated into these models. These parameterizations can be either theoretical or empirical. Empirical parameterizations enable the prediction of ice nucleation based on laboratory [Niemand et al., 2012] and field measurements [DeMott et al., 2010; Phillips et al., 2008, 2009]. For example, DeMott et al. [2010] presents a parameterization based on multiple field studies which relates the number of IN to the concentration of aerosol particles with diameters greater than $0.5\,\mu$m. Phillips et al. [2008] presents empirical presentations based on different particle types (dust and metallic, inorganic black carbon, and insoluble organic aerosols).

Theoretical parameterizations are based on some understanding of the nucleation process [Connolly et al., 2009; Fletcher, 1958, 1969; Hartmann et al., 2013; Lüönd et al., 2010; Marcolli et al., 2007; Niedermeier et al., 2011b, 2014] . These parameterizations often rely on classical nucleation theory (CNT) as a basis for the nucleation process with modifications used to describe the different nucleation abilities between particles. A more detailed description of CNT is presented in Chapter 2. Detailed descriptions of the theoretical parameterizations used in this thesis can be found in Chapters 3, 4, and 5.

The goal of this thesis is to improve our understanding of ice nucleation by atmospheric aerosols and to improve the parameterizations or schemes used to describe IN in atmospheric models. This research should lead to better predictions of climate change and its ramifications. More specifically, the ice nucleation of different mineral dust types is examined in both the deposition and immersion freezing modes through controlled laboratory studies. Freezing results from these studies are used to test different schemes commonly used to describe ice nucleation

in atmospheric models. Results from the immersion freezing measurements on mineral dusts are also used to determine ice nucleation active site (INAS) densities, which are often used to compare the ice nucleation ability of different IN. Experimental results on immersion freezing of different types of PBAPs reported in the literature are also used to test different schemes used to describe ice nucleation in atmospheric models.

1.4 Overview of dissertation

As mentioned above, this dissertation focuses on the ice nucleation properties of mineral dusts and PBAPs in the deposition and immersion modes. Chapter 1 (this chapter) gives an introduction to aerosols and outlines the importance of ice nucleation on atmospheric particles; Chapter 2 introduces CNT, which is the basis for several of the schemes used in this thesis; Chapters 3–5 are the research chapters; and Chapter 6 presents the conclusions of the research and suggestions for future work. Chapter 3 examines the surface area dependence of deposition ice nucleation on two commonly observed mineral dusts (kaolinite and illite). Experiments are performed on both minerals to determine the conditions (temperature, T, and saturation ratio, S_{ice}) for ice nucleation as a function of particle surface area. The ice nucleation results are used to test four different schemes for describing ice nucleation. Chapter 4 describes ice nucleation results in the immersion mode on two supermicron-sized mineral dust particle types (kaolinite and ATD). Freezing temperatures of drops with immersed mineral dust particles are measured. The freezing results are used to determine the INAS densities of supermicron dust particles for comparison with other measurements with the same mineral dusts in the submicron mode. The freezing results are also used to test four schemes used to describe ice nucleation. Chapter 5 uses freezing data of drops containing fungal spores and bacteria reported in the literature to test different schemes used to describe ice nucleation. This work investigates the best method for including PBAP ice nucleation in atmospheric models.

Chapter 2

Classical nucleation theory (CNT)

2.1 Stochastic vs singular nucleation

The exact nature of the heterogeneous nucleation of ice is not well understood. There exists a debate as to whether heterogeneous nucleation occurs through a stochastic or singular process [Vali, 2014]. "Stochastic" nucleation refers to the formation of ice clusters by random fluctuations. This is a time dependent process with nucleation being possible at any temperature as long as the observation time is long enough. "Singular" nucleation, on the other hand, refers to the formation of ice on a specific site of an IN at a characteristic temperature and/or saturation ratio depending on the type of nucleation. The nucleation of a given site is dependent only on the characteristic parameters and is independent of the observation time.

Evidence for the stochastic nature of nucleation can be derived from the observation of heterogeneous nucleation in drops held at constant temperature [Murray et al., 2011; Vonnegut and Baldwin, 1984; Welti et al., 2012]. Additionally, the observation of a variable freezing temperature with varying cooling rate [Wright et al., 2013], though small, provides further support for the stochastic nature of heterogeneous ice nucleation. Conversely, the singular nature of ice nucleation is demonstrated through small variation in the freezing temperature of drops exposed to repeated freezing and melting cycles [Shaw et al., 2005; Vali, 2008]. Recent work has suggested that heterogeneous ice nucleation is a combination of stochastic and singular

behaviour [Vali and Stansbury, 1966; Vali, 1994, 2008, 2014].

In this thesis laboratory freezing experiments are used to test the ability of a number of schemes used to describe heterogeneous ice nucleation in atmospheric models. The schemes tested include a scheme which is completely stochastic, a scheme which is completely singular as well as several schemes which combine both stochastic and singular nucleation. Several of these schemes are based on classical nucleation theory (CNT). As a result, details on CNT are given below.

CNT was originally developed for the formation of a stable liquid phase from a meta-stable vapour phase [Mullin, 2001]. First the formation of an ice phase from the vapour phase in the absence of heterogeneous ice nucleus (IN) (i.e. homogeneous nucleation from the vapour phase) will be considered and then expanded for the cases of ice formation in the deposition and immersion modes.

2.2 Homogeneous nucleation of ice

Consider the formation of an ice cluster from a supersaturated vapour phase. The free energy associated with the creation of the ice phase, ΔG_{cl}, is the sum of the free energy contributions from the formation of a new interface, ΔG_s, which is energetically unfavourable (positive ΔG_s), and the free energy contribution associated with the formation of bonds within the volume of the ice cluster, ΔG_v, which can be either positive or negative depending on the temperature and amount of water vapour [Murray et al., 2012].

$$\Delta G_{\mathrm{cl}} = \Delta G_s + \Delta G_v \tag{2.1}$$

ΔG_s is governed by the surface tension of the ice phase,$\sigma_{i/v}$. If the cluster is assumed to be a sphere, then the free energy required to create the new surface is given by

$$\Delta G_s = 4\pi r_{\mathrm{cl}}^2 \sigma_{\mathrm{i/v}}, \tag{2.2}$$

where r_{cl} is the radius of the cluster.

ΔG_v can be represented by

$$\Delta G_v = n_{\mathrm{cl}}\left(\mu_i - \mu_v\right) = -\frac{4\pi r_{\mathrm{cl}}^3}{3\nu_i} \cdot kT \ln S_{\mathrm{ice}}, \tag{2.3}$$

where n_{cl} is the number of water molecules in the cluster and μ_i - μ_v is the difference in chemical potential between the ice and vapour phases. The number of water molecules can be calculated from the volume of the cluster and the molecular volume of ice, ν_i. The difference in chemical potential is given by $-kT \ln S_{\mathrm{ice}}$ [Seinfeld and Pandis, 2006] where S_{ice} is the ratio of the partial pressure of water vapour to the saturation vapour pressure over ice, k is the Boltzmann constant and T is the temperature of the cluster.

Combining Eqs. (2.2) and (2.3) gives

$$\Delta G_{\mathrm{cl}} = -\frac{4\pi r_{\mathrm{cl}}^3}{3\nu_i} \cdot kT \ln S_{\mathrm{ice}} + 4\pi r_{\mathrm{cl}}^2 \sigma_{\mathrm{i/v}}. \tag{2.4}$$

The variation of ΔG_{cl} with cluster radius is given in Fig. 2.1 (solid line). As can be seen, ΔG_{cl} reaches a maximum at a particular radius, r_{cl}^*. If additional water molecules are added to a cluster with radius r_{cl}^*, then there will be a decrease in the free energy and further additions of water molecules becomes energetically favourable. This will lead to the formation of a macroscopic ice crystal. On the other hand, for clusters which form with radii smaller than r_{cl}^*, the addition of water molecules is energetically unfavourable and the formation of a macroscopic ice crystal is not favoured.

The size of the critical radius, r_{cl}^*, can be obtained by calculating the maximum of the free energy with respect to the cluster radius (i.e. where $\frac{d\Delta G_{\mathrm{cl}}}{dr_{\mathrm{cl}}} = 0$). The size of the critical radius is given by

$$r_{\mathrm{cl}}^* = \frac{2\sigma_{\mathrm{i/v}}\nu_i}{kT \ln S_{\mathrm{ice}}}. \tag{2.5}$$

The height of the energy barrier (activation energy) in Fig. 2.1, ΔG_{act}, is obtained by

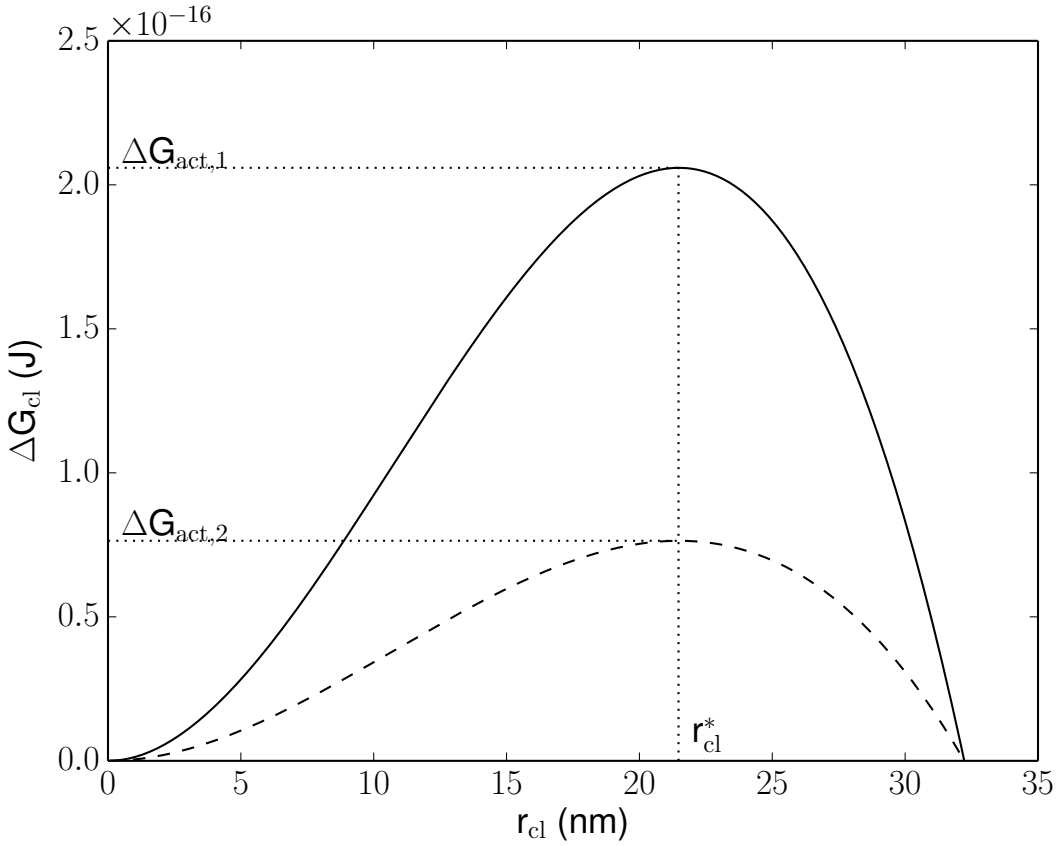

Figure 2.1: Classical nucleation theory (CNT) description of the free energy of cluster formation as a function of cluster radius. ΔG_{cl} is calculated according to Eq. (2.4) using an ice/vapour interfacial energy of $1.065 \times 10^{-5}\mathrm{J\,cm^{-2}}$ [Pruppacher and Klett, 1997], a molecular volume of ice of $3.2 \times 10^{-23}\mathrm{cm}^3$ [Lide, 2001], a temperature of 243 K, a saturation ratio of 1.1 and a contact angle of 80°. Clusters smaller than r^*_{cl} will favour a reduction in cluster radius while those greater than r^*_{cl} will favour an increase in radius leading to the growth of a macroscopic ice crystal. The introduction of a heterogeneous IN reduces the energy barrier to nucleation by a factor, $f_{\mathrm{het}}(\alpha)$, where $\Delta G_{\mathrm{act},1} = f_{\mathrm{het}}(\alpha) \cdot \Delta G_{\mathrm{act},2}$, dashed line. This reduction allows for nucleation to occur at warmer temperatures, T, and lower supersaturations, S_{ice}.

substituting Eq. (2.5) into Eq. (2.4):

$$\Delta G_{\text{act}} = \frac{16\pi\sigma_{\text{i/v}}^3 v_i^2}{3\left(kT\ln S_{\text{ice}}\right)^2} \tag{2.6}$$

The nucleation rate constant, j_{hom}, takes the form of an Arrhenius equation given by

$$j_{\text{hom}} = A_{\text{hom}} \exp\left(-\frac{\Delta G_{\text{act}}}{kT}\right) = A_{\text{hom}} \exp\left(-\frac{16\pi\sigma_{\text{i/v}}^3 v_i^2}{3kT\left(kT\ln S_{\text{ice}}\right)^2}\right), \tag{2.7}$$

where A_{hom} is the pre-exponential factor for homogeneous nucleation with units of $\text{cm}^{-3}\text{s}^{-1}$.

2.3 Heterogeneous nucleation of ice

2.3.1 Deposition nucleation of ice

In deposition nucleation, ice forms directly from the vapour phase similar to the process described above for homogeneous nucleation of water vapour. Unlike the homogeneous case described above, a solid IN is present onto which the ice nucleates. This heterogeneous IN reduces the energy barrier to nucleation making nucleation at a given temperature and supersaturation more likely than in the homogeneous case. This is illustrated in Fig. 2.1. The solid line shows the free energy barrier to nucleation in the homogeneous case. The introduction of a heterogeneous IN reduces the energy barrier as shown by the dashed line. The nucleation probability is greater for the heterogeneous case due to the decreased energy barrier.

The nucleation rate constant for deposition nucleation is given by

$$j_{\text{het}} = j_0 \exp\left(-\frac{\Delta G_{\text{act}} f_{\text{het}}(\alpha)}{kT}\right), \tag{2.8}$$

where ΔG_{act} is given by Eq. (2.6). The value of ΔG_{act} is reduced by a factor known as the contact parameter, $f_{\text{het}}(\alpha)$, with values between 0 and 1. The value of the contact parameter depends on the IN and is further discussed in Chapters 3 & 4. The pre-exponential factor, j_0,

has units of $\mathrm{cm}^{-2}\mathrm{s}^{-1}$.

2.3.2 Immersion freezing of ice

Nucleation in the case of immersion freezing is more complicated than for deposition nucleation. In the case of immersion freezing, the un-nucleated water molecules exist in the supercooled liquid phase. In order to form an ice cluster, water molecules must break existing hydrogen bonds in order to associate themselves with the ice cluster. This breaking of bonds results in a second energy barrier to nucleation [Pruppacher and Klett, 1997]. This energy barrier is referred to as the diffusion free energy, ΔF_{diff}. The nucleation rate constant for heterogeneous nucleation in the immersion mode is given by

$$j_{\mathrm{het}} = j_0 \exp\left(-\frac{\Delta G_{\mathrm{act}} f_{\mathrm{het}}(\alpha)}{kT} - \frac{\Delta F_{\mathrm{diff}}}{kT}\right). \tag{2.9}$$

Chapter 3

Deposition nucleation on mineral dust particles: a case against classical nucleation theory with the assumption of a single contact angle

3.1 Introduction

Atmospheric aerosol particles can indirectly influence climate by modifying the formation conditions and properties of ice and mixed-phase clouds. To better understand this topic, an improved understanding of the ice nucleation properties of atmospheric aerosols is required, and these properties need to be parameterized and incorporated in atmospheric models [Baker and Peter, 2008; Cantrell and Heymsfield, 2005; DeMott, 2002; Hegg and Baker, 2009; Houghton et al., 2001].

Ice nucleation may occur in the atmosphere either homogeneously or heterogeneously. Homogeneous nucleation involves the freezing of liquid droplets. In heterogeneous nucleation, ice forms on insoluble or partially soluble aerosol particles known as ice nuclei (IN). Four dif-

ferent modes of heterogeneous ice nucleation have been identified: immersion, condensation, deposition and contact nucleation. These four modes are discussed in Chapter 1. In the following we focus on deposition nucleation, which involves the formation of ice on a solid particle directly from the vapour phase [Pruppacher and Klett, 1997; Vali, 1985].

Different schemes have been developed to parameterize heterogeneous nucleation data. One of the simplest is classical nucleation theory (CNT) [Pruppacher and Klett, 1997] combined with the assumption of a single contact angle, α. We refer to this as the single-α scheme. This scheme assumes ice nucleation is a stochastic process and can occur at any location on the surface of a particle with equal probability (i.e. the surface is energetically uniform for ice nucleation). Therefore, each particle has the same probability per unit surface area to nucleate ice [Pruppacher and Klett, 1997]. Nucleation data is parameterized using a single parameter, the contact angle. Due in part to its simplicity, researchers have used the single-α scheme to parameterize laboratory data for use in atmospheric simulations [e.g. Archuleta et al., 2005; Chen et al., 2008; Chernoff and Bertram, 2010; Eastwood et al., 2008, 2009; Fornea et al., 2009; Hung et al., 2003]. In addition, the single-α scheme has been used to describe heterogeneous nucleation in atmospheric cloud simulations [e.g. Hoose et al., 2010a,b; Jensen and Toon, 1997; Jensen et al., 1998; Kärcher, 1996, 1998; Kärcher et al., 1998; Morrison et al., 2005].

A modification of the single-α scheme is the probability distribution function-α scheme (pdf-α scheme) [Lüönd et al., 2010; Marcolli et al., 2007]. Similar to the single-α scheme, the pdf-α scheme assumes that ice nucleation is stochastic and can be described by CNT. Nucleation can occur at any location on the surface of a particle with equal probability (i.e. the surface is energetically uniform for ice nucleation). However, the ice nucleation ability varies from particle to particle, which is described by a probability distribution function of contact angles, α. This scheme has recently been used to parameterize laboratory data of Marcolli et al. [2007] and Lüönd et al. [2010].

Yet another modification to the single-α scheme is the active site scheme [Fletcher, 1969;

Gorbunov and Kakutkina, 1982; Han et al., 2002; Lüönd et al., 2010; Marcolli et al., 2007; Martin et al., 2001; Niedermeier et al., 2011b]. In this scheme it is assumed that ice nucleation is a stochastic process and can be described by CNT. However, small areas or sites on a particle may be more effective at nucleating ice than the remainder of the particle. The distribution and ice nucleation properties of these areas, referred to as "active sites," govern the nucleating ability of a particle. The active site scheme has been used for parameterizing laboratory data and for describing ice nucleation in atmospheric models [Fletcher, 1969; Gorbunov and Kakutkina, 1982; Khvorostyanov and Curry, 2000, 2004, 2005, 2009; Kulkarni and Dobbie, 2010; Lüönd et al., 2010; Saunders et al., 2010].

The final scheme used here is the deterministic scheme [Connolly et al., 2009; Lüönd et al., 2010]. Unlike the other three schemes discussed above, this scheme is not based on classical nucleation theory. When applied to deposition nucleation, the deterministic scheme assumes particles have a characteristic number density of surface sites, and ice forms immediately on a surface site upon reaching a definite ice saturation ratio. This scheme has been used recently to parameterize immersion nucleation data for mineral dust particles [Connolly et al., 2009; Lüönd et al., 2010; Murray et al., 2011; Niedermeier et al., 2010].

In the following we investigate deposition nucleation of ice on illite and kaolinite particles, two minerals that are a significant fraction (up to 50 %) of atmospheric mineral dust [Claquin et al., 1999]. Mineral dust particles can play an important role in atmospheric ice formation based on previous field measurements and modelling studies [e.g. Ansmann et al., 2008; Barahona et al., 2010; Cziczo et al., 2004; DeMott et al., 2003a; Heintzenberg et al., 1996; Hoose et al., 2008; Klein et al., 2010; Koehler et al., 2010; Li and Min, 2010; Min et al., 2009; Prenni et al., 2009; Sassen, 2002; Sassen et al., 2003; Seifert et al., 2010; Twohy and Poellot, 2005]. We show that the S_{ice} conditions when ice first nucleates on kaolinite and illite particles are a strong function of the surface area available for nucleation. This surface-area dependent data is then used to test the different schemes discussed above. We show that the single-α scheme cannot describe the laboratory data, but the pdf-α scheme, the active site scheme and the de-

terministic scheme fit the data within experimental uncertainties. Parameters from the fits to the data are presented and the atmospheric implications are discussed.

3.2 Experimental

3.2.1 Ice nucleation experiments

The apparatus used in these studies has been described in detail previously [Dymarska et al., 2006; Eastwood et al., 2008; Parsons et al., 2004]. Figure 3.1 shows a schematic of the instrumental setup used. It consists of an optical microscope (Zeiss Axiotech 100 equipped with a 10X objective) coupled to a flow cell in which the saturation ratio and temperature can be accurately controlled. The saturation ratio, S_{ice}, is defined as the ratio of water vapour partial pressure to the saturation vapour pressure of ice at the same temperature. Mineral dust particles were deposited on the bottom surface of the flow cell; the saturation ratio with respect to ice inside the cell was increased, and the conditions for onset of ice nucleation (when the first particle nucleated ice) was determined with a reflected light microscope. We define this as the onset S_{ice} $\left(S_{\mathrm{ice,onset}}\right)$. The S_{ice} over the particles was controlled by continuously flowing a mixture of dry and humidified He through the flow cell. The humidity of the gas stream was continuously monitored using a frost point hygrometer (General Eastern 1311 DR) which was calibrated against the ice frost point within the flow cell [Dymarska et al., 2006].

The bottom surface of the flow cell, which supported the particles, consisted of a glass cover slide treated with dichlorodimethylsilane to make a hydrophobic surface [Dymarska et al., 2006]. This ensured that ice did not nucleate directly on the surface of the glass slide. The S_{ice} conditions at which all the particles nucleated ice could not be determined since after ice formed on the first particle, the S_{ice} above the other particles was reduced as water vapour condensed on the first nucleated particle. Each experiment involved determining the $S_{\mathrm{ice,onset}}$ for an ensemble of particles and this procedure was repeated a number of times with varying numbers of particles. $S_{\mathrm{ice,onset}}$ was determined for each sample once (i.e. measurements were not repeated on the same sample).

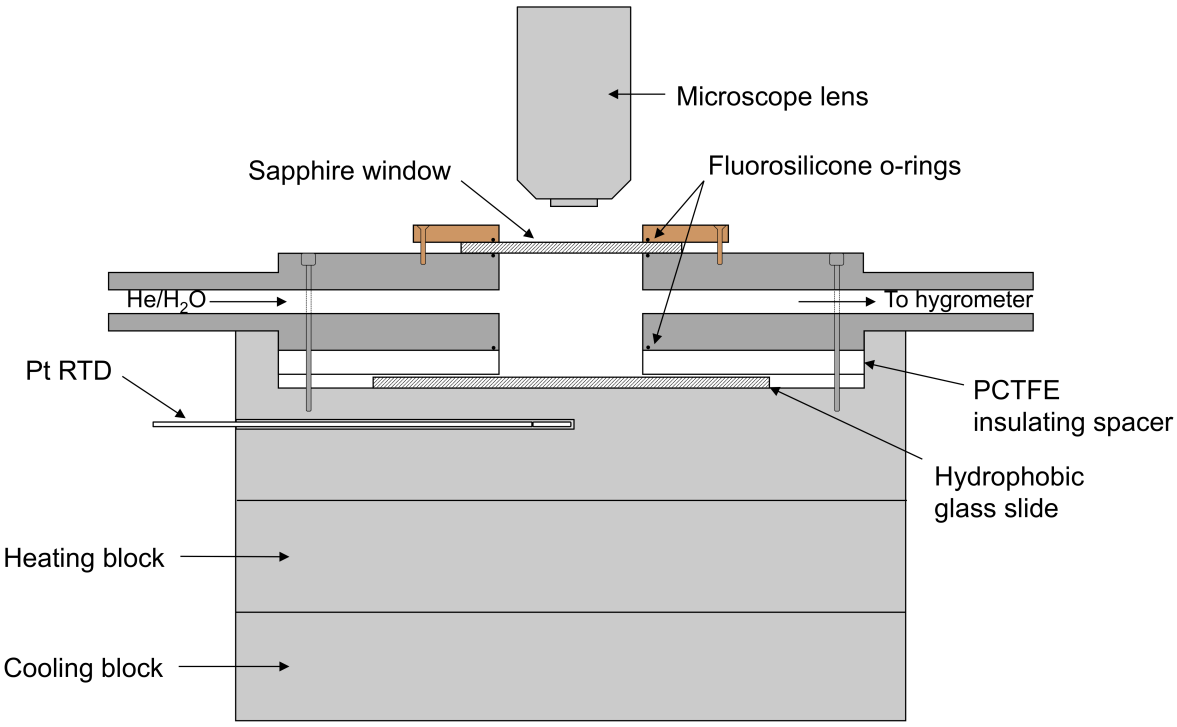

Figure 3.1: Schematic of the flow cell used for ice nucleation measurements. The flow cell is composed of stainless steel inserted into an aluminium holder. The bottom of the flow cell is a hydrophobic glass slide and this is separated from the stainless steel through an insulating spacer made of polychlorotrifluoroethylene (PCTFE) which prevents ice formation on the stainless steel by keeping its temperature slightly above that of the glass slide. Beneath the flow cell are two additional aluminium blocks, one of which allows coolant from a temperature controlled chiller to pass through and the other contains a heater. The combination of the two is used to accurately control the temperature of the flow cell which is measured by a platinum resistance temperature detector (RTD) located beneath the flow cell. A sapphire window in the top of the flow cell enables observation of the particles inside the flow cell through an optical microscope. Downstream of the flow cell is a frost point hygrometer which allows for accurate measurement of the humidity supplied to the cell.

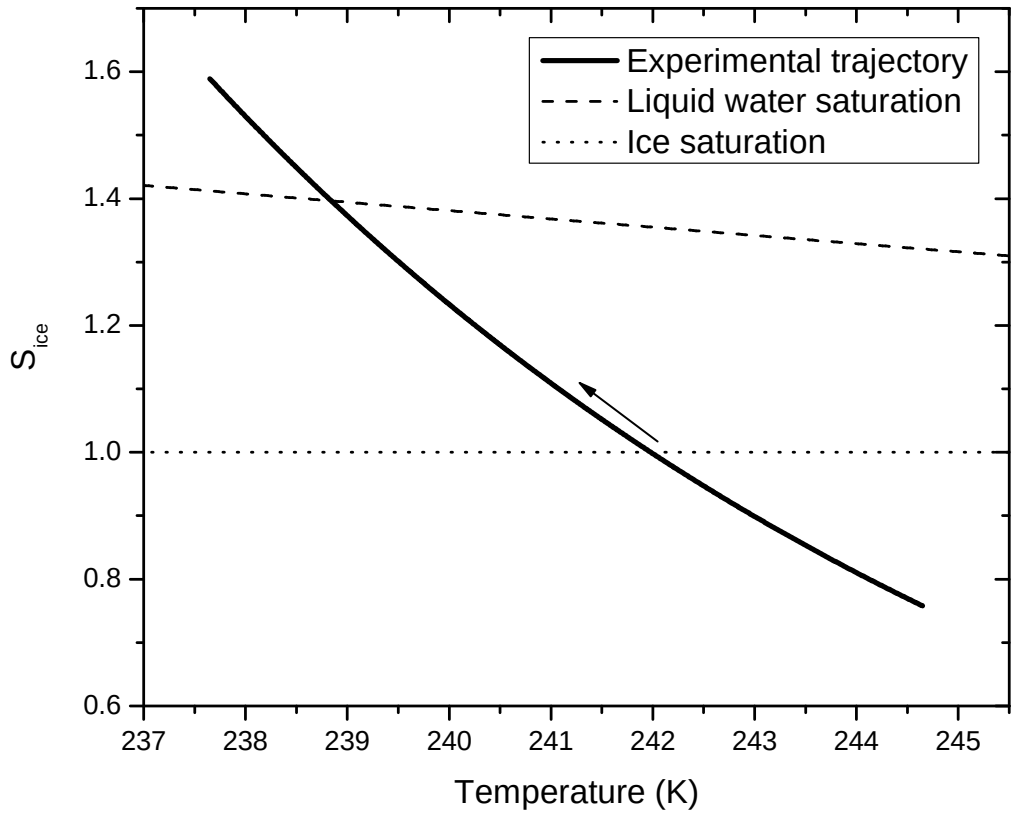

Figure 3.2: Typical experimental trajectory for the ice nucleation experiments. Experiments start below ice saturation and the temperature is decreased until ice crystals are observed.

Typical experimental S_{ice} trajectories used in these ice nucleation experiments are illustrated in Fig. 3.2. At the beginning of the experiments, the particles were exposed to a flow of dry He gas at room temperature ($S_{\text{ice}} < 1\,\%$). The temperature of the cell was then rapidly lowered and the S_{ice} was set to approximately $80\,\%$. The nucleation experiments were then conducted by steadily decreasing the temperature $\left(-0.1\,\text{K}\,\text{min}^{-1}\right)$ and thus increasing the S_{ice} as shown in Fig. 3.2. The S_{ice} ramp rate was approximately $1\,\%\,\text{min}^{-1}$. Optical images were recorded every 20 s, which corresponds to a change of $\sim 0.33\% S_{\text{ice}}$.

3.2.2 Sample preparation

Kaolinite and illite samples were purchased from Fluka (product ID: 03584) and the Clay Minerals Society (product ID: IMt-1), respectively. The mineral samples were deposited on hydrophobic glass slides using the following technique: dry dust particles were placed in a glass vessel immersed in an ultrasonic bath. A flow of ultrahigh-purity N_2 was passed through the vessel, and vibrations from the ultrasonic bath caused the dust particles to be suspended in the flow of N_2. This flow was directed at the hydrophobic glass slides, and the dust particles were deposited on the slides by impaction.

3.2.3 Total surface area, particle size, and particle number

The total surface area available for nucleation in each experiment, A_{total}, was determined from the images recorded with the optical microscope [Chernoff and Bertram, 2010; Dymarska et al., 2006; Eastwood et al., 2008, 2009]. First, the projected (i.e. 2-dimensional) surface area in a given experiment was determined with digital image analysis software (Northern Eclipse). The projected surface area was then multiplied by a factor of 4 to give A_{total}. A factor of 4 assumes that all particles are spherical, and the surface area available for nucleation can be approximated by the geometric surface area of the particles. Based on this analysis, the total surface area of the mineral dust deposited in any particular experiment ranged from 3.5×10^{-6} to $8 \times 10^{-3}\,\text{cm}^2$. Sensitivity to the assumption of spherical particles is explored in Section 3.4.5.

The size of the particles in the experiments were also determined with images from the optical microscope. In total 383 particles were analyzed for kaolinite and 363 particles for illite to extract size information. Shown in Fig. 3.3 are the number distributions of particles in the kaolinite and illite experiments determined from this analysis. Based on a log-normal fit to the data, the mean geometric diameter ($\bar{D_g}$) and geometric standard deviation (σ_g) in the experiments were $10.74\,\mu$m and 0.669 for kaolinite and $7.27\,\mu$m and 0.594 for illite. The optical resolution limit of the microscope was approximately $1\,\mu$m. Scanning electron microscopy was also carried out on some slides to ensure that the number of particles less than $1\,\mu$m on the

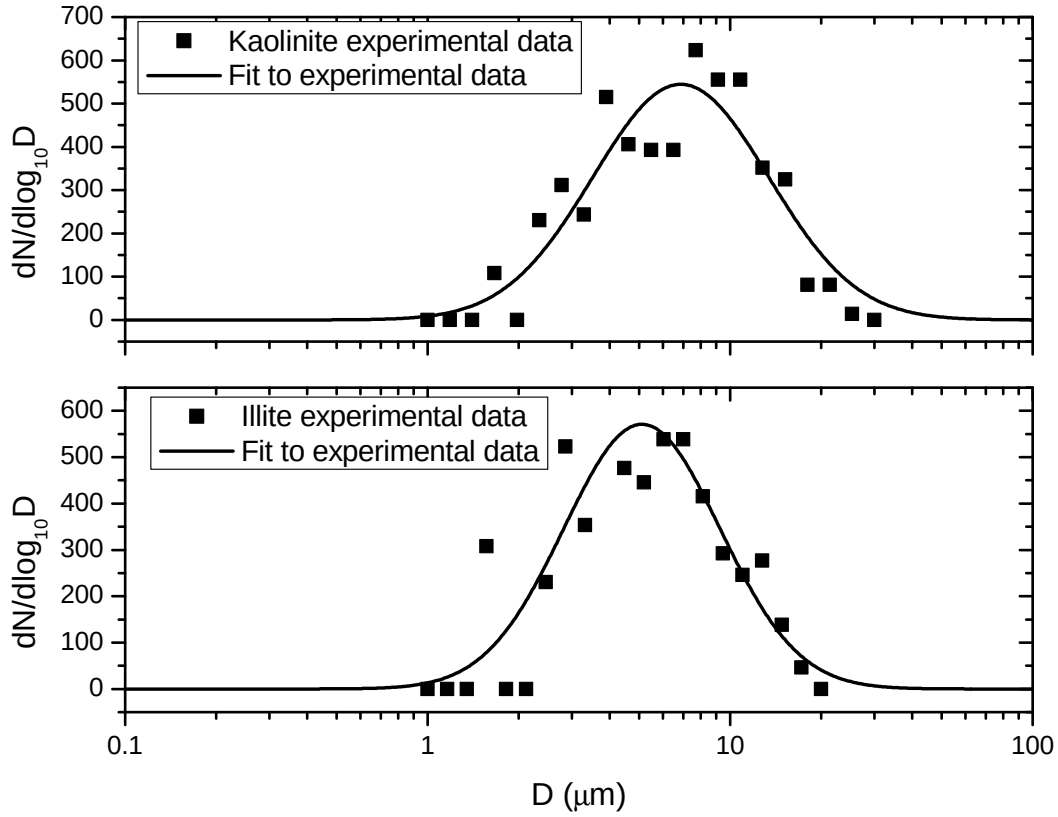

Figure 3.3: Number distributions measured using the optical microscope. N represents the number of particles and D represents the diameter. The experimental data were fit to a log-normal distribution function. Based on fits to the data, the mean geometric diameter $(\bar{D}_g)$ and geometric standard deviation (σ_g) in the experiments were $10.74\,\mu$m and 0.699 for kaolinite and $7.27\,\mu$m and 0.594 for illite.

slides was small. From the electron microscope images we concluded that $< 0.5\,\%$ of the total surface area lies in the sub-micrometer range. Also note that from the images recorded during the freezing experiments we can conclude that ice nucleation always occurred on particles $> 1\,\mu$m in diameter, further confirming that particles with diameters $< 1\,\mu$m are not important in our experiment. The size distribution presented in Fig. 3.3 is different from the size distribution reported by Welti et al. [2009] for kaolinite samples also purchased from Fluka since our method of depositing particles on slides favours particles with diameters $> 1\,\mu$m.

The number of particles in each experiment was calculated by the following equation:

$$N_{\text{total}} = \frac{A_{\text{total}}}{A_{\text{avg}}}, \tag{3.1}$$

where N_{total} is the number of particles, A_{total} is the total surface area of particles calculated as described above, and A_{avg} is the average surface area of the particles. The value of A_{avg} was calculated using the following equation [Reist, 1992]:

$$A_{\text{avg}} = \pi \bar{D_g}^2 \exp\left(2\sigma_g^2\right), \tag{3.2}$$

where $\bar{D}_g$ and σ_g are the geometric mean diameter and geometric standard deviation of the number distributions discussed above and calculated form the data shown in Fig. 3.3. In each experiment the number of particles on a slide ranged from 1 to ~ 1000.

3.3 Results

3.3.1 $S_{\text{ice,onset}}$ as a function of surface area

The individual onset results obtained for kaolinite and illite particles are shown in Figs. 3.4a and 3.5a respectively. Each data point represents the onset conditions observed for a single sample of dust particles, and the error bars are based on the manufacturer's stated uncertainties for the frost point hygrometer, RTD, and temperature readout. A few of the results for kaolinite particles are at $S_{\text{ice,onset}}$ values < 1 including error bars. This suggests that the uncertainties in $S_{\text{ice,onset}}$ are slightly larger than reported. There should not be an offset in our measurements since the relative humidity was calibrated with the ice frost point within the cell as mentioned above.

A total of 84 and 52 individual nucleation experiments were performed for kaolinite and illite, respectively. Measurements made with surface areas greater than $\sim 10^{-4}\,\text{cm}^2$ show both kaolinite and illite to be very good ice nuclei; nucleation occurred at supersaturations of less

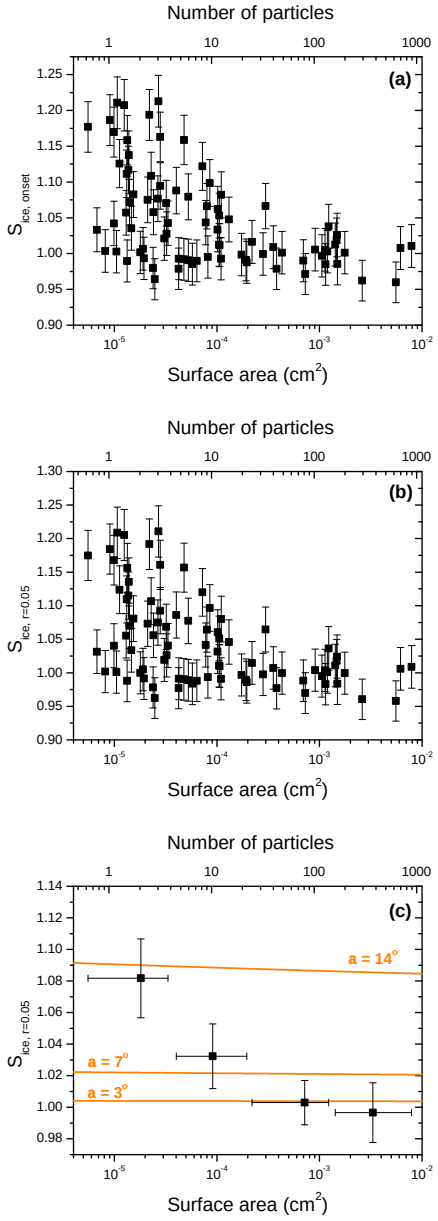

Figure 3.4: Results for kaolinite particles: **(a)** individual onset measurements, **(b)** individual $S_{\mathrm{ice,r=0.05}}$ results, and **(c)** average $S_{\mathrm{ice,r=0.05}}$. The average values are calculated for four equally sized bins and the horizontal error bars show the range of data points in each bin. The surface area values in **(c)** represent the average surface area of the points in each bin. Error in $S_{\mathrm{ice,onset}}$ is given as experimental error in measurements of saturation. Error in $S_{\mathrm{ice,r=0.05}}$ is based on the difference between $S_{\mathrm{ice,onset}}$ and $S_{\mathrm{ice,previous}}$ as well as the uncertainty in measuring $S_{\mathrm{ice,onset}}$. Error in the average $S_{\mathrm{ice,r=0.05}}$ represents the 95 % confidence interval. Predictions are shown using the single-α scheme (orange lines) calculated using Eq. (3.7). In addition to surface area, the corresponding number of particles calculated from A_{avg} is also shown.

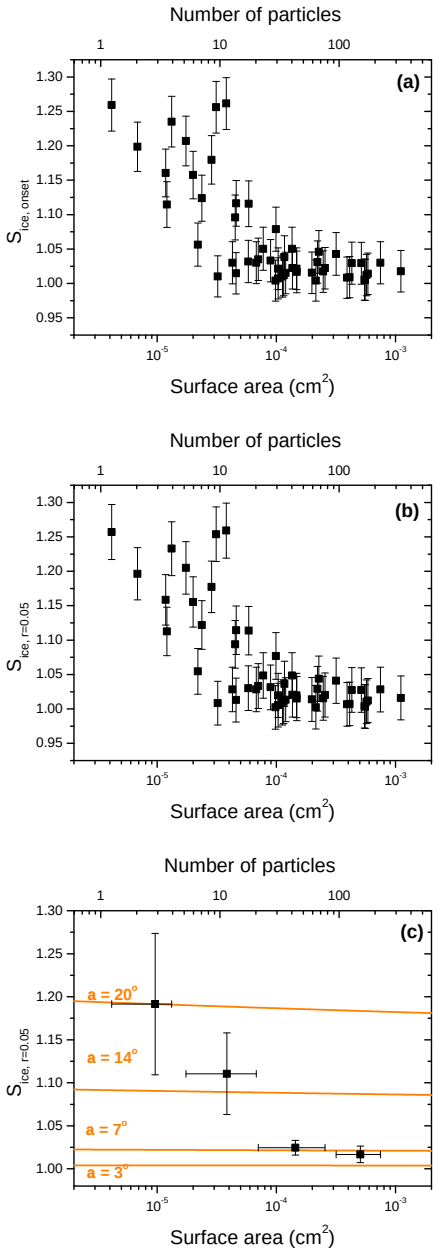

Figure 3.5: Results for illite particles: **(a)** individual onset measurements, **(b)** individual $S_{\mathrm{ice,r=0.05}}$ results, and **(c)** average $S_{\mathrm{ice,r=0.05}}$. The average values are calculated for four equally sized bins and the horizontal error bars show the range of data points in each bin. The surface area values in **(c)** represent the average surface area of the points in each bin. Error in $S_{\mathrm{ice,onset}}$ is given as experimental error in measurements of saturation. Error in $S_{\mathrm{ice,r=0.05}}$ is based on the difference between $S_{\mathrm{ice,onset}}$ and $S_{\mathrm{ice,previous}}$ as well as the uncertainty in measuring $S_{\mathrm{ice,onset}}$. Error in the average $S_{\mathrm{ice,r=0.05}}$ represents the 95 % confidence interval. Predictions are shown using the single-α scheme (orange lines) calculated using Eq. (3.7). In addition to surface area, the corresponding number of particles calculated from A_{avg} is also shown.

than 5 %. These results are consistent with previous measurements for both kaolinite and illite particles [Bailey and Hallett, 2002; Chernoff and Bertram, 2010; Eastwood et al., 2008; Kanji et al., 2008; Möhler et al., 2008a,c; Salam et al., 2006; Welti et al., 2009; Zimmermann et al., 2007, 2008]. The measurements made at low surface coverages $\left(< 10^{-4}\,\mathrm{cm}^2\right)$, however, show a different trend than was observed for high surface coverages. Onset values were observed over a broad range of saturation ratios (100 % to 125 %). The spread in onset values between different experiments is greater than the uncertainty in the measurements of S_{ice}.

3.3.2 $S_{\mathrm{ice,r=0.05}}$ as a function of surface area

$S_{\mathrm{ice,onset}}$ values reported in Figs. 3.4a and 3.5a correspond to the conditions when the number of nucleation events is greater than or equal to 1. Since the time between images is 20 s, at $S_{\mathrm{ice,onset}}$ the rate of nucleation, r, is $\geq 0.05\,\mathrm{s}^{-1}$. In the previous image (collected before $S_{\mathrm{ice,onset}}$, which we define as $S_{\mathrm{ice,previous}}$) there was no nucleation, i.e. $r = 0\,\mathrm{s}^{-1}$. As a result, $r = 0.05\,\mathrm{s}^{-1}$ somewhere within the range $S_{\mathrm{ice,onset}}$ to $S_{\mathrm{ice,previous}}$. For the calculations that follow, we define a new variable, the ice saturation ratio at which the nucleation rate equals $0.05\,\mathrm{s}^{-1}$ ($S_{\mathrm{ice,r=0.05}}$). $S_{\mathrm{ice,r=0.05}}$ can be calculated with the following equation:

$$S_{\mathrm{ice,r=0.05}} = \frac{\left(S_{\mathrm{ice,previous}} + S_{\mathrm{ice,onset}}\right)}{2}. \tag{3.3}$$

Figures 3.4b and 3.5b show individual $S_{\mathrm{ice,r=0.05}}$ values as a function of surface area. The uncertainty in $S_{\mathrm{ice,r=0.05}}$ includes the difference between $S_{\mathrm{ice,onset}}$ and $S_{\mathrm{ice,previous}}$ as well as the uncertainty in measuring $S_{\mathrm{ice,onset}}$. $S_{\mathrm{ice,onset}}$ and $S_{\mathrm{ice,r=0.05}}$ are very similar, but $S_{\mathrm{ice,r=0.05}}$ is more useful when discussing nucleation rates.

Figures 3.4c and 3.5c show average $S_{\mathrm{ice,r=0.05}}$ values calculated from the data presented in Figs. 3.4b and 3.5b. To determine averages, the data were binned as a function of surface area into equally spaced bins on a logarithmic scale. The uncertainty in the average $S_{\mathrm{ice,r=0.05}}$ values reported in Figs. 3.4c and 3.5c correspond to the 95 % confidence interval for the averages. As can be seen from the figures, the average $S_{\mathrm{ice,r=0.05}}$ values clearly increase with decreasing

surface area. Kanji and Abbatt [2010] observed a similar trend for deposition nucleation.

3.3.3 Fraction of particles nucleated as a function of $S_{\mathrm{ice,r=0.05}}$

A convenient way of displaying the data involves calculating the fraction of particles nucleated in an experiment as a function of S_{ice}. Presenting the data in this manner allows for a direct comparison with the pdf-α scheme, the active site scheme, and the deterministic scheme (see below). Since the number of particles nucleated at $S_{\mathrm{ice,r=0.05}}$ equals 1, the fraction nucleated is calculated by dividing 1 by the total number of particles available to nucleate ice (N_{total}).

In Figs. 3.6a and 3.7a we show the fraction of particles nucleated as a function of $S_{\mathrm{ice,r=0.05}}$ for each of the individual experimental results. Shown in Figs. 3.6b and 3.7b are average fraction nucleated values calculated from the data shown in Figs. 3.6a and 3.7a. To determine averages, the data was binned as a function of $S_{\mathrm{ice,r=0.05}}$ into four equally spaced bins. Figures 3.6b and 3.7b show an increase in fraction nucleated with increasing $S_{\mathrm{ice,r=0.05}}$ as expected.

3.4 Discussion

3.4.1 Single-α scheme

As discussed in Chapter 2, CNT [Pruppacher and Klett, 1997] relates the rate of heterogeneous ice nucleation (j_{het}, in units of $\mathrm{cm}^{-2}\ \mathrm{s}^{-1}$) to the energy barrier for ice cluster formation on the substrate surface:

$$j_{\mathrm{het}} = j_0 \exp\left(-\frac{\Delta G_{\mathrm{act}} f(\alpha)}{kT}\right) = j_0 \exp\left\{-\frac{16\pi\sigma_{i/v}^3}{3kT\left[kTN_i \ln S_{\mathrm{ice}}\right]^2} f_{\mathrm{het}}(\alpha)\right\}, \tag{3.4}$$

where ΔG_{act} is the activation barrier to ice nucleation, $f_{\mathrm{het}}(\alpha)$ is the contact parameter of the cluster on the surface, j_0 is the pre-exponential factor in $\mathrm{cm}^{-2}\ \mathrm{s}^{-1}$, k is the Boltzmann constant, and T is the temperature in degrees Kelvin. $\sigma_{i/v}$ is the ice-vapour interfacial energy in $\mathrm{J\,cm}^{-2}$, N_i is the molecular concentration of ice in cm^{-3}, and S_{ice} is the saturation ratio over

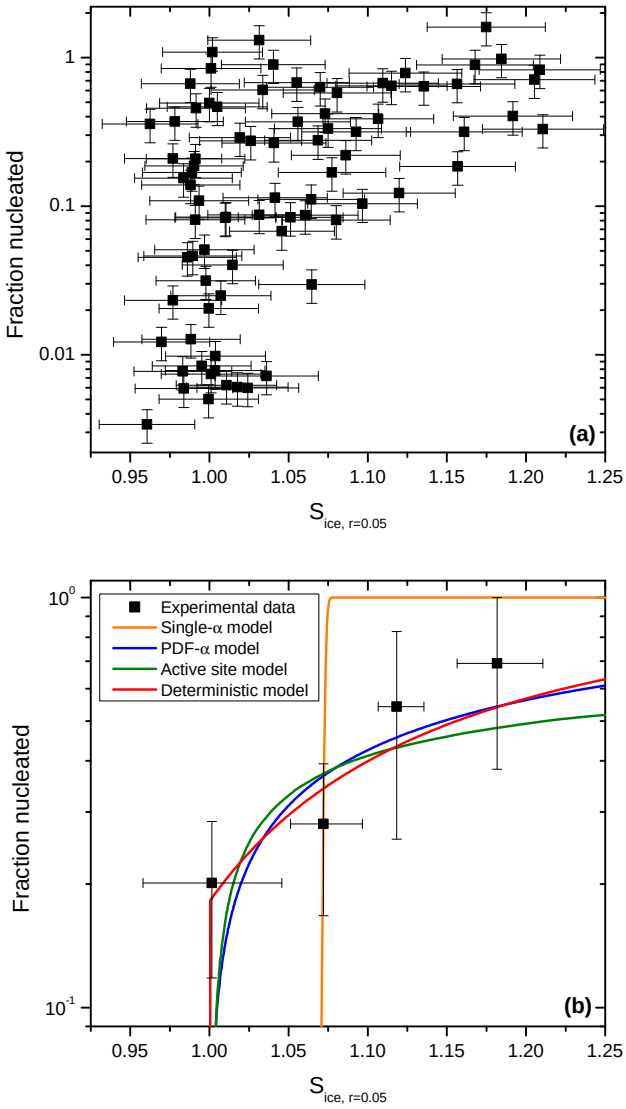

Figure 3.6: Fraction of particles nucleated as a function of $S_{\mathrm{ice,r=0.05}}$ for kaolinite. Panel **(a)** shows the nucleated fraction for the individual experimental results. The y-error was calculated from the uncertainty in the value of $\bar{D}_g$. The x-error represents the uncertainty in $S_{\mathrm{ice,r=0.05}}$. Panel **(b)** shows the average nucleated fraction calculated for four size bins. The range of the data points in each bin is given as the horizontal error and data points represent the average of the $S_{\mathrm{ice,r=0.05}}$ values within each bin. The y-error bar in panel **(b)** represents the 95 % confidence interval of the average nucleated fraction. Fits are shown for the single-α, pdf-α, active site, and deterministic schemes.

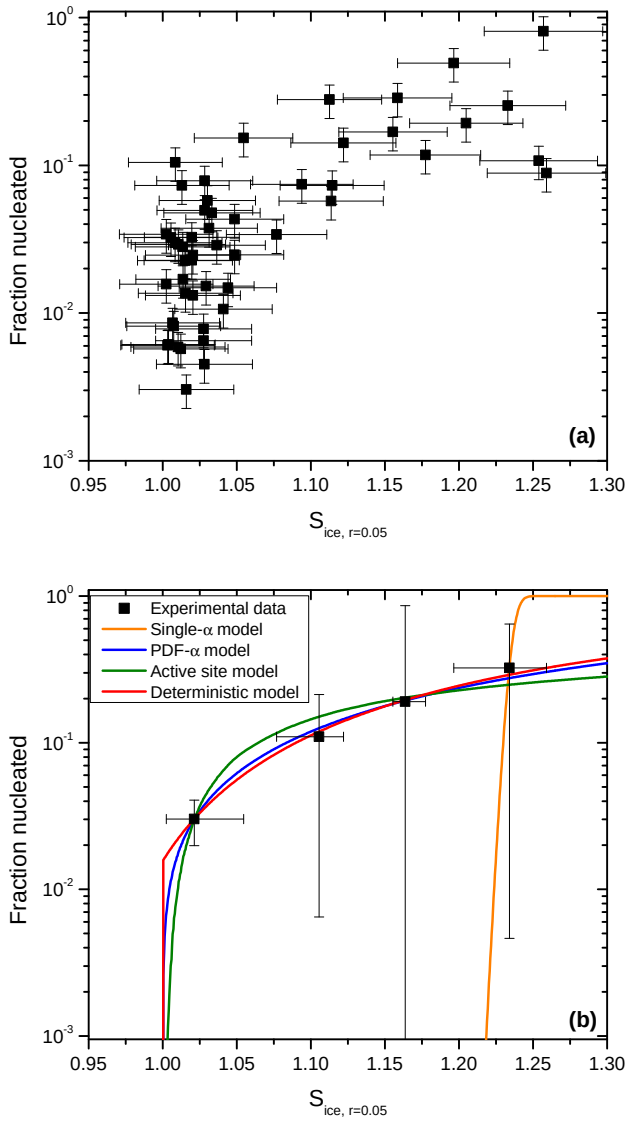

Figure 3.7: Fraction of particles nucleated as a function of $S_{\mathrm{ice,r=0.05}}$ for illite. Panel **(a)** shows the nucleated fraction for the individual experimental results. The y-error was calculated from the uncertainty in the value of $\bar{D}_g$. The x-error represents the uncertainty in $S_{\mathrm{ice,r=0.05}}$. Panel **(b)** shows the average nucleated fraction calculated for four size bins. The range of the data points in each bin is given as the horizontal error and data points represent the average of the $S_{\mathrm{ice,r=0.05}}$ values within each bin. The y-error bar in panel **(b)** represents the 95 % confidence interval of the average nucleated fraction. Fits are shown for the single-α, pdf-α, active site, and deterministic schemes.

the particles.

For particle radii significantly larger than the radius of an ice cluster (a good approximation under our conditions), $f_{\mathrm{het}}(\alpha)$ can be described by the following equation:

$$f_{\mathrm{het}}(\alpha) = \frac{(2+\cos\alpha)(1-\cos\alpha)^2}{4}, \tag{3.5}$$

where α is the contact angle of the ice cluster on the particle surface. The physical meaning of the contact angle is not well understood and it is often used as a means of parameterizing laboratory data.

The heterogeneous nucleation rate can be expressed as a function of area, time and number of nucleation events using the following equation:

$$j_{\mathrm{het}} = \frac{\omega}{A_{\mathrm{total}}\Delta t}, \tag{3.6}$$

where ω is the number of nucleation events, A_{total} is the total surface area of particles in cm^2 and Δt is the time scale of the measurements. Equations (3.4) and (3.6) can be combined to give the following relationship between S_{ice}, area, time and the number of nucleation events:

$$\ln S_{\mathrm{ice}} = \sqrt{\frac{16\pi\sigma_{i/v}^3 f_{\mathrm{het}}(\alpha)}{3kT\ln\left(\frac{A_{\mathrm{total}} j_0 \Delta t}{\omega}\right)}}\frac{1}{N_i kT}. \tag{3.7}$$

Equation (3.7) can be used to predict the relationship between $S_{\mathrm{ice,r=0.05}}$ and surface area. At $S_{\mathrm{ice,r=0.05}}$ the number of nucleation events, ω, is, by definition, 1, and the time for nucleation is 20 s.

In Figs. 3.4c and 3.5c (solid lines) we have calculated $S_{\mathrm{ice,r=0.05}}$ as a function of A_{total} using Eq. (3.7), $\omega = 1$, $\Delta t = 20\,\mathrm{s}$ and different contact angles. We also used an interfacial energy of $1.065 \times 10^{-5}\,\mathrm{J\,cm^{-2}}$ [Pruppacher and Klett, 1997], a pre-exponential factor of $10^{25}\,\mathrm{cm^{-2}\,s^{-1}}$ [Fletcher, 1958, 1959; Pruppacher and Klett, 1997] and a molecular concentration of ice of

3.1×10^{22} cm^{-3} (calculated from the molecular mass and density of ice [Lide, 2001]). Both the values of $\sigma_{i/v}$ and N_i are calculated for hexagonal ice. Recent findings have shown that cubic ice is formed preferentially for homogeneous nucleation [Murray and Bertram, 2006; Murray et al., 2005] but more information is needed to determine the polymorph of ice that is formed by heterogeneous nucleation.

It can be seen in Figs. 3.4c and 3.5c that there is no single contact angle capable of accurately describing the data. Measurements made at high surface areas are described by a low value of the contact angle ($\alpha \approx 3^\circ$ for kaolinite and $\alpha \approx 7^\circ$ for illite). Comparatively, the measurements made at the lowest surface areas are described by a much larger contact angle ($\alpha \approx 14^\circ$ for kaolinite and $\alpha \approx 20^\circ$ for illite).

The single-α scheme can also be used to predict the fraction of particles nucleated as a function of $S_{\mathrm{ice,r=0.05}}$ as in Figs. 3.6b and 3.7b. Equation (3.8) shows the relationship between the fraction of particles nucleated and the heterogeneous nucleation rate [Pruppacher and Klett, 1997]:

$$\frac{N_f}{N_0} = 1 - \int_0^\infty \exp\left[-\pi D^2 \, j_{\mathrm{het}}\left(\alpha, T, S_{\mathrm{ice}}\right) \Delta t\right] p_{\mathrm{num}}\left(D\right) \mathrm{d}D, \tag{3.8}$$

where $\frac{N_f}{N_0}$ is the fraction of particles nucleated, j_{het} is the heterogeneous nucleation rate which can be calculated from Eq. (3.4), D is the diameter of a single kaolinite or illite particle, and $p_{\mathrm{num}}(D)$ is the number distribution calculated from data presented in Fig. 3.3. The value $p_{\mathrm{num}}\left(D\right)\mathrm{d}D$ represents the fraction of particles having a diameter between D and $D + \mathrm{d}D$.

Shown in Figs. 3.6b and 3.7b (orange lines) are fits to the fraction nucleated as a function of $S_{\mathrm{ice,r=0.05}}$ obtained by numerical rectangular integration of Eq. (3.8) and assuming a single contact angle. In these calculations 20 s was used for the time scale of the experiment as done above. It can be seen from Figs. 3.6b and 3.7b that the single-α scheme cannot describe our experimental data. The parameters from the fitting procedure are listed in Tables 3.1 and 3.2.

Table 3.1: Fit parameters obtained for kaolinite. Best fits were obtained by minimizing the weighted sum of squared residuals (WSSR) between the experimental data and the fit function. See text for further discussion on the schemes used.

Scheme	Parameter	Value	WSSR[a]
single-α	α	12.53°	9.443
pdf-α	μ_α	0°	3.888
	σ_α	26.08°	
active site	b	$6.19 \times 10^9 \mathrm{m}^{-2}$	5.081
	β_1	0.01	
	β_2	0.001	
deterministic	A_1	$2.31 \times 10^6 \mathrm{cm}^{-2}$	0.718
	A_2	-0.8845	

[a] Weighted sum of squared residuals

Table 3.2: Fit parameters obtained for illite. Best fits were obtained by minimizing the weighted sum of squared residuals (WSSR) between the experimental data and the fit function. See text for further discussion on the schemes used.

Scheme	Parameter	Value	WSSR[a]
single-α	α	21.75°	9.778
pdf-α	μ_α	28.94°	0.0468
	σ_α	12.75°	
active site	b	$8.70 \times 10^9 \mathrm{m}^{-2}$	0.490
	β_1	0.1351	
	β_2	1.0×10^{-4}	
deterministic	A_1	$1.78 \times 10^6 \mathrm{cm}^{-2}$	0.0190
	A_2	-0.9481	

[a] Weighted sum of squared residuals

3.4.2 Pdf-α scheme

As mentioned above, the pdf-α scheme is a modification of the single-α scheme [Lüönd et al., 2010; Marcolli et al., 2007]. This scheme assumes that a single contact angle can describe ice nucleation on an individual particle, but that a distribution of contact angles exists for an ensemble of particles. Assuming a normal distribution of contact angles, the fraction of nucleated particles is given by

$$\frac{N_f}{N_0} = 1 - \int_0^\infty \int_0^\pi \exp\left[-\pi D^2 \, j_{\mathrm{het}}\left(\alpha, T, S_{\mathrm{ice}}\right) \Delta t\right] p(\alpha) p_{\mathrm{num}}(D) \, \mathrm{d}\alpha \, \mathrm{d}D, \tag{3.9}$$

where $p(\alpha)$ is the normal probability distribution at a particular value of α. The value $p(\alpha)\mathrm{d}\alpha$ is the fraction of particles having a contact angle between α and $\alpha + \mathrm{d}\alpha$. The normal probability distribution is described by the following equation:

$$p(\alpha) = \frac{1}{\sigma_\alpha \sqrt{2\pi}} \exp\left[-\frac{(\alpha - \mu_\alpha)^2}{2\sigma_\alpha^2}\right], \tag{3.10}$$

where μ_α and σ_α are the mean and standard deviation of the distribution, respectively. The value of μ_α is constrained such that $\mu_\alpha \geq 0$ and $p(\alpha)$ is normalized such that $\int_0^\pi p(\alpha)\mathrm{d}\alpha = 1$.

The blue lines in Figs. 3.6b and 3.7b show calculations of the fraction nucleated as a function of $S_{\mathrm{ice,r=0.05}}$ using Eq. (3.9). Similar to the previous calculations, an experimental time of 20 s was used. The data was fit by numerical rectangular integration of Eq. (3.9) and by varying the parameters μ_α and σ_α.

The best fit to the kaolinite data (blue line in Fig. 3.6b) gave a mean contact angle (μ_α) of 0° and a width (σ_α) of 26.1°. The best fit to the illite data (blue line in Fig. 3.7b) gave a mean contact angle of 28.9° and a standard deviation of 12.8°. The distribution of contact angles are shown (black lines) in Fig. 3.8 for kaolinite and Fig. 3.9 for illite. Figures 3.6b and 3.7b show that the pdf-α scheme agrees with the experimental data within the uncertainty of the measurements.

3.4.3 Active site scheme

The third method used to fit the experimental data was the active site scheme, which is a modification of the single-α scheme that includes the existence of active sites [Fletcher, 1969; Gorbunov and Kakutkina, 1982; Han et al., 2002; Lüönd et al., 2010; Marcolli et al., 2007; Niedermeier et al., 2011b]. The equations presented here are the same as those presented by Lüönd et al. [2010].

In contrast to the previous schemes, the active site scheme assumes ice nucleation occurs more readily on small sites on the particle surface as opposed being equally probable anywhere on the particle surface. For consistency, we assume that the size of an active site is constant

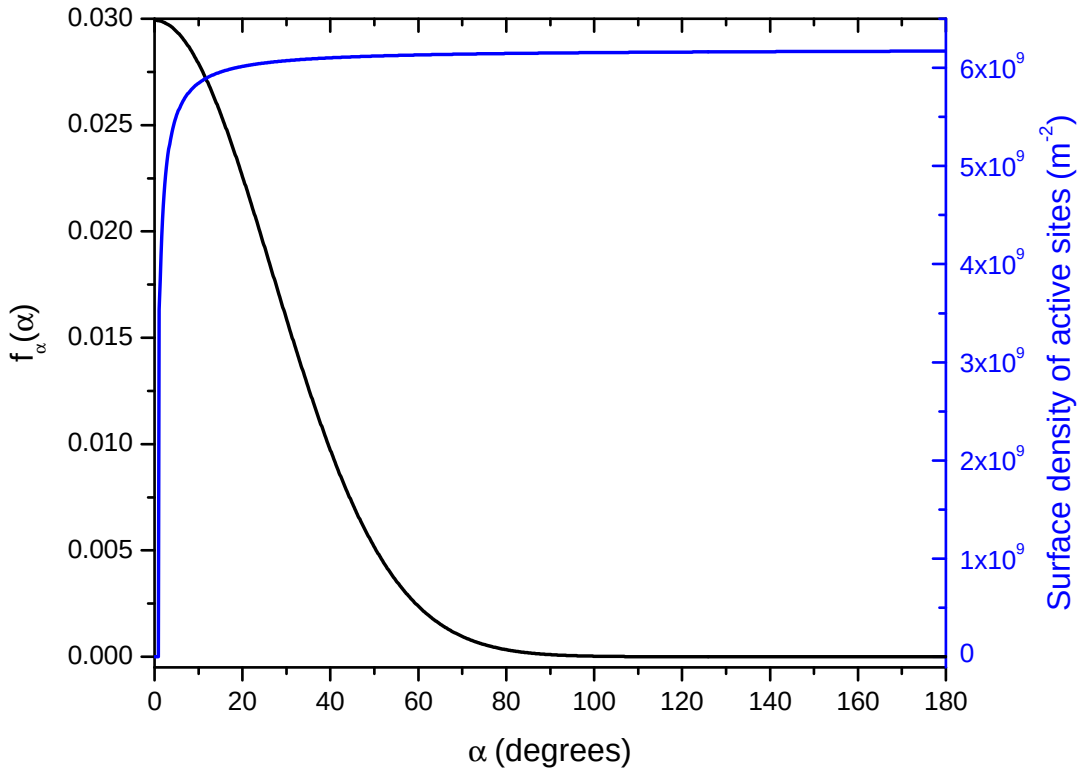

Figure 3.8: Probability distribution function for the pdf-α scheme and surface density of active sites, $\rho(\alpha)$, for the active site scheme. Shown are the results for kaolinite particles.

and equal to 6 nm^2 as done by Lüönd et al. [2010]. This is calculated from the critical ice cluster size determined for homogeneous nucleation of liquid water at 239 K using classical nucleation theory. The active site scheme assumes that the probability of ice nucleation on an active site is defined by a contact angle, α_i, and this contact angle can vary from site to site.

Similar to Eq. (3.8) presented above, the probability of nucleation on a single active site with contact angle, α, is

$$P_{\text{site}}(\alpha) = 1 - \exp\left[-A_\alpha J_{\text{het}}(\alpha, T, S_{\text{ice}})\,\Delta t\right], \tag{3.11}$$

where $P_{\text{site}}(\alpha)$ is the probability of nucleation, $j_{\text{het}}(\alpha, T, S_{\text{ice}})$ is the temperature, saturation and

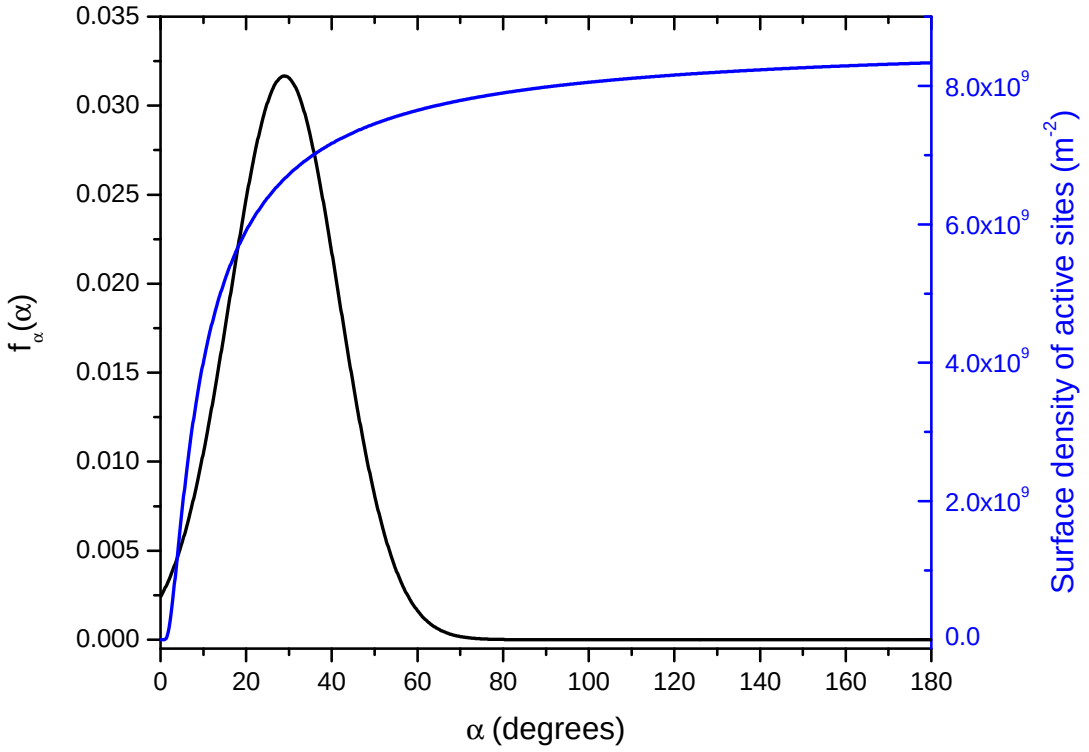

Figure 3.9: Probability distribution function for the pdf-α scheme and surface density of active sites, $\rho(\alpha)$, for the active site scheme. Shown are the results for illite particles.

contact angle dependent heterogeneous nucleation rate given by Eq. (3.4), A_α is the area of the active site ($6\,\mathrm{nm}^2$), and Δt is the time of observation. Similarly, the probability that nucleation does not occur on a single active site with contact angle α is

$$\bar{P}_{\mathrm{site}}(\alpha) = \exp\left[-A_\alpha J_{\mathrm{het}}(\alpha, T, S_{\mathrm{ice}})\,\Delta t\right]. \tag{3.12}$$

The probability of nucleation of a single particle is described by the following equation, which takes into account the assumptions that a single particle can have multiple active sites and

active sites can have a range of contact angles:

$$P_{\text{particle}}(S_{\text{ice}}) = 1 - \prod_{i=1}^{m} \bar{P}_{\text{site}}(\alpha_i) = 1 - \prod_{i=1}^{m} \exp\left[-A_{\alpha_i} J_{\text{het}}(\alpha_i, T, S_{\text{ice}})\,\Delta t\right], \tag{3.13}$$

where $P_{\text{particle}}(S_{\text{ice}})$ is the probability of nucleation of a single particle and $\bar{P}_{\text{site}}(\alpha_i)$ is the probability that an active site with a contact angle of α_i does not nucleate ice. A_{α_i} is the total surface area of active sites with a contact angle in the range $(\alpha_i,\ \alpha_i + \Delta\alpha)$ where $\Delta\alpha$ is the width of the individual bin such that the total number of bins is equal to m. A_{α_i} represents the summation of all active sites within the specified range, each with an area of 6 nm^2. Therefore, A_{α_i} is an integer multiple of the single active site area $\left(A_{\alpha_i} = n_i\left(6\text{nm}^2\right)\right)$.

The average number of active sites on a single particle in the range $(\alpha_i, \alpha_i + \Delta\alpha)$, $\bar{n}_i$, is given by

$$\bar{n}_i = \pi D^2 \rho(\alpha_i)\,\Delta\alpha, \tag{3.14}$$

where D is the diameter of the particle and $\rho(\alpha)$ is the contact angle dependent surface density of active sites (i.e. number of active sites per unit surface area per unit contact angle interval). The number of active sites on a single particle, n_i, in the range $(\alpha_i, \alpha_i + \Delta\alpha)$, was assigned using Poisson distributed random variables with the expectation value given by Eq. (3.14). The n_i values determined from Poisson statistics were then used in Eq. (3.13) to determine the nucleation probabilities, $P_{\text{particle}}(S_{\text{ice}})$, of a single particle. This whole process was then repeated 1000 times to determine nucleation probabilities of an ensemble of 1000 particles. The diameter of each particle was assigned using uniform random numbers in the range [0,1] and the cumulative distribution functions calculated from the data presented in Fig. 3.3. The nucleated fraction was then determined using the following equation:

$$\frac{N_f}{N_0} = \frac{1}{1000} \sum_{j=1}^{j=1000} P_{\text{particle, j}}\,(S_{\text{ice}}). \tag{3.15}$$

As was done by Marcolli et al. [2007] and Lüönd et al. [2010], the surface density of active

sites was described using a three parameter exponential function of the following form:

$$\rho(\alpha) = b \exp\left(\frac{-\beta_1}{\alpha - \beta_2}\right). \tag{3.16}$$

The experimentally determined nucleated fractions were fit to the active site scheme by varying the parameters, b, β_1, and β_2. Results are shown (green lines) in Figs. 3.6b and 3.7b for kaolinite and illite, respectively. As can be seen in the figures, the active site scheme fits the data within the experimental error. Fit parameters are reported in Table 3.1 and 3.2 for kaolinite and illite, respectively. Other combinations of two of the fitting parameters, β_1 and β_2, were found which provided equivalent fits to the ones presented (i.e. no single set of parameters best described the data). This was attributed to the low number of data points upon which the fits are based.

The fact that the experimental data is in agreement with the active site scheme is consistent with recent computer simulations of ice nucleation at the molecular level. These simulations show that the good ice nucleation characteristics of mineral dust is not likely due to the crystallographic match between the mineral surface and hexagonal ice, but rather may be due to ice nucleation on defects such as trenches [Croteau et al., 2008, 2010; Hu and Michaelides, 2007].

3.4.4 Deterministic scheme

A final scheme used here is the deterministic scheme [Connolly et al., 2009; Lüönd et al., 2010]. For deposition nucleation, we assume that the particles have a surface density of active sites, n_s, that is a function of $S_{\mathrm{ice,r=0.05}}$, but independent of temperature over the narrow range of temperatures investigated ($239 - 242\,\mathrm{K}$). The assumption of temperature independence for n_s should be reasonable based on previous measurements of $S_{\mathrm{ice,onset}}$ as a function of temperature for kaolinite particles [Eastwood et al., 2008], which show that $S_{\mathrm{ice,onset}}$ is relatively insensitive to temperature over the range of $236 - 246\,\mathrm{K}$. It is also assumed that the fraction of particles nucleated at a given S_ice is independent of time but related to $n_\mathrm{s}(S_\mathrm{ice})$ through the following

equation:

$$\frac{N_f}{N_0} = 1 - \int_0^\infty \exp\left[-\pi D^2 n_s\left(S_{ice}\right)\right] p_{num}\left(D\right) \mathrm{d}D. \tag{3.17}$$

The surface density of active sites, $n_s\left(S_{ice}\right)$, was described by [Connolly et al., 2009; Lüönd et al., 2010],

$$n_s\left(S_{ice}\right) = \begin{cases} 0, & S_{ice} \leq -A_2 \text{ or } S_{ice} \leq 1 \\ A_1\left(S_{ice} + A_2\right)^2, & \text{otherwise.} \end{cases} \tag{3.18}$$

Using Eqs. (3.17) and (3.18), the experimentally determined nucleated fractions were fit using the parameters A_1 and A_2. Good agreement was found between the experimental data and the deterministic scheme (red lines in Figs. 3.6b and 3.7b). Fit parameters can be found in Tables 3.1 and 3.2 for kaolinite and illite, respectively.

3.4.5 Sensitivity of the results to the assumption of spherical particles

The calculations above were carried out with the assumption that the surface area of a particle equals the geometric surface area (i.e. the particles are spherical). We assume this is a lower limit to the total surface area available for nucleation. Based on scanning electron microscope measurements of a limited number of mineral particles, we estimate that an upper limit to the surface area of the particles equals the geometric surface area multiplied by a factor of 50 [Eastwood et al., 2008]. We have reanalyzed the experimental data and redone the calculations with the assumption that the surface area of the particles equals the geometric surface area multiplied by 50. The results from this analysis and calculations are shown in Appendix A (Tables A.1 and A.2 and Figs. A.1 - A.4).

In short, when using a geometric surface area multiplied by 50, the single-α scheme does not describe the data but the pdf-α scheme, active site scheme, and deterministic scheme all fit the data within the experimental error. The fit parameters for the single-α and pdf-α schemes vary by less than 3 % compared with the parameters presented in Tables 3.1 and 3.2. For the deterministic scheme, the parameter A_2 is the same as presented in Tables 3.1 and 3.2 and the parameter A_1 is reduced by a factor of 50.

3.4.6 Comparisons with previous measurements

Previous studies have also used various nucleation data to test whether or not the single-α scheme can be used to accurately describe heterogeneous ice nucleation data for mineral dust particles. Several studies have shown that modifications to the single-α scheme are required for accurate predictions of heterogeneous nucleation data [Archuleta et al., 2005; Hung et al., 2003; Lüönd et al., 2010; Marcolli et al., 2007; Welti et al., 2009]. Most similar to our studies, Welti et al. [2009] studied ice nucleation on mineral dust particles, including illite and kaolinite, in the deposition mode. Relative humidities with respect to ice required to activate 1% of the dust particles as ice nuclei (IN) were reported as a function of temperature. An explicit size dependence of the ice formation efficiency was observed for all dust types. Particles 800nm in diameter required the lowest S_{ice} to activate. Similar to the main conclusions in our study, these authors found that a single contact angle could not describe freezing results for different particle diameters of a single mineral.

Murray et al. [2011] investigated immersion freezing by kaolinite particles as a function of dust concentration and cooling rate. In contrast with the references mentioned above, the data from this study were consistent with classical nucleation theory and the assumption of a single contact angle (the single-α scheme). The source of the kaolinite material used by Murray et al. was the Clay Minerals Society, which is a different source compared to our experiments. In addition, the work of Murray et al. investigated immersion freezing while our work examined deposition nucleation. Future studies investigating the ice nucleation properties of different mineral sources may provide some insight into the apparent discrepancies.

3.5 Conclusions and atmospheric implications

Deposition nucleation of ice on kaolinite and illite particles, two abundant minerals in the atmosphere, was investigated. The onset S_{ice} conditions for ice nucleation were a strong function of the surface area available for ice nucleation. For example, in the kaolinite experiments onset S_{ice} values ranged from 100 % to 125 % depending on the surface area used in the experiments.

The surface area dependent results were used to test the applicability of classical nucleation theory with a single contact angle as a method to parameterize heterogeneous ice nucleation data. The surface area dependent data could not be described accurately using this scheme. These results add to the growing body of evidence that suggests that, in many cases, the single-α scheme is not appropriate for predictions of heterogeneous nucleation. The results also suggest that caution should be applied when using contact angles determined from the single-α scheme and onset data. This is because different contact angles can be derived from onset S_{ice} data and the single-α scheme depending on the surface area used in the experiments. As an example, the contact angle consistent with our kaolinite data varied from 3° to 14° depending on the surface area. Fits were also performed using the pdf-α scheme, the active site scheme, and the deterministic scheme. In contrast to the single-α scheme, the other schemes used all fit the data within experimental uncertainties. Parameters from the fits to the data were presented. These parameters are applicable to the temperature range studied (239 - 242 K). Further studies are needed to determine if the parameters apply to temperatures outside this range.

Chapter 4

Immersion freezing of supermicron mineral dust particles: freezing results, testing different schemes for describing ice nucleation, and ice nucleation active site densities

4.1 Introduction

Ice nucleation in the atmosphere can influence precipitation and the properties of clouds, which can in turn influence the radiative properties of the Earth-atmosphere system [DeMott et al., 2010; Denman et al., 2007; Lohmann and Feichter, 2005]. A better understanding of the conditions necessary for ice nucleation may enable more accurate modelling of clouds and precipitation and may reduce uncertainties in climate models. Ice nucleation in the atmosphere can occur through two mechanisms: homogeneous or heterogeneous ice nucleation. Homogeneous ice nucleation occurs within a supercooled solution drop in the absence of insoluble ice nuclei

(IN) and is limited to temperatures $<$ -37 $^{\circ}$C, whereas heterogeneous ice nucleation requires the presence of an IN and can occur at warmer temperatures. Heterogeneous ice nucleation can occur through several different modes: deposition, immersion, condensation and contact nucleation [Vali, 1985]. A detailed description of these different modes can be found in Chapter 1. Here we focus on immersion freezing of pure water drops with mineral dust inclusions.

Based on field, laboratory, and modelling studies, mineral dust is known to be an important heterogeneous ice nuclei in the atmosphere. For example, previous field studies have observed that mineral dust particles are an important component of the atmospheric IN population [Cziczo et al., 2004, 2013; DeMott et al., 2003b,a; Ebert et al., 2011; Isono et al., 1959; Kumai, 1961; Prenni et al., 2009; Pruppacher and Klett, 1997; Richardson et al., 2007; Sassen et al., 2003; Seifert et al., 2010; Targino et al., 2006]. Many laboratory studies have also found that mineral dust particles are efficient IN [Atkinson et al., 2013; Connolly et al., 2009; Eastwood et al., 2008; Hoose and Möhler, 2012; Knopf and Koop, 2006; Lüönd et al., 2010; Marcolli et al., 2007; Murray et al., 2011; Niedermeier et al., 2010; Pinti et al., 2012; Roberts and Hallett, 1968; Welti et al., 2012; Wheeler and Bertram, 2012; Yakobi-Hancock et al., 2013; Zimmermann et al., 2008]. In addition, modelling studies have shown that mineral dust particles can cause ice to form in clouds at warmer temperatures than required for homogeneous freezing [Diehl and Wurzler, 2010; Hoose et al., 2008, 2010a,b; Lohmann and Diehl, 2006].

To accurately implement ice nucleation in atmospheric models, a suitable theory or scheme is desired to represent freezing data in atmospheric models. Recent work has illustrated that the cloud properties predicted with atmospheric models are sensitive to the scheme used to describe ice nucleation in the models [Eidhammer et al., 2009; Ervens and Feingold, 2012; Kulkarni et al., 2012; Wang and Liu, 2014; Wang et al., 2014]. For example, Ervens and Feingold [2012] implemented five different schemes for ice nucleation into an adiabatic parcel model and found that for polydisperse IN, differences of up to an order of magnitude are seen in the ice number concentration and ice water content of a cloud depending on the scheme used. Since atmospheric modelling shows that predictions are sensitive to schemes for describing

ice nucleation, information on which scheme is best able to reproduce freezing data would be useful. Relative rankings of the different schemes in terms of ability to reproduce freezing data may be useful when deciding which schemes are to be used in modelling studies and when considering trade-offs between accuracy and computational efficiency.

Listed below are four different schemes that have been used in the past to represent laboratory data in atmospheric models. These schemes have been discussed in Chapter 3 and are only briefly discussed here. The first scheme, the single-α scheme [Fletcher, 1958; Pruppacher and Klett, 1997], contains one parameter and is based on classical nucleation theory. Nucleation is assumed to be a stochastic process and can occur with equal probability anywhere on a particle surface. The nucleation ability of a particle is described with a single parameter, the contact angle (α). The second scheme, the pdf-α scheme [Lüönd et al., 2010; Marcolli et al., 2007], is a modification of the single-α scheme allowing for a distribution of contact angles among an ensemble of particles. The third scheme, the active site scheme [Fletcher, 1969; Lüönd et al., 2010; Niedermeier et al., 2011b], further extends the single-α scheme by allowing nucleation to occur only on small sites on the particle surface, termed "active sites". A distribution of these active sites among the particles is assumed to be responsible for the freezing behaviour. The final scheme used here is the deterministic scheme [Connolly et al., 2009] which, unlike the previous schemes, is not derived from classical nucleation theory. Instead, nucleation is assumed to occur instantaneously on a particle upon reaching a characteristic freezing temperature.

There have been several previous studies that have compared laboratory results of mineral dust freezing properties with different schemes for describing ice nucleation [Broadley et al., 2012; Lüönd et al., 2010; Marcolli et al., 2007; Murray et al., 2011; Niedermeier et al., 2010; Welti et al., 2012; Wheeler and Bertram, 2012]. However, there is still no consensus in terms of which scheme is best able to reproduce laboratory freezing data. Here we investigate the immersion freezing of size-selected Arizona Test Dust (ATD) and kaolinite particles with a majority of diameters in the supermicron mode. The new size-selected freezing data is used

to test the four different schemes discussed above (single-α scheme, pdf-α scheme, active site scheme, and deterministic scheme).

In addition to testing different schemes for describing ice nucleation, we also determined from our immersion freezing data the ice nucleation active site (INAS) density of the size-selected supermicron mineral dust particles studied. This is the first study to determine INAS densities of size-selected supermicron dust particles. This information is compared to INAS densities previously determined in the literature. INAS densities can be used to summarize the freezing properties of particles, to determine the relative importance of different types of atmospheric particles, and to make atmospheric predictions. As pointed out by Hoose and Möhler [2012], the size dependence of INAS densities has not been studied carefully in the past. If there is a difference between INAS densities for submicron and supermicron particles, then this needs to be considered when using INAS values for atmospheric predictions and for comparing different types of IN.

Kaolinite was chosen for these studies because it makes up a significant portion of atmospheric mineral dust (up to 60 %) [Claquin et al., 1999; Glaccum and Prospero, 1980]. In addition, the freezing properties of kaolinite particles has been studied extensively as an ice nucleus in the laboratory [Friedman et al., 2011; Hoffer, 1961; Lüönd et al., 2010; Murray et al., 2011; Pinti et al., 2012; Pitter and Pruppacher, 1973; Roberts and Hallett, 1968; Welti et al., 2009; Zimmermann et al., 2008]. Since the kaolinite used here (Clay Minerals Society (CMS) KGa-1b) contains very little contamination by other mineral types (96 % kaolinite [Chipera and Bish, 2001]), this mineral is suited to test the single component stochastic scheme (single-α) discussed above. ATD was chosen for these studies because it is a multi-component dust [Broadley et al., 2012] (like natural atmospheric dust) and because it contains minerals that have been observed in natural mineral dust [Broadley et al., 2012; Claquin et al., 1999; Glaccum and Prospero, 1980] (see Fig. 1.4 in Chapter 1 for the mineral composition of ATD). In addition, many investigations of immersion freezing have used ATD, which provides a large dataset for comparison purposes [Connolly et al., 2009; Cziczo et al., 2009; Hoyle et al., 2011;

Kanji and Abbatt, 2010; Knopf and Koop, 2006; Koehler et al., 2010; Koop and Zobrist, 2009; Marcolli et al., 2007; Niedermeier et al., 2010, 2011a; Niemand et al., 2012; Reitz et al., 2011; Welti et al., 2009].

4.2 Experimental

4.2.1 Freezing measurements

The immersion freezing of dust particles was measured using an optical microscope coupled to a flow cell. Figure 3.1 shows a schematic of the instrumental setup. The flow cell used here has both temperature and humidity control and has been used previously to measure ice nucleation in both the immersion and deposition modes [Chernoff and Bertram, 2010; Dymarska et al., 2006; Eastwood et al., 2008, 2009; Haga et al., 2013; Iannone et al., 2011; Wheeler and Bertram, 2012]. The apparatus is based in part on an earlier design that used an optical microscope coupled to a freezing cell to investigate homogeneous freezing [Koop et al., 2000]. Below is a brief description of the apparatus used here and the experimental protocol.

Particles of interest were deposited on a hydrophobic glass slide (Hampton Research). The glass slide containing the dust particles was then placed at the bottom of the flow cell. The latter was contained in an aluminum block which allowed for accurate control of the temperature. A gas stream was passed over the particles to control the humidity to which the particles were exposed. The flow cell used in the present study was modified from that shown in Fig. 3.1 by placing a gold coated silicon wafer between the Al block and the glass slide containing the sample to provide better contrast in the optical images. The addition of the silicon wafer did not produce a difference in freezing temperature which was confirmed by measuring the homogeneous freezing of pure water drops ($\sim 100\,\mu$m diameter) both with and without the silicon wafer. The median homogeneous freezing temperatures were not statistically different with and without the silicon wafer. The particles inside the flow cell were observed using an optical microscope (Zeiss Axiolab 50X magnification).

The experimental procedure began by increasing the humidity to above water saturation

in order to condense water on the particles held at a constant temperature of 0 °C. After the drops were grown, the relative humidity was decreased in order to slightly evaporate the drops allowing more space between each drop. After partial evaporation, the size of the drops ranged from $10\,\mu$m and $70\,\mu$m. The temperature of the cell was then lowered at a constant rate of $10\,^{\circ}\mathrm{C\,min^{-1}}$ until all the drops froze. A cooling rate of $10\,^{\circ}\mathrm{C\,min^{-1}}$ was chosen in order to reduce the amount of vapour transfer between frozen and unfrozen drops during the course of a single experiment. Video of the drops was recorded throughout the entire experiment. Video recorded during water condensation was used to determine the surface area of mineral dust particles within each drop while video taken during freezing was used to determine the freezing temperature of each drop.

Figure 4.1 shows the temperature profile used for these measurements. Figure 4.2 shows the particles at different steps of the experiment with the Roman numerals indicating the corresponding time and temperature in Fig. 4.1. From top to bottom, the images correspond to the drops at the beginning of an experiment, the drops after water condensation and evaporation, the ice crystals after freezing of all the drops, and the remaining particles after melting of the ice crystals and evaporation of the drops.

4.2.2 Sample generation

ATD (Ultrafine A1) was acquired from Powder Technologies Inc. and kaolinite (KGa-1b) was acquired from the Clay Minerals Society (CMS). We employed a dry generation method here in order to more accurately represent freshly emitted mineral dust. Studies have shown that the method of sample generation (wet versus dry generation) can affect both the CCN and IN activity of mineral dust particles [Herich et al., 2009; Koehler et al., 2010], most likely due to the dissolution of soluble material on the particle surface during wet generation methods. The dust samples were aerosolized using a fluidized bed (TSI model 3400A) with the cyclone attachment removed. The aerosolized sample was then passed through a six-stage Andersen cascade impactor with a hydrophobic glass slide placed on the fourth stage of the impactor.

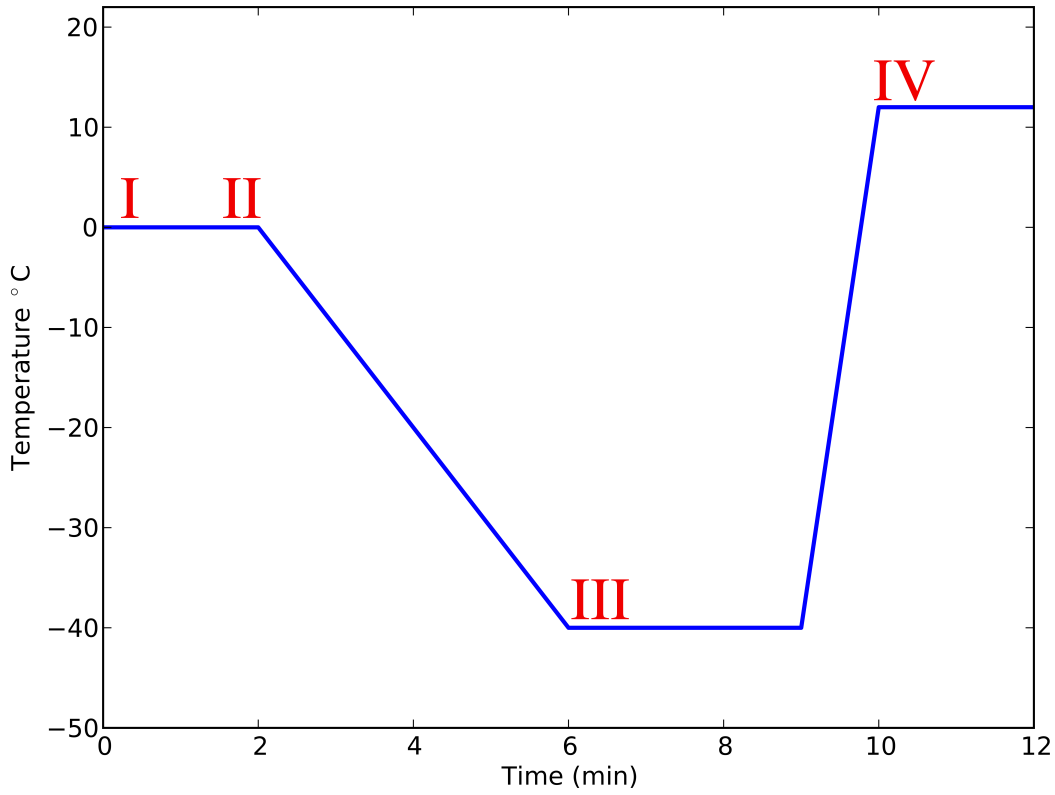

Figure 4.1: Temperature profile used in the freezing experiments. Labels correspond to conditions at which the images in Fig. 4.2 were recorded.

The fourth stage of the impactor has a nominal aerodynamic size cut of $2.0 - 3.5\,\mu$m when operated at 28 lpm [Andersen, 1958]. This corresponds to a geometric diameter size cut of $1.3 - 2.2\,\mu$m for mineral dust, assuming an average density of $2.5\,\mathrm{g\,cm^{-3}}$.

4.2.3 Surface area per drop

Surface areas of solid particles contained in each drop were determined from images recorded during the freezing experiments before and after condensing water. First, the individual drops were identified from images recorded after condensing water (see row II from Fig. 4.2). Each drop was then traced backwards in time to when no water was condensed on the slide (row I from Fig. 4.2) to determine which dust particles were contained within each drop. This is illustrated in Fig. 4.2, row I, where the green traces outline the dust particles contained in each

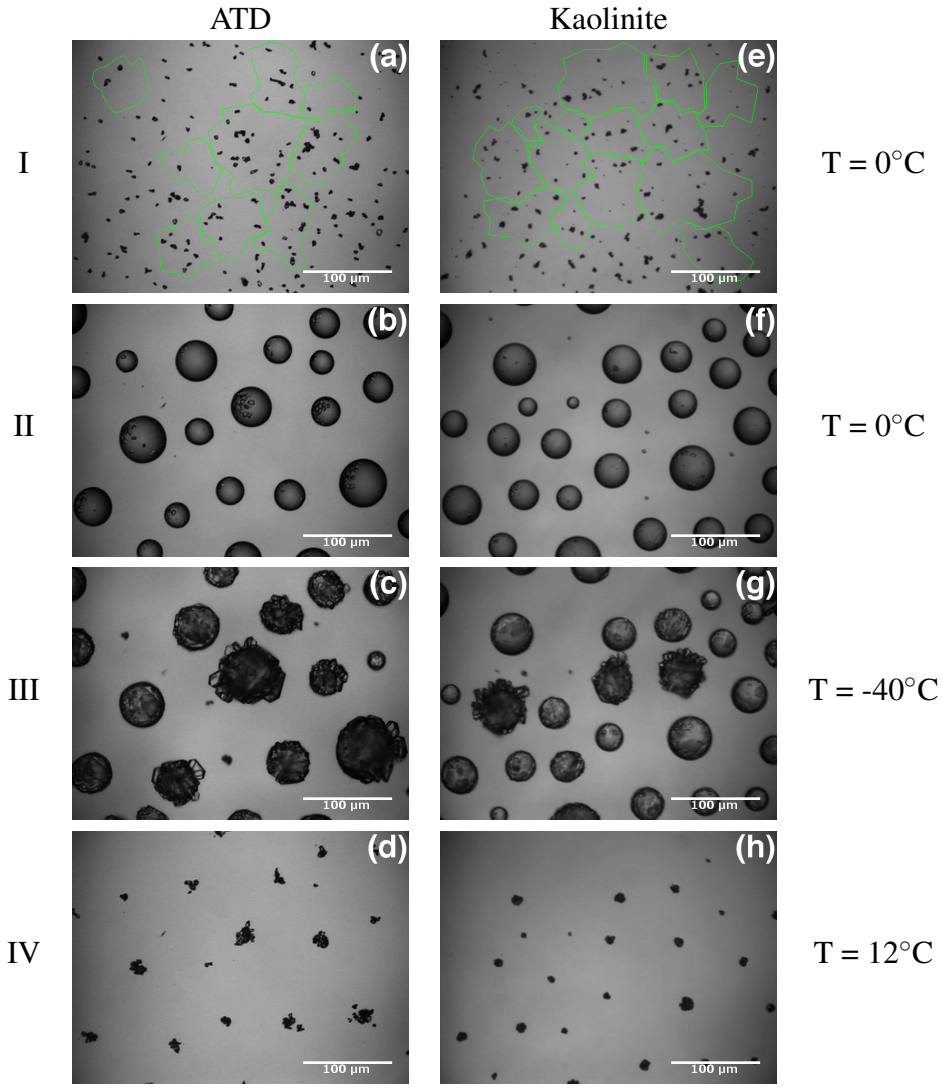

Figure 4.2: Example of optical images collected during a freezing experiment. Panels (**a**) - (**d**) show images from an ATD experiment while panels (**e**) - (**h**) show images from a kaolinite experiment. Rows I-IV correspond to particles before condensing water, particles after condensing water, drops after freezing, and inclusions contained in each drop after evaporation, respectively. The green traces in row I represent the area included in each drop in row II. See text for further details. Labels I-IV can be used to determine the temperature and time in the freezing experiment from Fig. 4.1.

drop. Only those drops where all of the particles were contained within the original field of view were included in the analysis. The surface area of dust contained within each drop was measured using image processing software (ImageJ [Rasband, 1997-2014]), resulting in the projected 2-dimensional geometric area of dust contained in each drop. In order to relate the projected 2-dimensional area to a 3-dimensional geometric surface area, the area measured was scaled by a factor of 4 (which assumes spherical particles).

4.2.4 Size distribution of the mineral dust particles

In experiments separate from the freezing experiments discussed above, size distributions of the mineral dust particles were determined using scanning electron microscopy (SEM; Hitachi S-2600N). Hydrophobic glass slides containing the mineral dust particles were prepared using the same procedure outlined above for the freezing experiments. A total of 81 separate slides were analyzed, and the projected 2-dimensional area of 5243 individual particles deposited on the glass slides was determined from the SEM images. The corresponding data were used to obtain the number and surface area distribution of the particles for both mineral dusts. High resolution SEM images (Hitachi S-4700) of the individual dust particles were also obtained to examine the morphology of the dust particles.

4.3 Results and discussion

4.3.1 Surface area and size distribution of minerals

The size distributions measured by SEM are shown in Figs. 4.3a and 4.4a for ATD and kaolinite, respectively. Based on these distributions, 15% of the ATD particles and 33% of the kaolinite particles have a diameter below $1\,\mu$m. This represents less than 0.5% and 2% of the total measured surface areas for ATD and kaolinite respectively, indicating that a large fraction of the surface area of the particles studied lies in the supermicron range. The particle sizes obtained for kaolinite and ATD are slightly larger than was predicted by the specifications of the Andersen impactor ($1.3-2.2\,\mu$m), likely due to the non-spherical nature of the dust particles

(see SEM images of individual particles in Figs. 4.3b and 4.4b) or charging of the mineral dust particles during the aerosolization process with the fluidized bed. High resolution SEM images of ATD and kaolinite particles are shown in Figs. 4.3b and 4.4b.

Shown in Figs. 4.5 and 4.6 are the distribution of surface areas per drop in the freezing experiments. Also shown is the number of particles per drop calculated using the mean particle diameter obtained from SEM images (mean diameter 3.0 and 2.5 μm for ATD and kaolinite particles, respectively). Based on Figs. 4.5 and 4.6, the number of particles per drop in the freezing experiments ranged from approximately 1-100.

4.3.2 Freezing results

Prior to studying the freezing of drops with ATD or kaolinite inclusions, we first measured freezing of drops (average size of 30 μm) without inclusions (stars in Figs. 4.7 and 4.8). Measurements of the melting point of pure ice were used to correct the temperature of all freezing measurements. Repeated melting point measurements gave a standard deviation of 0.06 °C. This indicates the uncertainty in the temperature measurements obtained with this apparatus. The corrected median freezing temperature of the drops without inclusions was -37.7 ± 0.2 °C. This temperature is within 0.1 °C of the median freezing temperature of 30 μm pure water drops calculated using Eq. 7-51 from Pruppacher and Klett [1997] and parameterizations for ice and water properties from Pruppacher and Klett [1997] and Zobrist et al. [2007]. The agreement between our results and the calculated values indicates the hydrophobic surface does not cause significant heterogeneous freezing and the results for drops without inclusions correspond to homogeneous freezing. The median homogeneous freezing temperature reported here is colder than previously reported using the same apparatus [Iannone et al., 2011]. This difference is due to the smaller drops used here compared to those used by Iannone et al. [2011].

In the heterogeneous freezing experiments, freezing occurred by both immersion freezing and contact freezing. Here immersion freezing refers to freezing of drops by IN immersed in the liquid drops, and contact freezing refers to freezing of liquid drops by contact with neigh-

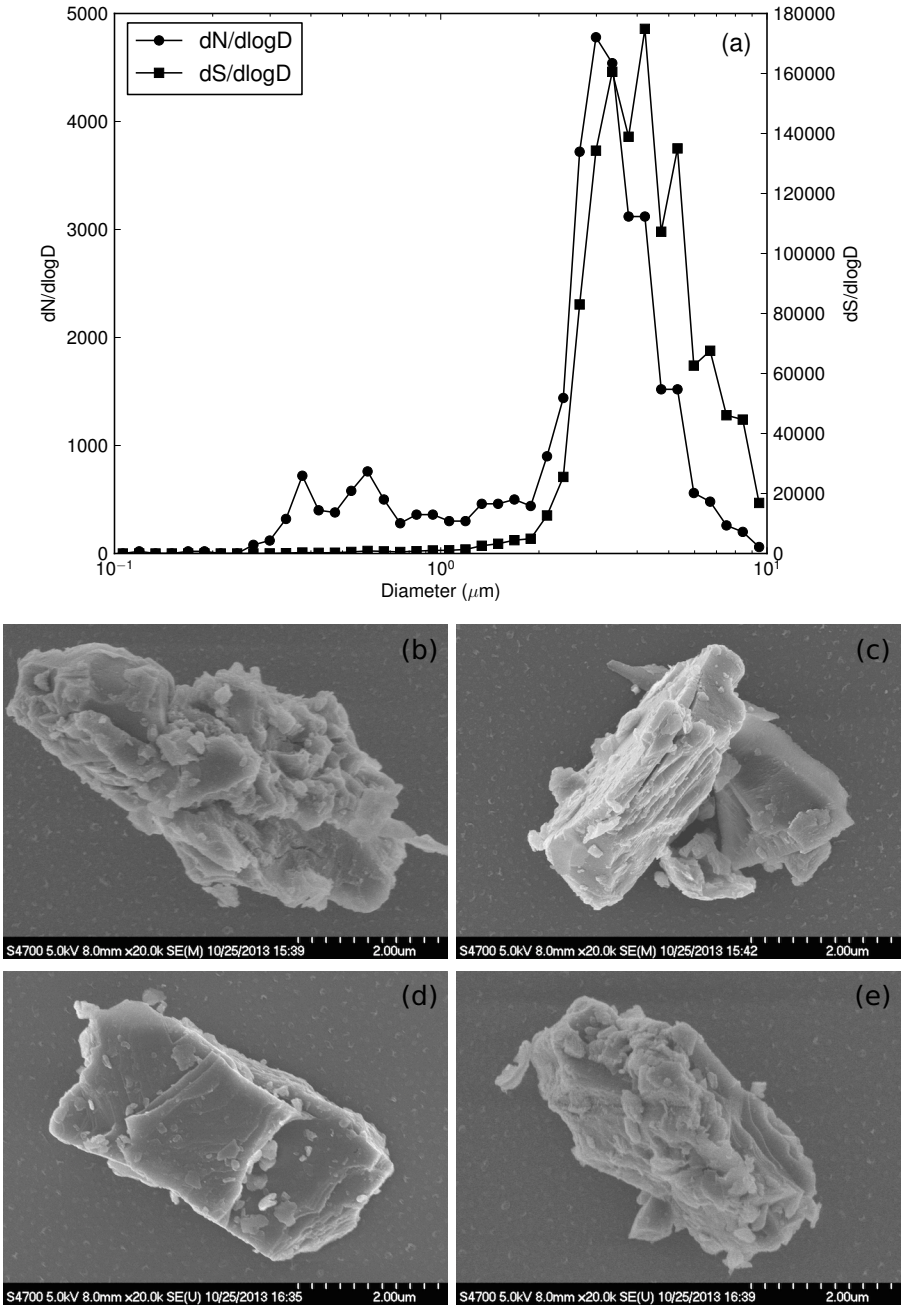

Figure 4.3: (**a**) Size distribution of ATD measured by SEM. Shown are the number, N, distribution (closed circles) and the surface area, S, distribution (closed squares) functions. (**b**) - (**e**) SEM images of individual ATD particles impacted on the slides.

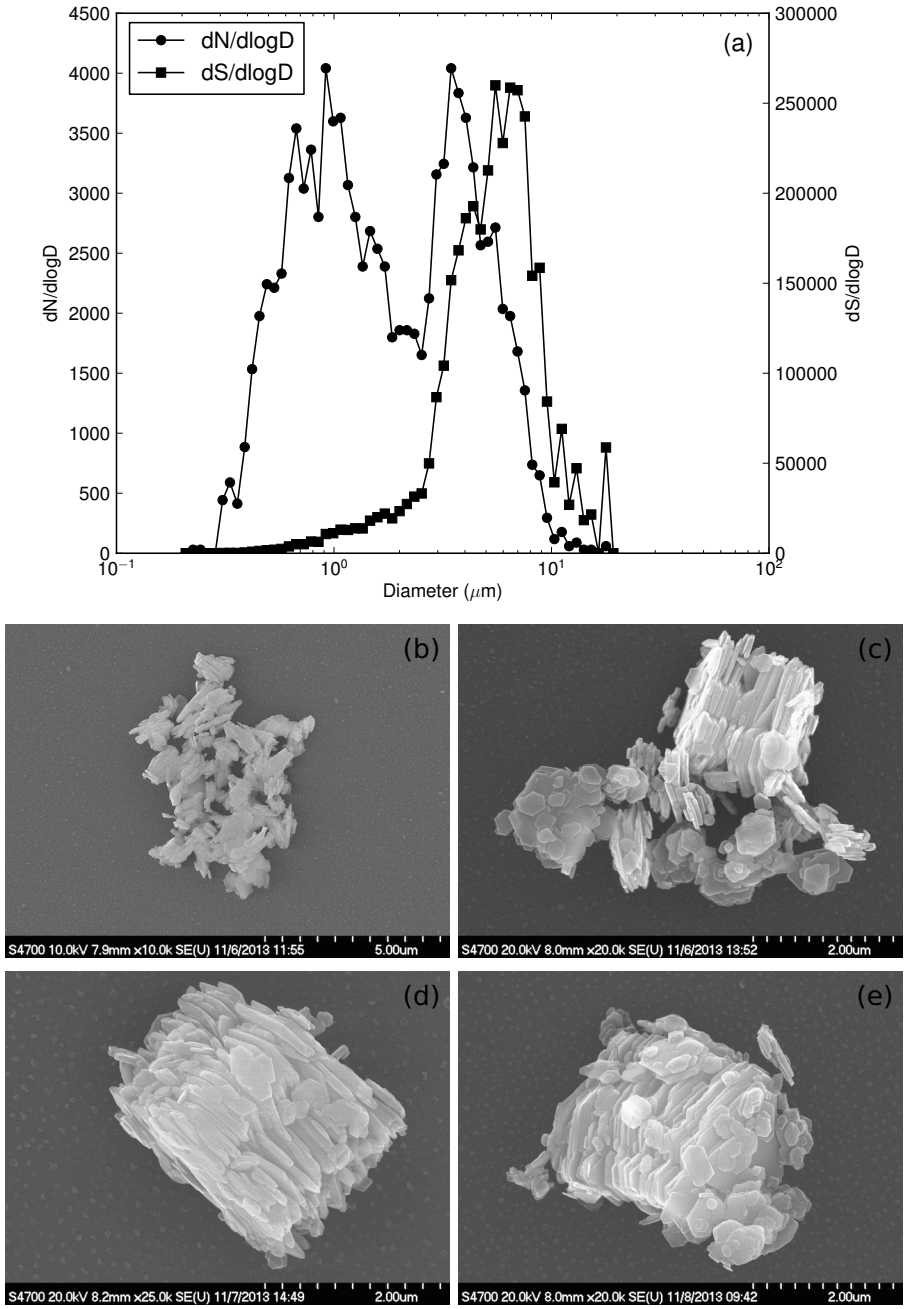

Figure 4.4: (**a**) Size distribution of kaolinite measured by SEM. Shown are the number, N, distribution (closed circles) and the surface area, S, distribution (closed squares) functions. (**b**) - (**e**) SEM images of individual kaolinite particles impacted on the slides.

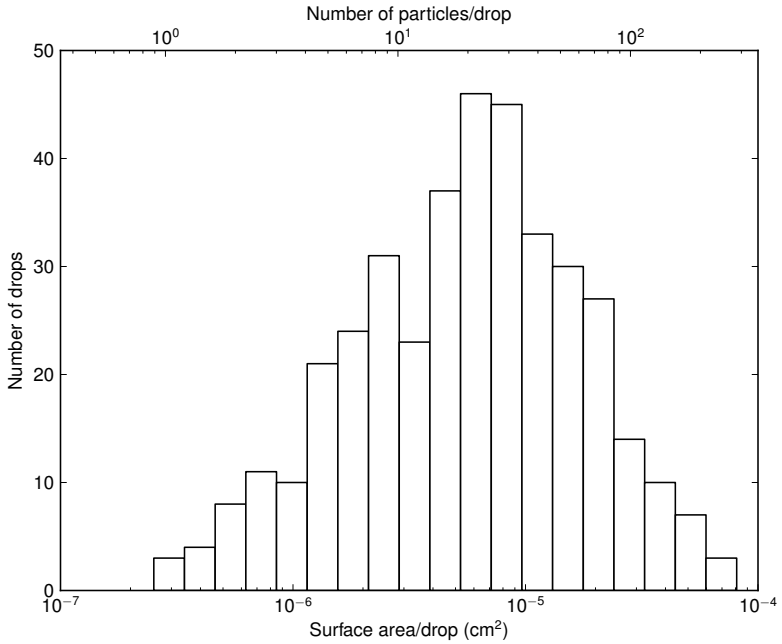

Figure 4.5: Distribution of surface area of mineral dust particles per drop for ATD experiments. The upper abscissa shows the corresponding number of particles contained in each drop based on the average particle size determined from the SEM images ($3\,\mu$m).

bouring frozen drops. Frozen drops can grow by vapour transfer and eventually can come in contact with their neighbouring liquid drops. Alternatively, frozen drops can cause their liquid neighbours to evaporate completely by vapour transfer from liquid drops to frozen drops due to the lower saturation vapour pressure over ice compared with that over supercooled water. In Figs. 4.7 and 4.8 (closed circles), the fraction of drops which froze by immersion freezing are reported. When calculating the fraction frozen, the contact freezing and complete evaporation of supercooled drops was dealt with in two ways. In the first case we assumed that the drops removed by contact freezing and evaporation froze by immersion freezing. This provides an upper limit to the fraction frozen by immersion freezing. In the second case we assumed that the drops which were removed by contact freezing and evaporation remain liquid until the homogeneous freezing temperatures were reached. Since these drops contained mineral dust inclusions and could have frozen at temperatures warmer than homogeneous freezing, this gives a lower limit to the fraction of drops frozen by immersion freezing. Calculations of the

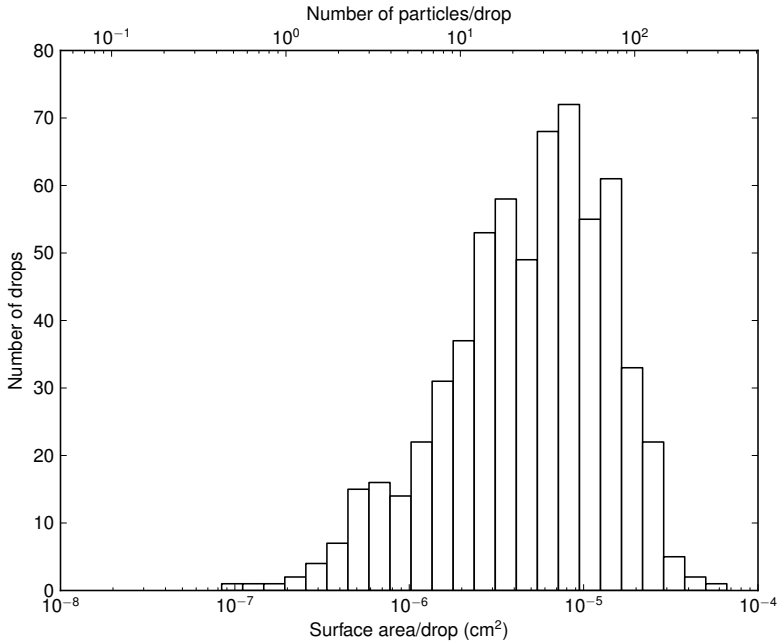

Figure 4.6: Distribution of surface area of mineral dust per drop for kaolinite experiments. The upper abscissa shows the corresponding number of particles contained in each drop based on the average particle size determined from the SEM images ($2.5\,\mu$m).

fraction frozen were done at 0.5 °C intervals down to the onset of homogeneous freezing. The closed circles represent the median between the upper and lower limits at each temperature.

As can be seen from Figs. 4.7 and 4.8, ATD in our experiments induces immersion freezing at warmer temperatures than kaolinite. The median freezing temperature of drops containing ATD was measured to be approximately $-30\,^{\circ}$C compared with approximately $-36\,^{\circ}$C for kaolinite. The ATD containing drops were all observed to be frozen at temperatures warmer than homogeneous freezing. Kaolinite containing drops on the other hand were not all frozen upon reaching temperatures where homogeneous freezing occurred.

The results presented here are the first size-selected freezing studies to focus on supermicron dust particles. The median freezing temperatures for the supermicron dust fall within the range of median freezing temperatures measured previously for submicron dust particles of the same composition [Hoffer, 1961; Hoyle et al., 2011; Lüönd et al., 2010; Murray et al., 2011; Niedermeier et al., 2010, 2011a; Pitter and Pruppacher, 1973; Welti et al., 2012]. However,

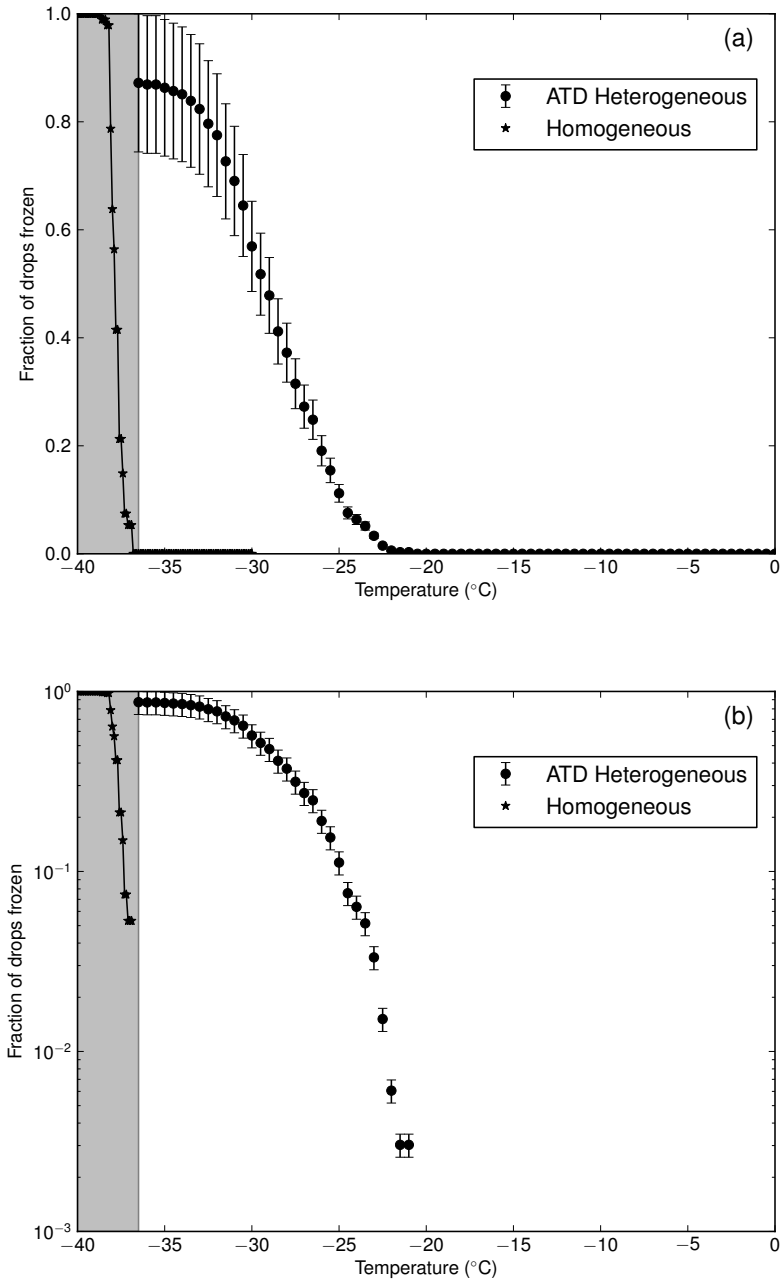

Figure 4.7: Fraction of drops frozen by homogeneous freezing and immersion freezing of drops containing ATD. Data are shown on both a linear (panel a) and log scale (panel b). Stars represent homogeneous freezing results. The closed circles represent the median frozen fraction between the upper and lower limits as described in the text. The uncertainty in the temperature values is $\sim 0.06\,^{\circ}$C. The shaded region represents the area where homogeneous freezing interferes with the heterogeneous freezing results. Heterogeneous data are only shown at temperatures warmer than this region.

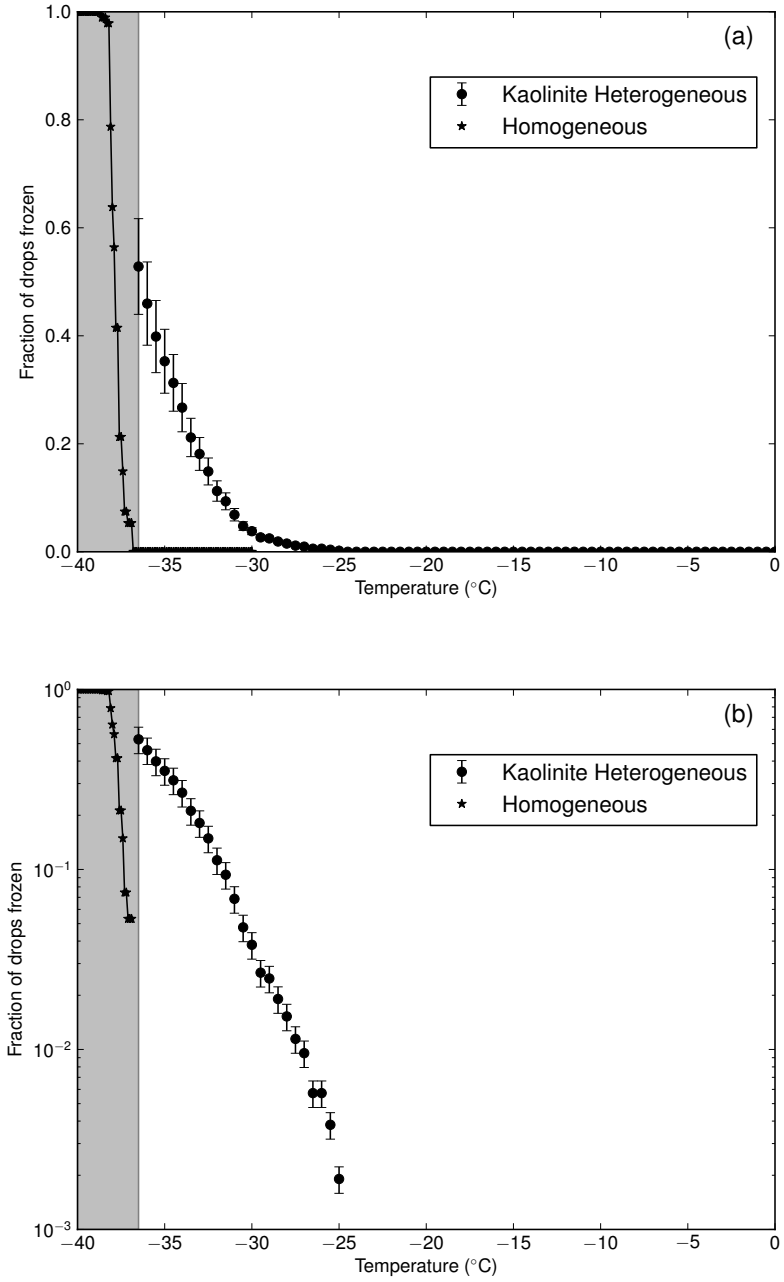

Figure 4.8: Fraction of drops frozen by homogeneous freezing and immersion freezing of drops containing kaolinite. Data are shown on both a linear (panel a) and log scale (panel b). Stars represent homogeneous freezing results. The closed circles represent the median frozen fraction between the upper and lower limits as described in the text. The uncertainty in the temperature values is $\sim 0.06\,^{\circ}$C. The shaded region represents the area where homogeneous freezing interferes with the heterogeneous freezing results. Heterogeneous data are only shown at temperatures warmer than this region.

the median freezing temperature is not the best method for inter-comparison of heterogeneous freezing results since median freezing temperature can depend on the amount of mineral dust in each drop. A more useful metric for inter-comparison of the freezing studies is the ice nucleation active site (INAS) density, which takes into account the surface area of solid material in each drop. A detailed examination of the INAS densities and comparison with other measurements is presented below.

4.3.3 Testing ice nucleation schemes for use in atmospheric models

The new freezing results presented above were used to test four different schemes previously used to describe ice nucleation in atmospheric models. These schemes are referred to as the single-α, pdf-α, active site, and deterministic schemes. These schemes were described in Chapter 3 for deposition nucleation. Below these four schemes are described for immersion freezing.

4.3.3.1 Single-α scheme

The single-α scheme [Fletcher, 1958; Pruppacher and Klett, 1997] is the simplest of the four schemes used here. This scheme is based on classical nucleation theory. Nucleation is assumed to be a stochastic process and can occur with equal probability anywhere on a particle surface. All particles have equal probability per unit surface area to nucleate ice. A single parameter, the contact angle (α), is used to parameterize the data. This scheme has been used in many atmospheric modelling studies [Eidhammer et al., 2009; Ervens and Feingold, 2012; Hoose et al., 2010a,b; Jensen et al., 1994; Jensen and Toon, 1997; Jensen et al., 1998; Kärcher, 1996, 1998; Kärcher et al., 1998; Khvorostyanov and Curry, 2000, 2004, 2005, 2009; Kulkarni et al., 2012; Liu et al., 2007; Morrison et al., 2005].

As shown in Chapter 2, classical nucleation theory can relate the heterogeneous nucleation rate constant for immersion freezing to the energy barrier for embryo formation on a solid

surface [Pruppacher and Klett, 1997; Zobrist et al., 2007]:

$$j_{\text{het}}(T,\alpha) = \frac{kTn_{\text{ice}}}{h}\exp\left(-\frac{\Delta F_{\text{diff}}(T)}{kT}\right)\exp\left(-\frac{\Delta G_{\text{act}}(T)f_{\text{het}}(\alpha)}{kT}\right) \tag{4.1}$$

where k is the Boltzmann constant, n_{ice} is the number density of water molecules at the ice nucleus-water interface, h is Planck's constant, $\Delta F_{\text{diff}}(T)$ is the diffusion activation energy for transfer of water molecules across the ice nucleus-water interface, $\Delta G_{\text{act}}(T)$ is the activation energy for critical embryo formation and $f_{\text{het}}(\alpha)$ is the contact parameter (given by Eq. (4.2)) which describes the reduction in the Gibbs free energy barrier due to the presence of a heterogeneous nucleus. Parameterizations for n_{ice}, $\Delta G_{\text{act}}(T)$, and $\Delta F_{\text{diff}}(T)$ are given by Zobrist et al. [2007].

As was done in Chapter 3 for deposition nucleation, the contact parameter for a given contact angle, α, is given by

$$f_{\text{het}}(\alpha) = \frac{(2+\cos\alpha)(1-\cos\alpha)^2}{4}. \tag{4.2}$$

This equation assumes that the radius of curvature of the particle is significantly larger than the radius of the critical embryo, a valid assumption for our measurements.

The single-α scheme assumes that classical nucleation theory can describe the nucleation rate of ice embryos on the surface of particles and that every particle has the same contact angle. For an ensemble of drops each containing the same surface area of solid inclusions, the fraction of drops frozen at a temperature T can be related to the heterogeneous nucleation rate constant predicted with the single-α scheme by

$$f_d(T) = 1 - \exp\left(-A\, j_{\text{het}}(T,\alpha)\Delta t\right), \tag{4.3}$$

where f_d is the fraction of drops frozen at some temperature T, A is the surface area available to nucleate in each drop, j_{het} is the heterogeneous nucleation rate constant in ($\text{cm}^{-2}\,\text{s}^{-1}$) at

temperature T, and Δt is the time step.

Since the experiments presented here do not involve equal surface areas in each drop (see Figs. 4.5 and 4.6), Eq. (4.3) needs to be modified to take the difference in surface area per drop into account. Equation (4.4) shows the fraction of drops frozen according to the single-α scheme when each drop does not contain the same surface area of solid inclusions.

$$f_d(T) = 1 - \sum_{i=1}^{n_d} \exp\left[-A_i j_{\text{het}}(T,\alpha)\Delta t\right] P(A_i) \tag{4.4}$$

where n_d is the number of drops with unique surface areas observed in the experiments, A_i is the surface area (in cm^2) contained in drop i, $j_{\text{het}}(T,\alpha)$ is the heterogeneous nucleation rate constant (in $\text{cm}^{-2}\,\text{s}^{-1}$) at temperature T, Δt is the time step, and $P(A_i)$ is the probability of a drop containing surface area A_i. For all calculations, the time step Δt is taken as 3 s. This represents the time between successive 0.5°C intervals when using a cooling rate of -10°C/min.

4.3.3.2 Pdf-α scheme

The pdf-α scheme [Lüönd et al., 2010; Marcolli et al., 2007] is a modification of the single-α scheme presented above allowing for a distribution of freezing probabilities among the individual dust particles. In this scheme, each particle nucleates stochastically as in the single-α scheme according to classical nucleation theory with a nucleation rate constant given by Eq. (4.1). The nucleation probability per unit surface area differs, however, from particle to particle. This scheme has been used previously to describe freezing data [Lüönd et al., 2010; Marcolli et al., 2007; Welti et al., 2012; Wheeler and Bertram, 2012] and in model comparison studies [Ervens and Feingold, 2012; Kulkarni et al., 2012].

To describe the nucleation probability of all particles, a distribution of contact angles is assumed for an ensemble of particles. Here, we test a normal distribution of contact angles described by

$$p(\alpha) = \frac{1}{\sigma_\alpha \sqrt{2\pi}} \exp\left[-\frac{(\alpha - \mu_\alpha)^2}{2\sigma_\alpha^2}\right], \tag{4.5}$$

where μ_α and σ_α^2 describe the mean and variance of the normal distribution, respectively. This

gives two parameters to describe the nucleation ability of both the ATD and kaolinite particles.

For an ensemble of drops each containing a single solid inclusion of the same size, the fraction of drops frozen at temperature T described by the pdf-α scheme is given by

$$f_d(T) = 1 - \int_0^{\pi} \exp\left[-A j_{\text{het}}(T,\alpha)\Delta t\right] p(\alpha) d\alpha, \tag{4.6}$$

where f_d is the fraction of drops frozen at temperature T, $p(\alpha)d\alpha$ is the probability of having a contact angle in the range $[\alpha, \alpha + d\alpha]$, A is the surface area of the immersed particle, j_{het} is the heterogeneous nucleation rate constant given by Eq. (4.1), and Δt is the time step.

Since the experiments presented here do not involve only a single solid particle per drop (see Figs. 4.5 and 4.6), Eq. (4.6) above needs to be modified to take into account the possibility of more than one solid inclusion per drop. The fraction of drops frozen according to the pdf-α scheme when each drop does not contain the same number of solid inclusions is given by

$$f_d(T) = 1 - \sum_{n=1}^{n_{\max}} \left\{ \int_0^{\pi} \exp\left[-A_{\text{avg}} j_{\text{het}}(T,\alpha)\Delta t\right] p(\alpha) d\alpha \right\}^n P(n), \tag{4.7}$$

where A_{avg} is the surface area of an average particle immersed in the drop, n is the number of particles per drop, $P(n)$ is the probability of having n particles per drop, and $n_{\max}$ is the maximum number of particles per drop observed in the experiment. The exponent in Eq. (4.7) is included since the probability of a drop containing n solid inclusions of area A_{avg} remaining liquid at temperature T will be the product of the probability of each individual particle not nucleating at temperature T. Numerical integration of Eq. (4.7) was performed using rectangular integration.

4.3.3.3 Active site scheme

As a further extension of the single-α scheme, the active site scheme [Fletcher, 1969; Lüönd et al., 2010; Niedermeier et al., 2011b], assumes that there are certain regions (i.e. active sites) of the particle surface that have a greater probability to nucleate ice. Each active site

nucleates stochastically according to classical nucleation theory as in the single-α and pdf-α schemes, but nucleation is assumed to occur only on these small active sites. Each particle has a particular distribution of active sites determined by the density of active sites ($\rho(\alpha)$). The scheme used here is the same as described by Lüönd et al. [2010] and Welti et al. [2012].

According to the active site scheme, the probability that a single drop containing a single solid inclusion will freeze is given by the following equation, which takes into account that a solid particle can have multiple active sites and that the contact angle can vary from site to site:

$$P_{\text{freeze}}(T) = 1 - \prod_{i=1}^{m} \exp\left[-j_{\text{het}}(T, \alpha_i) A_{\alpha_i} \Delta t\right] \tag{4.8}$$

where A_{α_i} is the total area of active sites with contact angle in the range of α_i to $\alpha_i + \Delta\alpha$, $\Delta\alpha$ is the width of an individual bin such that the total number of bins is equal to m. The area of a single active site is fixed at 6 nm^2 [Lüönd et al., 2010] and A_{α_i} represents an integer multiple of the area of a single site ($A_{\alpha_i} = n_i A_{\text{single}}$ where $A_{\text{single}} = 6\,\text{nm}^2$).

The average number of active sites contained in a drop in each contact angle interval $(\alpha_i, \alpha_i + \Delta\alpha)$ is given by

$$\bar{n}_i = A\rho(\alpha_i)\Delta\alpha, \tag{4.9}$$

where A is the surface area of the solid inclusion immersed in the drop, $\rho(\alpha_i)$ is the density of active sites in the interval $(\alpha_i, \alpha_i + \Delta\alpha)$ given by Eq. (4.10).

$$\rho(\alpha) = b \exp\left(\frac{-\beta_1}{\alpha - \beta_2}\right) \tag{4.10}$$

The number of active sites with contact angles in range $(\alpha_i, \alpha_i + \Delta\alpha)$ can be assigned using Poisson distributed random variables with the expectation value given by Eq. (4.9). To account for multiple particles per drop, the total surface area immersed in the drop was used in place of the surface area of the individual particle in Eq. (4.9).

The freezing probabilities, $P_{\text{freeze}}(T)$, of 1000 drops were calculated using Eq. (4.8). Since there is a distribution of surface areas per drop (see Figs. 4.5 and 4.6), surface areas were

randomly assigned to each drop based on the surface area distributions shown in Figs. 4.5 and 4.6. The fraction of drops frozen was then calculated as:

$$f_d(T) = \frac{N_f(T)}{N_0} = 1 - \frac{N_u(T)}{N_0} = \frac{1}{N_0} \sum_{k=1}^{N_0} P_{\text{freeze,k}}(T), \tag{4.11}$$

where N_u and N_f are the number of unfrozen and frozen drops, respectively, N_0 is the total number of drops (i.e. 1000), and $P_{\text{freeze,k}}$ is the probability that drop k will freeze.

To account for the statistical variability associated with using a limited number of randomly assigned contact angles and areas, averages of 10 individual runs of 1000 drops were used.

4.3.3.4 Deterministic scheme

Unlike the single-α, pdf-α and active site schemes presented above, the deterministic scheme [Connolly et al., 2009] is not derived from classical nucleation theory. Nucleation in the immersion mode according to the deterministic scheme is assumed to be independent of time and depends only on the temperature. This scheme has been used previously to parameterize immersion freezing data [Connolly et al., 2009; Lüönd et al., 2010; Murray et al., 2011; Niedermeier et al., 2010; Welti et al., 2012] and in model comparison studies [Eidhammer et al., 2009; Ervens and Feingold, 2012; Kulkarni et al., 2012].

The fraction of frozen drops for the deterministic scheme is given by

$$f_d(T) = 1 - \sum_{i=1}^{n_d} \exp\left[-A_i n_s(T)\right] P(A_i), \tag{4.12}$$

where n_d is the number of drops with unique surface areas observed in the experiments, $n_s(T)$ is the surface density of active sites at a temperature T given by Eq. (4.13) [Connolly et al., 2009; Lüönd et al., 2010; Welti et al., 2012], and $P(A_i)$ is the probability of a drop containing surface area A_i. The density of active sites, $n_s(T)$, is described using two parameters, A_1 and A_2, which are used to fit the experimental data.

$$n_s(T) = \begin{cases} A_1(T + A_2)^2, & T < -A_2 \\ 0, & T \geq -A_2 \end{cases} \tag{4.13}$$

4.3.3.5 Results from testing different schemes

The experimental freezing data for ATD and kaolinite were fit to the schemes presented above by reducing the weighted sum of squared residuals (WSSR) between the median frozen fractions (as shown in Figs. 4.7 and 4.8) and the predictions. Owing to the greater uncertainty in the frozen fraction at colder temperatures, a weighting function was used to fit the data. The weighting function used is given by [Wolberg, 2006]

$$W_i = \frac{1}{\sigma_i^2}, \tag{4.14}$$

where σ_i is half the distance between the upper and lower limits of the frozen fraction presented in Figs. 4.7 and 4.8. To avoid interferences with homogeneous freezing, only those freezing events which occurred at temperatures warmer than homogeneous freezing were used to fit each scheme. This cut-off temperature was taken as the warmest observed freezing temperature for the homogeneous data shown in Figs. 4.7 and 4.8 (i.e. T = -36.9°C).

The results from fitting the freezing data to the different schemes are shown in Figs. 4.9 and 4.10 for ATD and kaolinite respectively. Tables 4.1 and 4.2 show the best fit parameters, the WSSR and reduced chi-squared values (χ^2_{red}). The value of χ^2_{red} gives a means of comparing the goodness of fit of different schemes with different numbers of fitting parameters. A value close to unity indicates a good fit to the data.

As can be seen in Figs. 4.9 and 4.10 and Tables 4.1 and 4.2, the single-α scheme is unable to represent the freezing of either ATD or kaolinite particles. The scheme prediction is too steep to represent the experimental data, and the χ^2_{red} values are much greater than unity. Given that kaolinite is a single-component mineral, the single-α scheme assumes that the nucleation

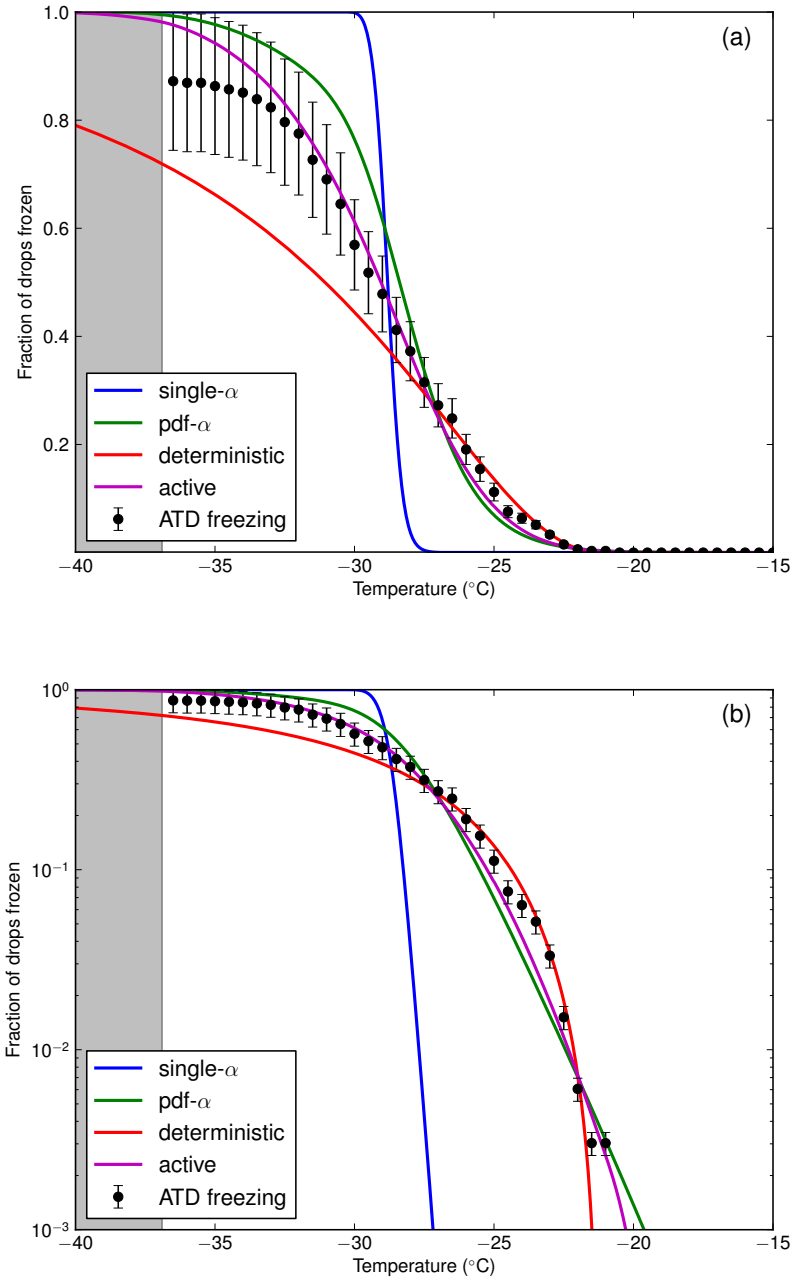

Figure 4.9: Comparison between heterogeneous freezing of drops containing ATD and the different schemes used to describe heterogeneous ice nucleation. Data are shown on both a linear (panel a) and a log scale (panel b). The error in the data points represents the difference between the upper and lower limits to the frozen fraction as described in the text. The uncertainty in the temperature values is $\sim 0.06\,^{\circ}$C. The shaded region shows the area where homogeneous freezing was observed.

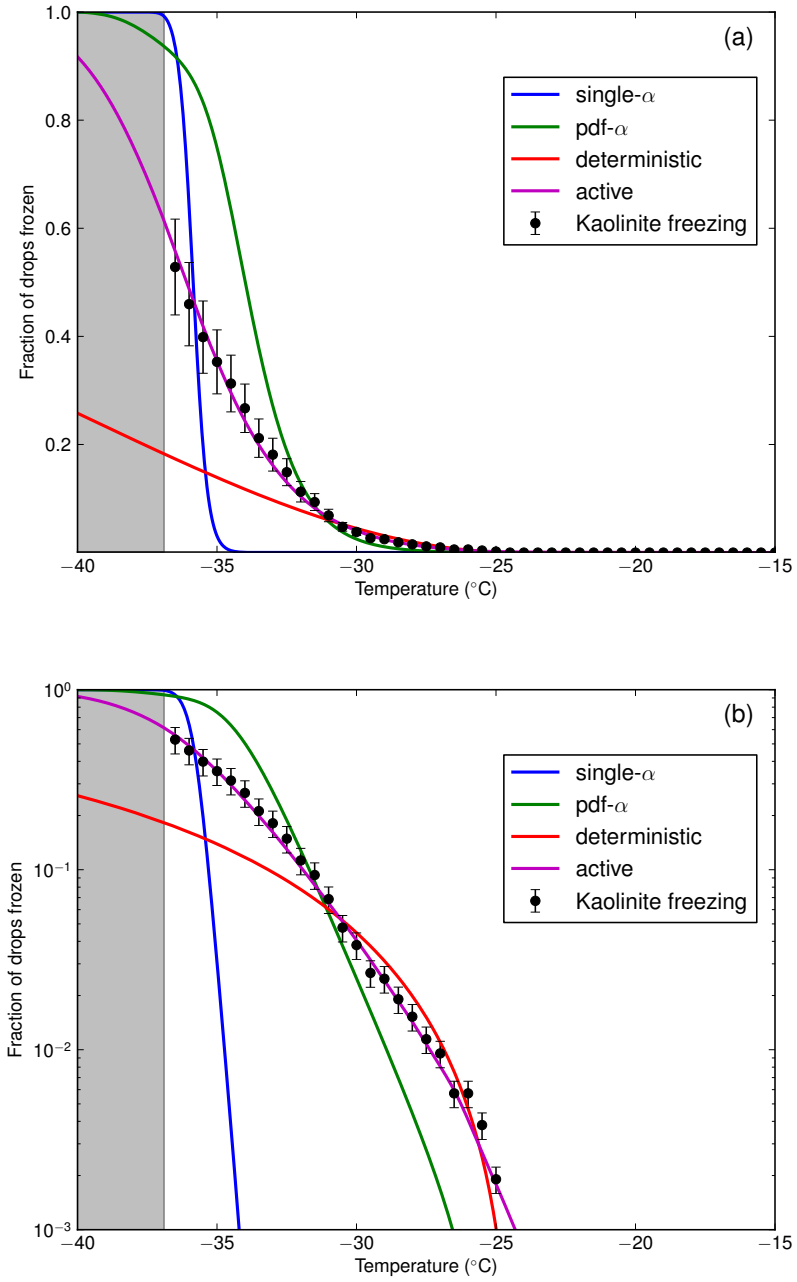

Figure 4.10: Comparison between heterogeneous freezing of drops containing kaolinite and the different schemes used to describe heterogeneous ice nucleation. Data are shown on both a linear (panel a) and a log scale (panel b). The error in the data points represents the difference between the upper and lower limits to the frozen fraction as described in the text. The uncertainty in the temperature values is $\sim 0.06\,^{\circ}\mathrm{C}$. The shaded region shows the area where homogeneous freezing was observed.

Table 4.1: Results from fitting the ATD freezing data to the different schemes. Fitting parameters for the best fit are given along with the weighted sum of squared residuals (WSSR) and reduced chi-squared values (χ^2_{red}).

Scheme	Parameters	WSSR	χ^2_{red}
single-α	$\alpha = 79.5°$	810.5	26.14
pdf-α	$\mu_\alpha = 101.9°$ $\sigma_\alpha = 10.5°$	119.9	3.998
deterministic	$A_1 = 1117.7\,\text{cm}^{-2}$ $A_2 = 21.04\,°\text{C}$	131.6	4.385
active site	$b = 6 \times 10^8\,\text{cm}^{-2}$ $\beta_1 = 3.14$ $\beta_2 = 0.613$	20.7	0.646

Table 4.2: Results from fitting the kaolinite freezing data to the different schemes. Fitting parameters for the best fit are given along with the weighted sum of squared residuals (WSSR) and reduced chi-squared values (χ^2_{red}).

Scheme	Parameters	WSSR	χ^2_{red}
single-α	$\alpha = 108.3°$	775.3	33.71
pdf-α	$\mu_\alpha = 130.2°$ $\sigma_\alpha = 13.7°$	465.4	21.15
deterministic	$A_1 = 177.9\,\text{cm}^{-2}$ $A_2 = 23.98\,°\text{C}$	148.0	6.729
active site	$b = 2 \times 10^{11}\,\text{cm}^{-2}$ $\beta_1 = 16.52$ $\beta_2 = 0.055$	5.8	0.243

probability per unit area is equal for all particles. The results presented here suggest that the assumption of equal nucleation probability is incorrect. The large χ^2_{red} gives further support that a simple stochastic approach is not sufficient to describe ice nucleation on most mineral dusts, consistent with recent conclusions in the literature [Broadley et al., 2012; Lüönd et al., 2010; Marcolli et al., 2007; Vali, 2008, 2014; Welti et al., 2012; Wheeler and Bertram, 2012].

The pdf-α and deterministic schemes are better at describing the freezing data than the single-α scheme but both the pdf-α and deterministic schemes give χ^2_{red} values significantly above 1 for both minerals, suggesting they do not give optimal fits; the deviation between the

fits and the experiments is greater than the uncertainty in the measurements. In contrast, the active site model is able to describe well the freezing of ATD and kaolinite particles as shown with χ^2_{red} values close to one. χ^2_{red} values less than one indicate an overestimation of the error used in the weighting function (Eq. (4.14)).

In terms of ability to fit the ATD data (quantified with χ^2_{red} values), the following trend is observed (from best to worst): active site, pdf-α, deterministic, single-α. For kaolinite, the following trend is observed (from best to worst): active site, deterministic, pdf-α, single-α. Our data suggests that the active site scheme is the most accurate for describing the freezing of the ATD and kaolinite particles tested here. If this scheme cannot be used due to computational expense, then the pdf-α or deterministic scheme should be used, not the single-α scheme.

The changes in median freezing temperatures predicted by each of the stochastic schemes per decade change in the cooling rate is presented in Table 4.3. This was determined by calculating the difference in the median freezing temperature predicted by the different schemes when using the fit parameters to the experimental data (Tables 4.1 and 4.2) and a cooling rate of $10\,^{\circ}\text{C}\,\text{min}^{-1}$ and $1\,^{\circ}\text{C}\,\text{min}^{-1}$. Table 4.3 shows that the active site scheme gave the largest change in median freezing temperature with a decade change in cooling rate. The deterministic scheme (by definition) does not depend on the cooling rate and so no change in median freezing temperature is expected from this scheme.

Also shown in Table 4.3 are changes in the median freezing temperatures with a decade change in cooling rate based on experimental results presented in the literature. The values of Wright et al. [2013] are based on a logarithmic fit to the median freezing temperatures measured at multiple cooling rates. Samples used by Wright et al. [2013] contained a mixture of submicron and supermicron particles, and the kaolinite sample used by Wright et al. [2013] was from a different source than the kaolinite used in this study. A combination of experimental results and fitting to the experimental data by Murray et al. [2011] suggests a variation in the median freezing temperature of approximately $-2\,^{\circ}\text{C}$ per decade change in cooling rate for kaolinite particles. Samples used by Murray et al. [2011] contained a mixture of submicron

Table 4.3: Variation of median freezing temperature with changing cooling rate for both ATD and kaolinite. The prediction for each scheme was calculated by determining the change in median freezing temperature as the cooling rate was changed from $\mathbf{10}\,^{\circ}\mathrm{C\,min^{-1}}$ to $\mathbf{1}\,^{\circ}\mathrm{C\,min^{-1}}$. Variations previously determined in the literature are given for both ATD and kaolinite.

Scheme or Study	Predicted/measured change in median freezing per decade change in cooling rate for ATD (°C)	Predicted/measured change in median freezing per decade change in cooling rate for kaolinite (°C)
single-α	-0.57	-0.58
pdf-α	-0.60	-0.62
deterministic	0	0
active site	-1.0	-1.1
Wright et al. [2013]	-0.5	-1.3
Murray et al. [2011]	not measured	-2

and supermicron particles and the kaolinite sample used by Murray et al. [2011] was from the same source as that used here.

A few conclusions can be made from Table 4.3. First, the experimental studies suggest that the median freezing temperature depends on cooling rate, although the dependence is weak. This is in contrast to the deterministic model, which predicts the median freezing temperature is independent of cooling rate. Second, the single-α, pdf-α, and active site schemes all agree with the experimental results within roughly a factor of two. To further differentiate between the different schemes using the experimental results shown in Table 4.3, an uncertainty analysis of the experimental and modelling results is required.

4.3.3.6 Comparison of fitting results with other studies

The trend from best to worst for ATD and kaolinite in terms of ability to fit the data in our studies (quantified with χ^2_{red} values) is summarized in Table 4.4. For comparison, we have also summarized results from other studies that have compared different schemes, again ranking the schemes from best to worst in terms of their ability to fit experimental data. The active site scheme ranked first or tied for first in five out of the six studies where it was implemented. The pdf-α model ranked first or tied for first in four out of the seven studies where it was

implemented while the deterministic model ranked first or tied for first in three out of the eight studies where it was implemented. The single-α scheme ranked first or tied for first in only two out of the nine studies where it was tested. Studies by Murray et al. [2011] and Niedermeier et al. [2010] both indicate that the single-α scheme provides the best fit to the data or is tied for best fit, however these studies did not test the pdf-α or active site schemes. In addition, the single-α model was ranked last in seven out of the nine studies where it was implemented. The summary in Table 4.4 suggests that the active site scheme is often the most accurate at describing experimental freezing data for mineral dust.

4.3.4 Area sensitivity

As described above, the area determined in these experiments represents the geometric area of the individual particles. SEM images of both kaolinite and ATD (Figs. 4.5b and 4.6b) show that these particles contain additional structure not captured in the area measurements. For this reason, the areas presented in this study represent lower limits to the actual surface area present in each drop. To examine the sensitivity of the fit parameters to the surface area and to determine if the relative rankings of the different schemes was sensitive to the surface area, we performed a sensitivity study by scaling the total surface area in each drop by a factor of 50 [Eastwood et al., 2008; Wheeler and Bertram, 2012]. The resulting fit parameters, WSSR values, and reduced chi-squared values are given in Tables 4.5 and 4.6 for both ATD and kaolinite. Results from the scaled fitting shows that the χ^2_{red} values for each of the four schemes do not vary drastically when the area is scaled by a factor of 50. More important, the relative rankings of the different schemes when the area was scaled by a factor of 50 remain the same. In terms of the parameters from the fits, the parameters derived for the single-α and pdf-α schemes vary by less than 40% when the area was scaled by a factor of 50. On the other hand, the parameters derived for the deterministic scheme and the active site scheme vary by up to a factor of 300 when the area was scaled by a factor of 50.

Table 4.4: Relative ranking of the ability of different schemes to accurately model heterogeneous freezing of mineral dust in both the immersion and deposition mode. Schemes are ranked from 1 to 4 where 1 gives the best fit to the data and 4 the worst. Included are the multi-component stochastic scheme used by Broadley et al. [2012], which is similar to the pdf-α scheme, and the soccer ball scheme of Niedermeier et al. [2011b], which is similar to the active site scheme.

Mineral, mode, size	Study	Scheme			
		single-α	pdf-α	deterministic	active site
kaolinite, deposition, supermicron	Wheeler and Bertram [2012]	4	1	1	1
kaolinite, immersion, supermicron	this study	4	3	2	1
kaolinite, immersion, mixed[1]	Murray et al. [2011]	1	NT[2]	2	NT
kaolinite, immersion, submicron	Lüönd et al. [2010]	4	1	1	1
kaolinite, immersion, submicron	Welti et al. [2012]	4	1	3	2
ATD, immersion, supermicron	this study	4	2	3	1
ATD, immersion, mixed	Marcolli et al. [2007]	4	2	NT	1
ATD, immersion, submicron	Niedermeier et al. [2010]	1	NT	1	NT
illite, immersion, mixed	Broadley et al. [2012]	4	1	2	NT

[1] mixed here refers to a mixture of submicron and supermicron particles used.
[2] NT indicates that this scheme was not tested.

Table 4.5: Results from fitting the scaled surface area ATD freezing data to the different schemes. Fits were obtained by scaling the mineral dust surface area by a factor of 50. Fitting parameters for the best fit are given along with the weighted sum of squared residuals (WSSR) and reduced chi-squared values (χ^2_{red}).

Scheme	Parameters	WSSR	χ^2_{red}
single-α	$\alpha = 82.5°$	819.7	26.44
pdf-α	$\mu_\alpha = 124.3°$ $\sigma_\alpha = 13.6°$	123.9	4.131
deterministic	$A_1 = 22.38\,\text{cm}^{-2}$ $A_2 = 21.04\,°\text{C}$	131.6	4.385
active site	$b = 2 \times 10^6\,\text{cm}^{-2}$ $\beta_1 = 2.11$ $\beta_2 = 0.650$	17.0	0.533

Table 4.6: Results from fitting the scaled surface area kaolinite freezing data to the different schemes. Fits were obtained by scaling the mineral dust surface area by a factor of 50. Fitting parameters for the best fit are given along with the weighted sum of squared residuals (WSSR) and reduced chi-squared values (χ^2_{red}).

Scheme	Parameters	WSSR	χ^2_{red}
single-α	$\alpha = 116.0°$	782.1	34.01
pdf-α	$\mu_\alpha = 134.0°$ $\sigma_\alpha = 8.7°$	741.8	33.72
deterministic	$A_1 = 3.557\,\text{cm}^{-2}$ $A_2 = 23.98\,°\text{C}$	148.0	6.729
active site	$b = 1 \times 10^{10}\,\text{cm}^{-2}$ $\beta_1 = 18.52$ $\beta_2 = 0.006$	6.8	0.284

4.3.5 Supermicron INAS values

The density of ice nucleation active surface sites has been used previously as a means of normalizing data to surface area [DeMott, 1995; Connolly et al., 2009; Hoose and Möhler, 2012; Murray et al., 2012; Niemand et al., 2012]. INAS densities represent the number of ice nucleation sites per unit area (cm^{-2}) of solid inclusion. These values have been used to make conclusions on the importance of different ice nuclei in the atmosphere and to compare results from different laboratories [Hoose and Möhler, 2012; Murray et al., 2012].

We use the method described by Vali [1971] to calculate the value of n_s by first binning

the data according to the surface areas shown in Figs. 4.5 and 4.6. The value of n_s at each temperature is then calculated according to the following formula:

$$n_s(T) = \frac{\sum_{i=1}^{m} -\ln\left(\frac{N_{u,i}(T)}{N_{0,i}}\right) \cdot N_{0,i}}{\sum_{i=1}^{m} N_{0,i} \cdot A_i} \tag{4.15}$$

where the data are divided into m bins, A_i is the surface area per drop contained in bin i, $N_{u,i}(T)$ is the number of unfrozen drops at temperature T in bin i, and $N_{0,i}$ is the total number of drops in bin i. This method has recently been used to determine the INAS densities of other immersion freezing data using the same apparatus [Haga et al., 2013].

Using this method, the INAS densities for ATD and kaolinite were calculated using the upper and lower limits for $N_u(T)$ described above. This provided upper and lower limits for the INAS values. In addition, only bins containing at least 5 data points were included in order to ensure reasonable statistics in each bin.

In Figs. 4.11 and 4.12, the blue shaded areas show the INAS density for ATD and kaolinite based on the measurements presented here. These INAS values do not span the entire range of temperatures shown in Figs. 4.7 and 4.8 due to the binning of the data in Eq. (4.15). Since the numerator in Eq. (4.15) is infinite for values of $N_{u,i} = 0$, values of n_s only exist where values in all bins are not infinite. Also included in Figs. 4.11 and 4.12 for comparison are other experimental data presented in Hoose and Möhler [2012] along with data from Hader et al. [2014]. The data from the literature presented in Figs. 4.11 and 4.12 include measurements of immersion freezing as well as condensation freezing. The data shown in Figs. 4.11 and 4.12 have been grouped based on the size range of particles used in the studies, with red symbols representing studies that used submicron particles, blue symbols representing studies that used supermicron particles, and magenta symbols representing studies that used a mixture of submicron and supermicron particles.

Although there is substantial scatter in each group, Figs. 4.11 and 4.12 suggest that over the range of -26 to $-20\,^{\circ}$C for ATD and -35 and $-25\,^{\circ}$C for kaolinite, the INAS density of

supermicron particles studied here is lower than that of submicron particles shown in Figs. 4.11 and 4.12 (*cf.* red points in Figs. 4.11 and 4.12 with experimental results shown as blue regions). One possible explanation for the difference in INAS densities between submicron and supermicron particles is that the mechanical action of breaking up a mineral into smaller sizes results in the formation of more ice nucleation sites per unit surface area. This finding is consistent with recent experiments by Hiranuma et al. [2014]. These authors showed that the creation of surface irregularities by milling cubic hematite particles can result in an increase in the INAS density of an order of magnitude.

Another possible explanation for the difference in INAS densities between submicron and supermicron ATD particles is that the particle composition depends on particle size. It is conceivable that in the case of a multi-component mineral such as ATD, size selecting particles may result in preferential selection of a particular mineral from the mixture. This may be responsible, at least partially, for the size dependent freezing results shown in Fig. 4.11.

Some of the differences between the supermicron results and the submicron results shown in Figs. 4.11 and 4.12 may also be related to the instrumentation used to determine INAS densities. The majority of the submicron studies were carried out using a continuous flow diffusion chamber, which employed a different method of determining surface area, and a different method of detecting ice nucleation than that employed in the present study. Additionally, different mineral sources may be partially responsible for the differences seen in Figs. 4.11 and 4.12. In the case of kaolinite, Murray et al. [2011] and Zimmermann et al. [2008] used the same source of kaolinite as in our experiments (i.e. CMS KGa-1b); Lüönd et al. [2010] and Welti et al. [2009] used kaolinite obtained from Fluka; Friedman et al. [2011] and Roberts and Hallett [1968] did not indicate the source of the kaolinite used in their study; and Pinti et al. [2012] used multiple sources of kaolinite including the KGa-1b used in this study. In the case of ATD, Niedermeier et al. [2010] and Sullivan et al. [2010] both used the same type of ATD as used in this study (i.e. ATD Ultrafine A1). Knopf and Koop [2006], Marcolli et al. [2007] and Niemand et al. [2012] use other ultrafine samples of ATD. The source of ATD used in the

other studies was not indicated.

Figs. 4.11 and 4.12 also show that the INAS results from the supermicron studies (blue symbols) roughly fall within the range of INAS results determined with a mixture of submicron and supermicron particles (magenta symbols). The reasonable agreement between the supermicron and mixed particle results could in part be due to the fact that many of the mixed particle results were carried out with a drop freezing technique similar to the technique employed here.

Some of the mixed particle data (i.e. experiments with submicron and supermicron particles) presented in Figs. 4.11 and 4.12 use gas-adsorption derived surface areas in the determination of INAS densities (Hader et al. [2014]; Marcolli et al. [2007]; Murray et al. [2011]; Pinti et al. [2012]). As pointed out by Hoose and Möhler [2012], the use of gas-adsorption derived surface areas is likely to result in lower INAS values determined compared with the use of geometric surface areas as was done in the present study. Hiranuma et al. [2014] examined the difference in calculating the INAS densities of cubic and milled hematite particles. Their results showed that for cubic and milled hematite particles, the difference in INAS densities determined using gas-adsorption surface areas compared with those determined using geometric surface areas were less than one order of magnitude.

4.4 Conclusions

The ice nucleation ability of supermicron particles of two mineral species, kaolinite and Arizona Test Dust (ATD), was investigated in the immersion freezing mode. Results showed that supermicron ATD nucleates at warmer temperatures than supermicron kaolinite particles in the immersion mode. Kaolinite had a median freezing temperature of $-36\,^{\circ}$C while ATD had a median freezing temperature of $-30\,^{\circ}$C. Both minerals show median nucleation temperatures which are warmer than homogeneous freezing.

The experimental data were fit to four different freezing schemes: the single-α, pdf-α, active site, and deterministic schemes. The one-parameter classical nucleation single-α scheme

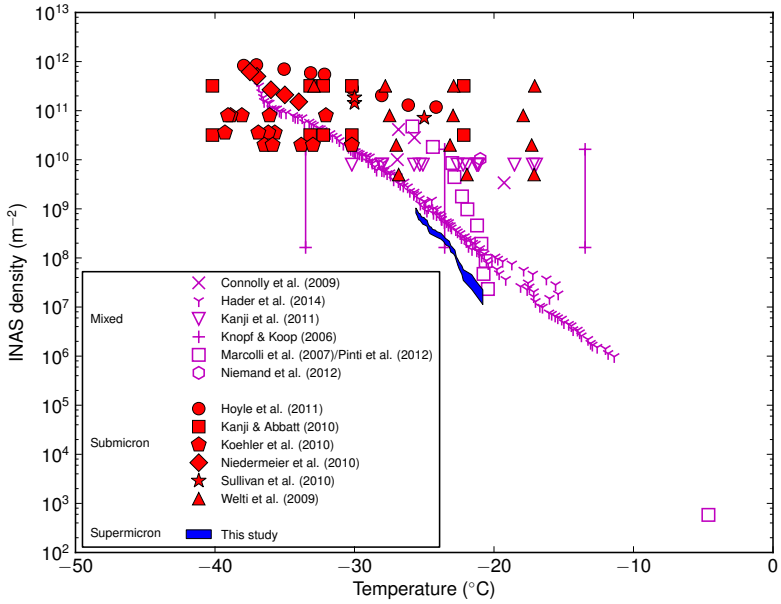

Figure 4.11: Ice nucleation active site (INAS) densities as a function of temperature for ATD. Results from supermicron particles are in blue while submicron data are in red. Experiments performed with a mixture of submicron and supermicron particles are shown in magenta.

is incapable of describing the nucleation of supermicron ATD or kaolinite particles. The active site scheme is the most accurate at reproducing the freezing results of ATD and kaolinite particles and the pdf-α and deterministic schemes fall between the active site scheme and the single-α scheme in terms of ability to fit the freezing results (quantified using the χ^2_{red} values).

The variation in the predicted median freezing temperature per decade change in the cooling rate for each of the schemes was also compared with experimental results from other studies. The deterministic scheme predicts the median freezing temperature to be independent of cooling rate, while the experimental results show a weak dependence on cooling rate. The single-α, pdf-α, and active site schemes all agree with the experimental results within roughly a factor of two.

Based on our results and previous results where different schemes were tested, the active site scheme is recommended for describing the freezing of ATD and kaolinite particles. The current study was carried out using a single cooling rate ($10\,^{\circ}\text{C}\,\text{min}^{-1}$) and over a relatively

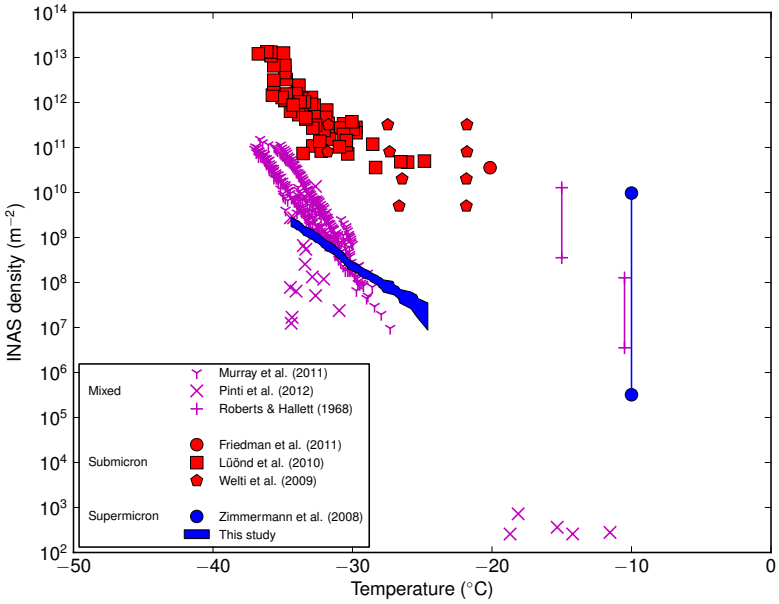

Figure 4.12: Ice nucleation active site (INAS) densities as a function of temperature for kaolinite. Results from supermicron particles are in blue while submicron data are in red. Experiments performed with a mixture of submicron and supermicron particles are shown in magenta.

limited range of temperatures. Additional studies with different cooling rates and different numbers of particles per drop (which would extend the temperature range studied) would be useful to further test the schemes.

INAS densities were calculated from the experimental data and compared with other results presented in Hoose and Möhler [2012] and Hader et al. [2014]. The supermicron particles studied here were observed to have a lower INAS density than submicron particles for both ATD and kaolinite reported in the literature. For kaolinite, the differences may be related to the different sources of kaolinite used in the studies. In the case of ATD, the differences may be due to the mechanical processing of the particles to produce smaller sized particles which may lead to greater surface imperfections in submicron particles compared with supermicron particles. Recent studies with hematite particles are consistent with this finding [Hiranuma et al., 2014].

Maring et al. [2003] has shown that there is a significant fraction of mineral dust parti-

cles that lie in the supermicron range even after transport. This combined with the difference between the freezing abilities of supermicron and submicron particles indicates the need for further study into freezing on supermicron dust particles.

Chapter 5

Testing different schemes for describing immersion freezing of water drops containing primary biological aerosol particles

5.1 Introduction

Ice nucleation in the atmosphere can occur through two distinct processes: homogeneous nucleation and heterogeneous nucleation. Heterogeneous nucleation refers to the formation of the ice phase due to the presence of an insoluble (or partially insoluble) particle referred to as an ice nucleus (IN).

Heterogeneous ice nucleation can influence the extent and lifetime of both ice and mixed-phase clouds [Boucher et al., 2013; DeMott et al., 2010; Lohmann and Feichter, 2005; Lohmann and Diehl, 2006] which in turn can lead to changes in radiative forcing and precipitation. There still remains a large uncertainty in our understanding of the nature of heterogeneous ice nucleation in the atmosphere [Boucher et al., 2013; Murray et al., 2012] and by consequence in the

ability to accurately predict heterogeneous ice nucleation in atmospheric models.

There is now strong evidence that mineral dust particles are an important atmospheric IN. Evidence in favour of this has been presented in laboratory, field and modelling studies [Hoose and Möhler, 2012; Murray et al., 2012]. Another potentially important atmospheric IN is primary biological aerosol particles (PBAPs). PBAPs include fungi, bacteria, pollen, and viruses as well as fragment or excretions from biological organisms [Després et al., 2012]. Although recent atmospheric simulations have shown that PBAPs may not be important on a global annual scale [Burrows et al., 2013; Hoose et al., 2010a,b; Sesartic et al., 2012, 2013] they may still be important both regionally and seasonally. For example, numerous field studies have identified ice nucleation active PBAPs [Bowers et al., 2009; Christner et al., 2008a,b; Constantinidou et al., 1990; Garcia et al., 2012; Huffman et al., 2013; Jayaweera and Flanagan, 1982; Lindemann et al., 1982; Maki and Willoughby, 1978; Morris et al., 2008; Pratt et al., 2009; Prenni et al., 2009, 2013]. In addition, modelling studies suggest that ice nucleation of PBAPs may be important when concentrations of other important IN are low or concentrations of PBAPs are high [Phillips et al., 2008; Hazra, 2013; Gonçalves et al., 2012; Costa et al., 2014; Després et al., 2012]

In order to implement ice nucleation into atmospheric models, an appropriate scheme is necessary in order to accurately describe the freezing behaviour of the IN particles in question. Modelling studies have shown that varying the scheme used to represent ice nucleation in the model can produce significant variation in the predicted cloud properties [Eidhammer et al., 2009; Ervens and Feingold, 2012; Kulkarni et al., 2012; Wang and Liu, 2014; Wang et al., 2014]. For example, Ervens and Feingold [2012] compared five different schemes for describing ice nucleation on kaolinite particles in an adiabatic parcel model. Results showed significant differences in the number of IN predicted depending on the scheme used to describe ice nucleation. These differences were greatest for simulations which employed polydisperse IN compared with monodispersed particles.

Recently, several studies have focused on testing difference schemes for describing labora-

tory freezing of mineral dusts [Broadley et al., 2012; Lüönd et al., 2010; Marcolli et al., 2007; Murray et al., 2011; Niedermeier et al., 2010; Welti et al., 2012; Wheeler and Bertram, 2012; Wheeler et al., 2015b]. Some of the results from this work is summarized in Chapter 4, Section 4.3.3.6. Four schemes were mainly tested: the single-α, pdf-α, active site and deterministic schemes. Three of these schemes are stochastic schemes (single-α, pdf-α, active site) based on CNT. The results of these tests suggest that the active site scheme is most capable of describing ice nucleation on mineral dust particles with the pdf-α scheme performing almost as well followed by the deterministic scheme. In the majority of studies, the single-α scheme was the worst at predicting the ice nucleation behaviour of mineral dust particles. The studies which suggest that the single-α scheme most accurately describes the freezing behaviour did not examine the pdf-α or active site schemes.

There have also been a few studies that have tested different schemes for describing laboratory freezing studies of PBAPs, although the number of these studies is fewer than for mineral dusts. Hartmann et al. [2013] tested the CHESS (stoCHastic modEl of similar and poiSSon distributed ice nuclei) scheme for representing the ice nucleation of *Pseudomonas syringae* and Snowmax^{TM} (an industrial formulation containing non-viable *P. syringae* cells). Augustin et al. [2013] tested the CHESS scheme, single-α scheme and an active site scheme (soccer ball, described below) using the immersion freezing of ice nucleating macromolecules from two samples of Birch pollen. Empirical parameterizations have also been proposed for PBAPs [Tobo et al., 2013; Diehl and Wurzler, 2004; Diehl et al., 2006; Phillips et al., 2008], although these have not been compared with the other schemes described above.

In the following we test four different schemes using the freezing data of bacteria and fungal spores measured by Haga et al. [2013] and Haga et al. [2015]. The schemes tested were the single-α scheme, the pdf-α scheme, the soccer ball scheme and the deterministic scheme. The single-α, pdf-α and deterministic schemes are the same as presented in Chapter 4. The soccer ball scheme is similar to the active site scheme presented in Chapters 3 and 4. Results from the test were used to rank the different schemes in terms of their ability to describe the

freezing data. These relative rankings of the different schemes may be useful when deciding which schemes to use in modelling studies and when considering trade-offs between accuracy and computational efficiency.

5.2 Methods

5.2.1 Immersion freezing data from Haga et al. [2013] and Haga et al. [2015]

The immersion freezing temperatures of six species of fungal spore as well as eight species of bacteria cells were previously examined using a temperature and humidity controlled flow cell [Haga et al., 2013, 2015]. A full description of the experimental technique can be found in the previous references.

The list of fungal spores studied can be found in Table 5.1. They comprise two different classes of fungi. Four rust species were examined: *Puccinia graminis*, *Puccinia triticina*, *Puccinia allii* and *Endocronartium harknessii*. Two species of bunt fungi were also examined: *Tilletia laevis* and *Tilletia tritici*. Both of these classes of fungi represent common plant pathogens.

Table 5.1: Summary of fungal spores used in the immersion freezing experiments of Haga et al. [2013]. The freezing data by Haga et al. [2013] is used here to test different schemes for describing laboratory ice nucleation data. All spores are assumed to be prolate spheroids based on experimental images. Sizes are given as major axis $\times$ minor axis. All dimensions are given in μm.

Type	Species	Spore Size[1]
Rust fungi	*Puccinia graminis* f. sp. *tritici*	20.8×12.5
	Puccinia triticina	21.6×18.0
	Puccinia allii	23.0×17.6
	Endocronartium harknessii	23.8×17.0
Bunt fungi	*Tilletia laevis*	18.2×14.8
	Tilletia tritici	17.9×15.9

[1]Spore size determined from optical images of individual spores.

P. graminis and *P. triticina* spores were obtained from the Cereal Research Centre, Agriculture and Agri-Food Canada, Winnipeg, Manitoba. *P. allii* (sample held at the UBC Herbarium under label AKB 4) was harvested from leek plants in Vancouver, British Columbia, Canada. *E. harknessii* (UBC Herbarium, AKB 5) was obtained from a pine tree in Terrace, British Columbia, Canada. *T. laevis* and *T. tritici* spores were obtained from infected wheat heads acquired from the Lethbridge Research Centre, Agriculture and Agri-Food Canada, Lethbridge, Alberta.

The list of the bacteria species studied are shown in Table 5.2 along with the size of the individual cells. A total of eight species were examined by Haga et al. [2015], however we have limited the analysis here to three species since these were the only species which showed any significant amount of IN activity warmer than homogeneous freezing (*cf.* homogeneous freezing with samples *B. subtillis*, *C. testosteroni*, *M. luteus*, *P. putida*, and *S. albidoflavus* from Haga et al. [2015]).

Table 5.2: Summary of bacteria species used in the immersion freezing experiments by Haga et al. [2015]. The freezing data by Haga et al. [2015] is used here to test different schemes for describing laboratory ice nucleation data. All cells are assumed to be cylinders with size information based on the literature values of Buchanan and Gibbons [1974]. Sizes are given as major axis $\times$ minor axis. All dimensions are given in μm.

Species	Cell Size
Bacillus cereus	4×1.1
Pseudomonas graminis (strain 13b-3)	4.25×0.75
Pseudomonas syringae (strain 31R1)	2.25×0.95

Bacillus cereus was obtained from the Bioservices Laboratory bacterial collection (Department of Chemistry, University of British Columbia, Vancouver, Canada), collection number 1062. *Pseudomonas graminis* (strain 13b-3) was provided by P. Amato (Laboratoire de Synthèse et Étude de Systèmes à Intérêt Biologique, CNRS-Université Blaise Pascal, Aubière, France). *Pseudomonas syringae* (strain 31R1) was provided by S. Lindow (Department of Plant and Microbial Biology, University of California, Berkley, U.S.A.).

All bacteria species were cultured according to the method outline by Möhler et al. [2008b]. Bacteria were deposited on the glass slides by nebulizing a suspension of the cells after culturing. Further details on the sample preparation method can be found in Haga et al. [2015].

Shown in Figs. 5.1 and 5.2 are the freezing data from Haga et al. [2013] and Haga et al. [2015]. Plotted are the fraction of drops frozen as a function of temperature. In these experiments, drops contained one or more fungal spore or bacteria cell inclusion. The distribution of fungal spores or bacteria cells per drop can be found in Figs. B.5 and B.6. Details on how these values were determined can be found in Haga et al. [2013] and Haga et al. [2015]. Also included for comparison purposes in Figs. 5.1 and 5.2 are the homogeneous freezing results from Iannone et al. [2011].

The data shown in Figs. 5.1 and 5.2 have been replotted from what was plotted in Haga et al. [2013] and Haga et al. [2015]. In the original publications, the frozen fraction of drops was presented as a function of temperature with each plotted point representing an individual freezing event. In order to more easily fit the ice nucleation schemes to the experimental data, the fraction frozen presented here has been calculated at 0.5 °C intervals from 0 °C to −40 °C. For measurements taken at a constant cooling rate (as is the case in these studies) this ensures a constant time between subsequent frozen fraction values when fitting the data to the stochastic time dependent schemes.

5.3 Fitting schemes

The single-α scheme, the pdf-α scheme, and the deterministic scheme are the same as presented in Chapter 4. Only the details specific to the implementation to the data described here are discussed along with a more detailed description of the soccer ball scheme.

5.3.1 Single-α scheme

The single-α scheme is described in Chapter 4. As was the case for the data presented in Chapter 4, each drop contains multiple particles. For the experiments performed here, however,

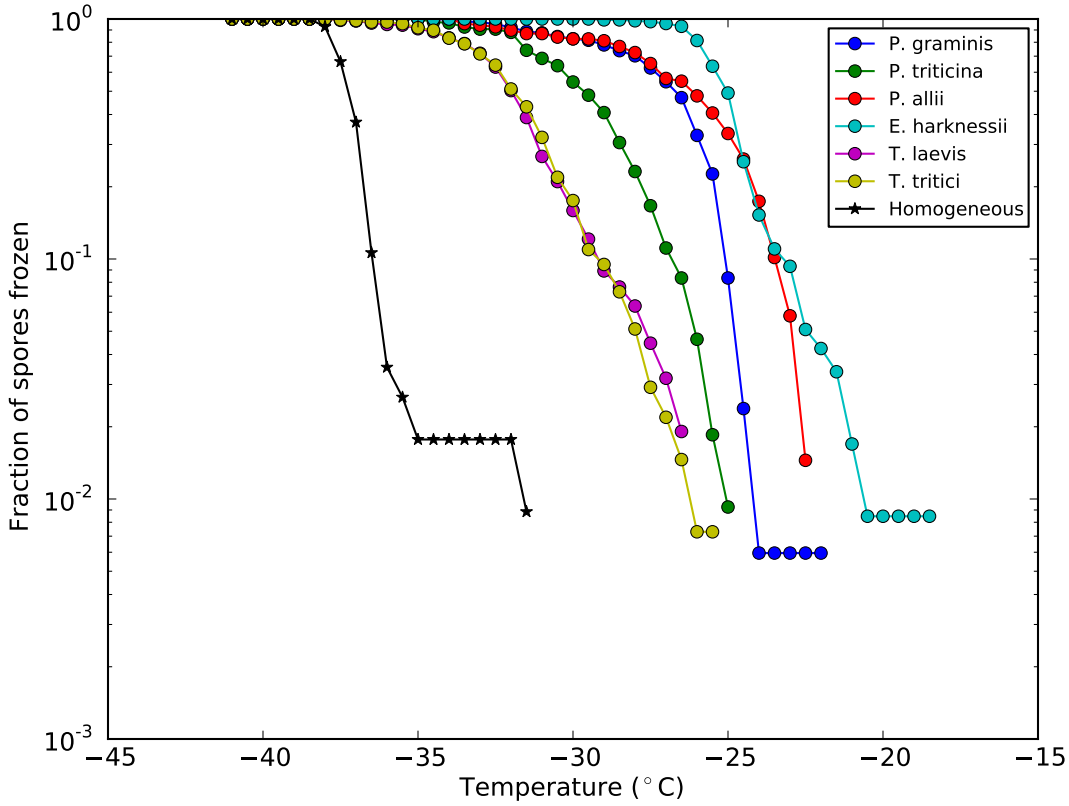

Figure 5.1: Fraction of spore containing drops frozen as a function of temperature calculated from data presented in Haga et al. [2013]. See text for details. Also included are results for drops containing no spores taken from Iannone et al. [2011] and referred to as homogeneous freezing here.

there is only a small variation in size among the particles. Due to this, we assume that each of the particles contained in a drop are all of equal size as shown in Tables 5.1 and 5.2. With this assumption, the resulting fraction of drops frozen as a function of temperature is given by,

$$f_d(T) = 1 - \sum_{n=0}^{n_{\max}} \exp\left[-nA_p j_{\text{het}}(T,\alpha)\Delta t\right] P(n), \tag{5.1}$$

where n is the number of particles contained in a drop, A_p is the surface area of a single particle, $P(n)$ is the fraction of drops containing n particles, and j_{het} is the temperature and contact angle dependent heterogeneous nucleation rate constant given by Eq. (4.1). A time step of 6 s (the time between successive 0.5 °C intervals at a ramp rate of $-5\,^{\circ}\text{C}\,\text{min}^{-1}$) was used for all

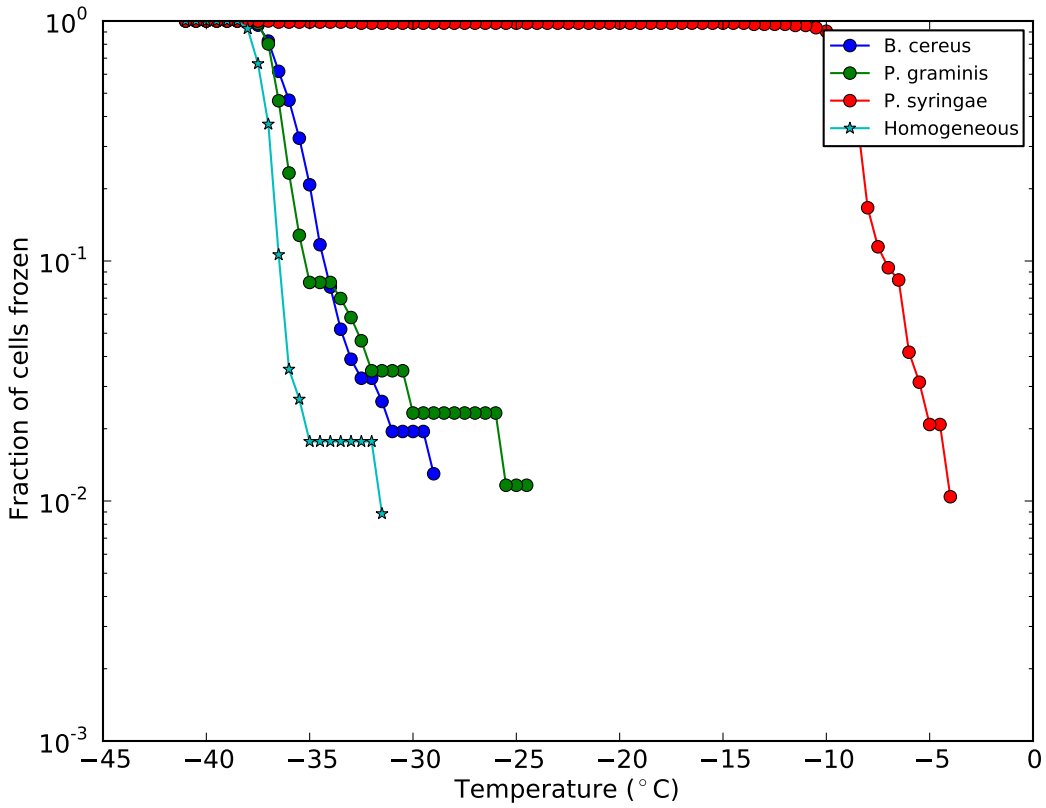

Figure 5.2: Fraction of bacteria containing drops frozen as a function of temperature calculated from data presented in Haga et al. [2015]. See text for details. Also included are results for drops containing no bacteria, taken from Iannone et al. [2011] and referred to as homogeneous freezing here.

samples studied except for the *P. syringae* samples where a ramp rate of $-10\,^{\circ}\mathrm{C\,min^{-1}}$ led to a time step of 3 s.

5.3.2 Soccer ball scheme

Fletcher [1969] was the first to propose a theoretical model to describe the existence of preferential nucleation sites on a particle surface, termed "active sites". These active sites were assumed to be physical deformities on the particle surface having a contact angle of zero. Ensembles of particles could be modelled assuming a size dependent density of active site on the particle surface. This form of the active site model is similar to that used by Lüönd et al. [2010] and Welti et al. [2012].

Niedermeier et al. [2011b] proposed a variation to the active site model described above called the "soccer ball" model. In this model the particle is divided up into a number of equally sized sites and the contact angle is allowed to vary from site to site. Using a Monte Carlo simulation, ensembles of particles were modelled and the freezing probability of the ensemble was determined. More recently, Niedermeier et al. [2014] proposed a modified version of the soccer ball model. This model is less computationally expensive and has been shown to produce the same results as the previous Monte Carlo simulation.

The soccer ball scheme starts by dividing each particle up into a number (n_{site}) of equally sized nucleation sites. The contact angle of each site is assumed to follow a normal distribution with a mean (μ_α) and a standard deviation (σ_α). Each site nucleates according to the single-α scheme described above.

If we consider a situation where each drop contains only a single particle and each particle is composed of a single site ($n_{\text{site}} = 1$), then each particle can be described by a single contact angle and the distribution of these contact angles is given by the normal distribution. The surface area of each site (s_{site}) is equal to the surface area of the particle (A_p). The probability of a single drop being unfrozen at temperature T is given by,

$$\begin{aligned} P_{\text{het unfr}}(T,\mu_\alpha,\sigma_\alpha,t) = &\int_0^\pi p(\alpha)\exp(-j_{\text{het}}(T,\alpha)s_{\text{site}}t)d\alpha \\ &+ \int_{-\infty}^0 p(\alpha)\exp(-j_{\text{het}}(T,\alpha=0)s_{\text{site}}t)d\alpha \\ &+ \int_\pi^\infty p(\alpha)\exp(-j_{\text{het}}(T,\alpha=\pi)s_{\text{site}}t)d\alpha \end{aligned} \tag{5.2}$$

where $p(\alpha)$ is the probability density function of the normal distribution given by Eq. (5.3) and s_{site} is the area of the active site. The three terms in Eq. (5.2) account for the fact that the normal distribution of contact angles (Eq. (5.3)) is a continuous function outside of the interval of contact angles we define $(0,\pi)$. The contact angle is set to 0 for values of the distribution with $\alpha < 0$ while the contact angle is set to π for values of the distribution with $\alpha > \pi$. This ensures that the freezing probability covers the interval [0,1].

$$p(\alpha) = \frac{1}{\sqrt{2\pi}\sigma} \exp\left[-\frac{(\alpha-\mu)^2}{2\sigma^2}\right] \tag{5.3}$$

The frozen fraction of drops is given as the probability that a single drop will freeze heterogeneously. This is given by:

$$f_{\text{ice}}(T, \mu_\alpha, \sigma_\alpha, t) = 1 - P_{\text{het unfr}}(T, \mu_\alpha, \sigma_\alpha, t). \tag{5.4}$$

If we now consider a situation where there are multiple sites on each particle ($n_{\text{site}} > 1$), the area of a single site is $s_{\text{site}} = A_p/n_{\text{site}}$ where A_p is the surface area of a single particle. The probability of a single site remaining unfrozen at temperature T is given by Eq. (5.2). Since the freezing of each site is independent of the other, the probability of all sites on a particle remaining liquid at temperature T is given by:

$$P_{\text{all sites unfrozen}}(T, \mu_\alpha, \sigma_\alpha, t) = \left[P_{\text{het unfr}}(T, \mu_\alpha, \sigma_\alpha, t)\right]^{n_{\text{site}}}. \tag{5.5}$$

Since the measurements presented here do not contain a single particle in each drop, we must consider the probability of each of these individual particles freezing. Similar to the introduction of multiple sites on a single particle above, the introduction of multiple particles per drop results in a product of the freezing probabilities of the individual particles resulting in:

$$P_{\text{all particles unfr}} = \sum_{n=1}^{n_{\max}} \left\{\left[P_{\text{het unfr}}(T, \mu_\alpha, \sigma_\alpha, t)\right]^{n_{\text{site}}}\right\}^n P(n), \tag{5.6}$$

where $P(n)$ is the probability of having n particles per drop.

The fraction of drops frozen is given by

$$f_d(T) = 1 - P_{\text{all particles unfr}}. \tag{5.7}$$

Due to the necessity of performing a numerical integration of Eq. (5.2), the probability

$P_{\text{het unfr}}$ will not equal exactly one even at temperatures close to 0 °C. This will lead to a non zero fraction frozen calculated at 0 °C. For a value of $n_{\text{site}} = 1$ this error remains quite low ($\sim 10^{-15}$), but for higher values of n_{site} in Eq. (5.6), the error is compounded by the power of n_{site}. Thus, for high values of n_{site} the error in frozen fraction calculated with the soccer ball scheme is comparable to the experimental frozen fraction values. For this reason, we have limited the maximum value of n_{site} in these calculations to be 10^8 such that the error in calculated frozen fraction will remain several orders of magnitude below the lowest experimental frozen fraction. Numerical integration was performed using trapezoidal integration.

5.3.3 Pdf-α scheme

This model is the same as the soccer-ball model shown in Eq. (5.7) where the number of sites is set to unity ($n_{\text{site}} = 1$). Here we use the soccer ball scheme in the special case where $n_{\text{site}} = 1$ to evaluate the pdf-α scheme and compare these results with the three parameter soccer ball scheme. This is equivalent to the pdf-α scheme presented in Chapter 4.

5.3.4 Deterministic scheme

The deterministic scheme is the same as was presented in Chapter 4. As described for the single-α scheme, we assume that the size of all particles of a given type is the same for these measurements (i.e. the particles are monodisperse). Based on this assumption, the fraction of drops frozen at temperature T considering a distribution of particles per drop is given by,

$$f_d(T) = 1 - \sum_{n=0}^{n_{\max}} \exp\left[-nA_p n_s(T)\right] \cdot P(n) \tag{5.8}$$

where n is the number of particles contained in each drop, $P(n)$ is the probability of having n particles per drop, and A_p is the surface area of a single particle. The density of sites active at a temperature T, $n_s(T)$, is given by Eq. (4.13).

5.4 Results and discussion

The experimental freezing data (Figs. 5.1 and 5.2) were fit to the different schemes described above by minimizing the weighted sum of squared residuals (WSSR) between the scheme output and the experimental results. WSSR was calculate as

$$\mathrm{WSSR} = \sum_{i=1}^{n} w_i \left(y_i - f_d(T_i, \gamma_1, ..., \gamma_m)\right)^2, \tag{5.9}$$

where w_i is the weighting function employed, y_i is the individual fraction frozen at temperature T_i, and $\gamma_1, ..., \gamma_m$ represents the variable number of fitting parameters (1 for the single-α scheme, 2 for the pdf-α and deterministic schemes, and 3 for the soccer ball scheme). Input to the different schemes included the size of the individual fungal spores or bacteria cells (Tables 5.1 and 5.2) and the number of spores or bacteria cells per drop (Figs. B.5 and B.6).

In order to avoid influence from homogeneous freezing, heterogeneous freezing data at temperatures $\leq -36\,^{\circ}\mathrm{C}$ was not included in the fitting of the four schemes based on the homogeneous freezing data of Iannone et al. [2011]. Iannone et al. [2011] measured homogeneous freezing with the same apparatus used by Haga et al. [2013] and Haga et al. [2015].

Due to the variation in uncertainty as a function of frozen fraction, a weighting function was used in fitting the experimental data. The inverse of the variance at each point was chosen as a weighting function [Wolberg, 2006] which applied greater weighting to points which had a lower level of uncertainty. The weighting function employed is given as

$$w_i = \frac{1}{\sigma^2\left(f_d\right)} \tag{5.10}$$

where $\sigma^2\left(f_d\right)$ represents the variance as a function of frozen fraction. In order to estimate the variance of the measurements, the original freezing data for each species were randomly divided into two equally sized groups. The frozen fraction was calculated independently for the two groups and the difference between the values of the two groups was calculated at each

temperature. An example of this is shown in Fig. 5.3 for the *P. allii* dataset. The blue and green traces show the frozen fractions each calculated from half of the complete dataset. The red trace represents the midpoint between the green and blue traces. The standard deviation at each temperature was calculated as half the difference between the blue and the green traces. An average standard deviation at each temperature was obtained by repeating the above process 100 times for each species. This process was repeated for each of the nine species and the resulting average standard deviations as a function of frozen fraction is shown in Fig. 5.4. A best fit to the data presented in Fig. 5.4 was used to calculate the variance in Eq. (5.9).

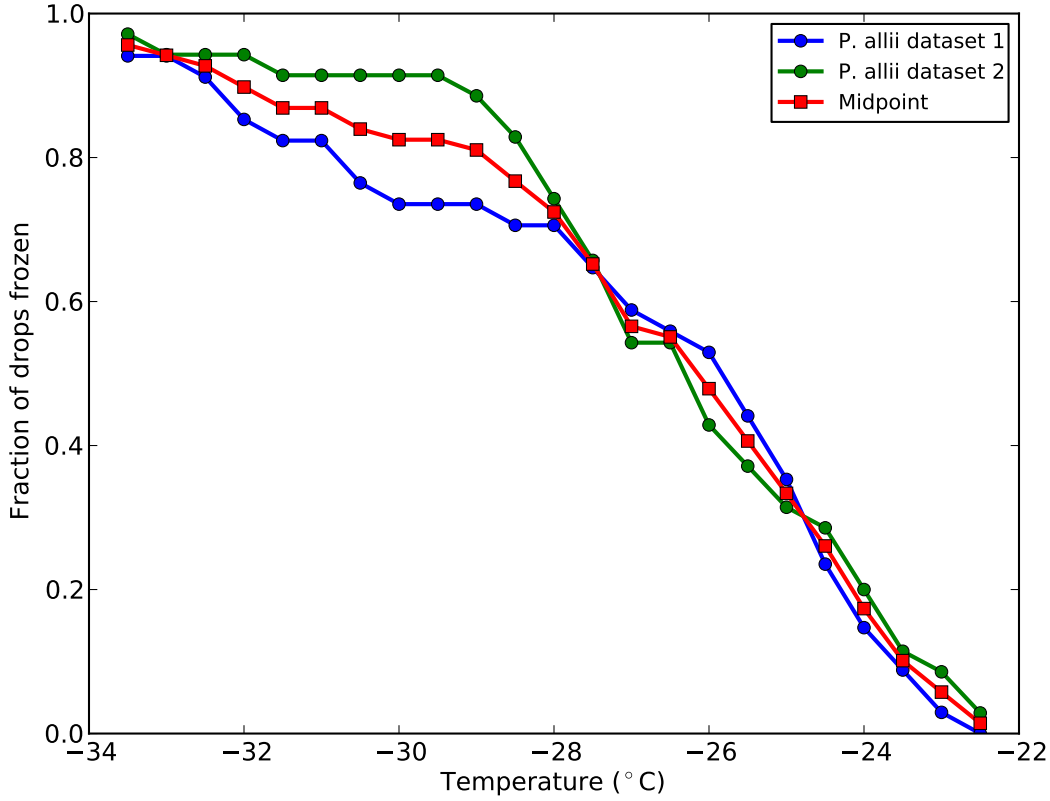

Figure 5.3: Estimation of the relative standard deviation (σ_{rel}) of *P. allii*. A description of the method used to evaluate σ_{rel} is given in the text.

The standard deviations determined using the method described above should be considered conservative estimates of the actual standard deviation since they were determined by splitting each of the datasets in half. Since the freezing data used in the measurements analyzed here

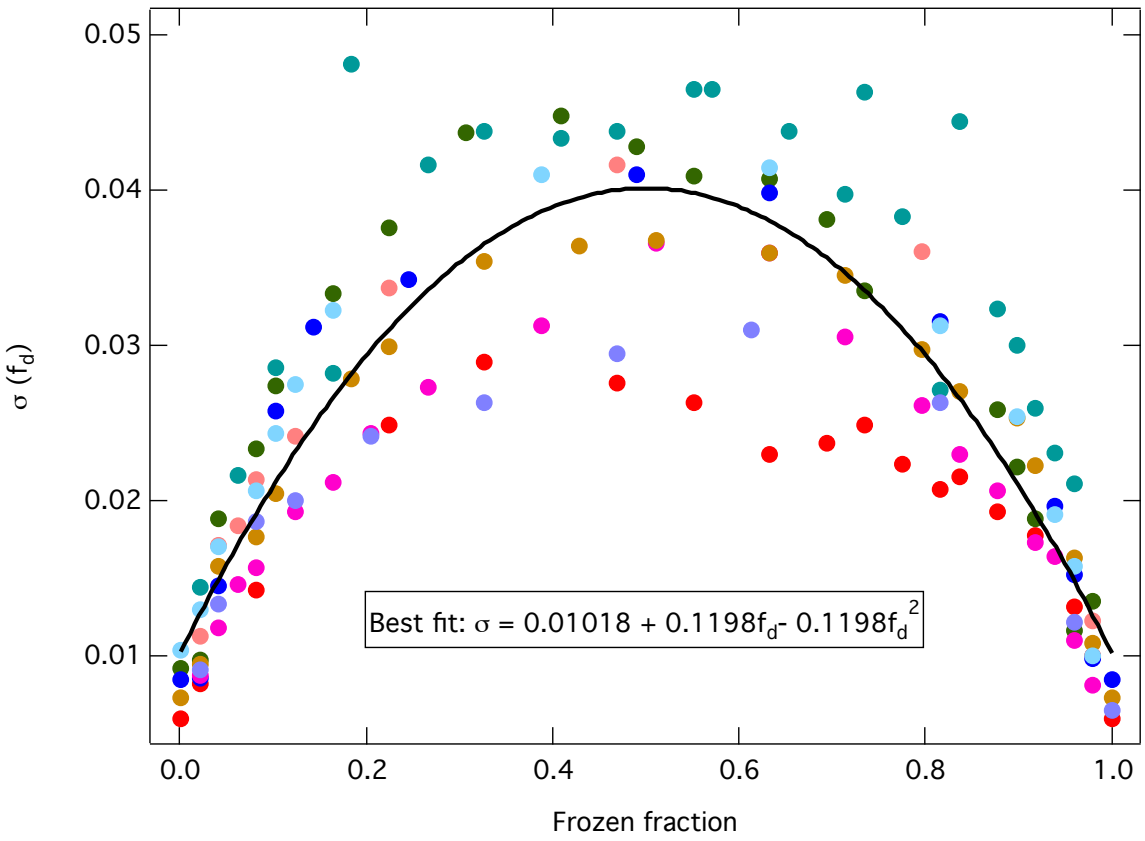

Figure 5.4: Calculated standard deviations of each dataset as a function of frozen fraction. Each data set is shown as a different coloured point. A description of the method used to evaluate $\sigma(f_d)$ is given in the text. The best fit to all of the datasets is shown as a black line.

are based on twice the number of freezing events, the standard deviation determined here is expected to be an upper limit to the relative standard deviation of the measurements.

In order to evaluate the different schemes in terms of their ability to represent the experimental data, the reduced chi-squared (χ^2_{red}) was employed as a means of normalizing the WSSR to the number of measurements as well as the different models. A value of $\chi^2_{\text{red}} > 1$ indicates that the model is not completely representing the data. A value of $\chi^2_{\text{red}} < 1$ indicates that the measurement variance used is too high.

The fraction of drops frozen by fungal spores shown in Fig. 5.1 and bacteria shown in Fig. 5.2 were fit using the schemes described above. Figures 5.5 and 5.6 show the fitting results for the fungal spore and bacteria species studied, respectively. The resulting fit parameters are also

tabulated in Appendix B in Tables B.1, B.2, B.3, and B.4 for the single-α, pdf-α, deterministic and soccer ball schemes, respectively. For the soccer ball scheme (Table B.4), the best fits have $n_{\text{site}} = 1$ for four of the spore types studied (*P. graminis*, *P. triticina*, *P. allii*, and *T. tritici*) indicating that the results from the soccer ball scheme are equivalent to the pdf-α scheme. It should be noted that in the cases where the soccer ball scheme was the same as the pdf-α scheme, the values of χ^2_{red} are larger for the soccer ball scheme than for the pdf-α scheme due to the greater number of fitting parameters for the soccer ball scheme compared with the pdf-α scheme.

Table 5.3 summarizes the χ^2_{red} values for each of the schemes and each of the spore types and bacteria studied. As mentioned above, a χ^2_{red} value close to unity indicates a good fit to the data. In all cases, the single-α model gave χ^2_{red} values above unity indicating a misfit between the experimental data and the nucleation scheme. The deterministic scheme also produces fits with $\chi^2_{\text{red}} > 1$ in seven of the nine species studied. The χ^2_{red} values were, however, significantly smaller than with the single-α scheme in all cases. On the other hand, the soccer ball and pdf-α schemes produced values close to or less than one in the majority of cases, indicating that these schemes were able to reproduce the experimental freezing results. For many of the species studied, only a small difference was observed between the best fit of the pdf-α scheme and the soccer ball scheme. Only *E. harknessii* shows a substantial difference in the resulting χ^2_{red} value for the pdf-α scheme compared with the soccer ball scheme. Some of the results in Table 5.3 for the pdf-α, deterministic, and soccer ball schemes are less than one indicating an overestimation of the variance used to calculate χ^2_{red}.

Table 5.4 shows relative ranking of each of the four schemes investigated based on the χ^2_{red} values from Table 5.3. In cases where the soccer ball scheme gave a best fit with $n_{\text{site}} = 1$, the soccer ball scheme was ranked the same as the pdf-α scheme despite the difference in χ^2_{red} values as described above. As can be seen from the data, in all cases the single-α model is the worst at fitting the heterogeneous freezing results of the fungal spores and bacteria studied. This finding is consistent with previous studies of mineral dust particles [Broadley et al., 2012;

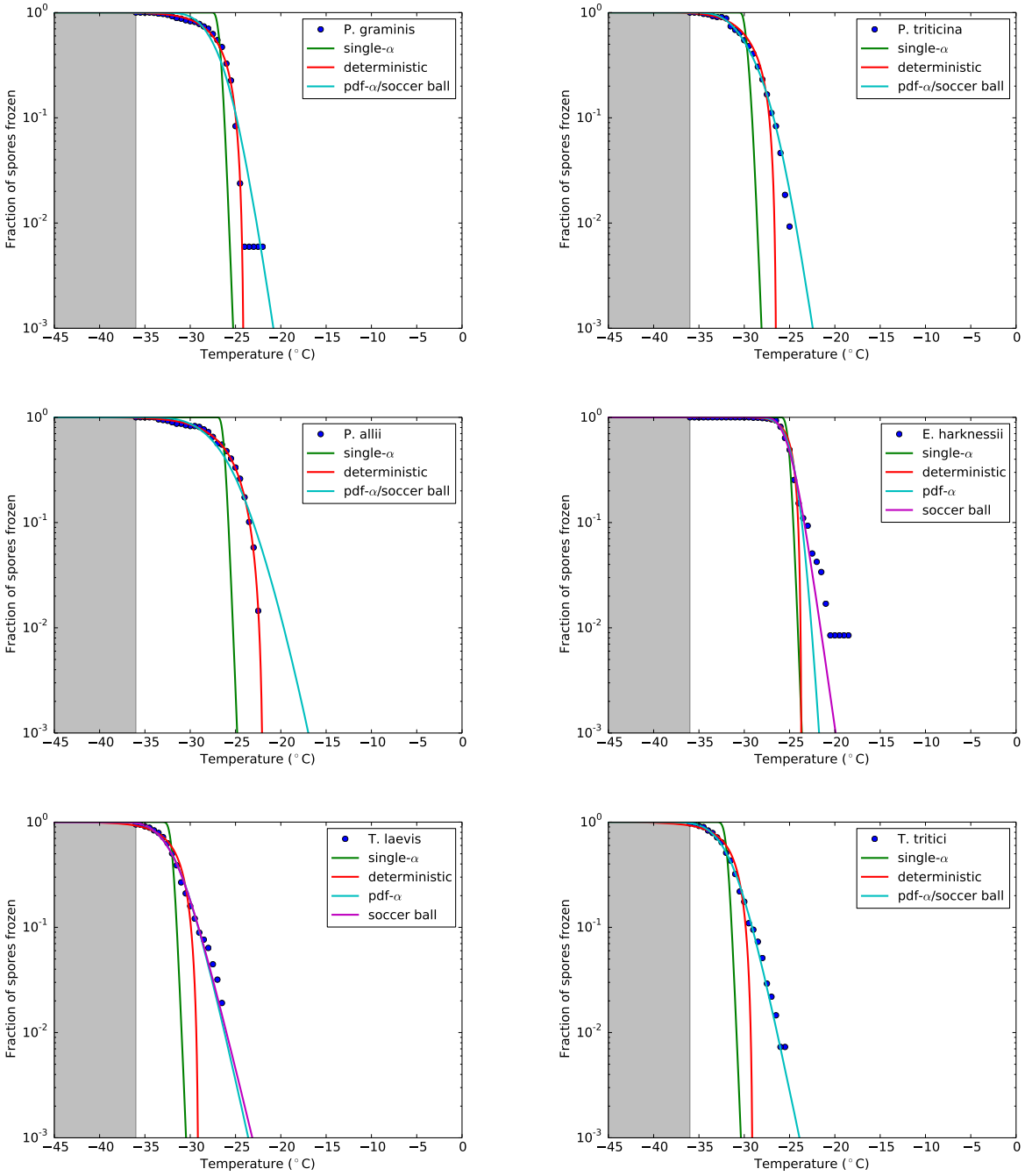

Figure 5.5: Fit results for all fungal spores studied. The shaded region represents the region where homogeneous freezing was observed and where fits to the experimental data were not considered. Experimental freezing data is shown as filled circles, while best fits are shown as solid lines for each of the four schemes studied.

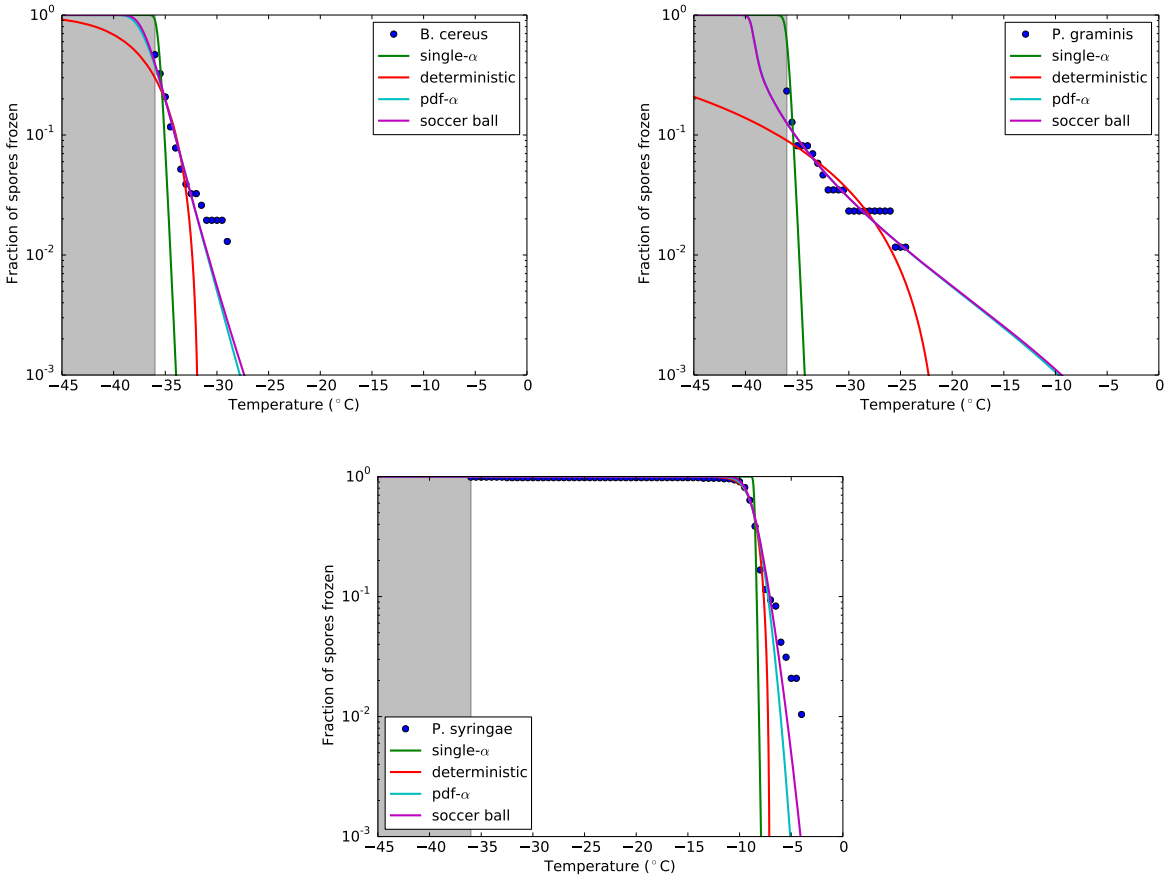

Figure 5.6: Fit results for all bacteria studied. The shaded region shows the region where homogeneous freezing was observed and where fits to the experimental data were not considered. Experimental freezing data is shown as filled circles, while best fits are shown as solid lines for each of the four schemes studied.

Table 5.3: χ^2_{red} values from the fits of all species studied.

Particle Type	Species	single-α	pdf-α	deterministic	soccer ball
Fungi	*P. graminis*	25.248	6.900	0.862	7.176
	P. triticina	32.152	1.079	3.552	1.135
	P. allii	38.160	5.075	1.282	5.286
	E. harknessii	7.739	1.587	3.203	0.921
	T. laevis	31.145	0.853	6.618	0.891
	T. tritici	28.353	0.293	5.319	0.309
Bacteria	*B. cereus*	8.083	0.953	2.531	0.916
	P. graminis	6.256	0.186	0.478	0.194
	P. syringae	6.914	2.836	3.209	2.838

Table 5.4: Relative rankings of different fitting schemes used for all species studied. Schemes are ranked from 1 to 4 where 1 gives the best fit to the data and 4 the worst.

Particle Type	Species	single-α	pdf-α	deterministic	soccer ball
Fungi	*P. graminis*	4	2	1	2
	P. triticina	4	1	3	1
	P. allii	4	2	1	2
	E. harknessii	4	2	3	1
	T. laevis	4	1	3	2
	T. tritici	4	1	3	1
Bacteria	*B. cereus*	4	2	3	1
	P. graminis	4	1	3	2
	P. syringae	4	1	3	2

Lüönd et al., 2010; Marcolli et al., 2007; Vali, 2008, 2014; Welti et al., 2012; Wheeler and Bertram, 2012; Wheeler et al., 2015b]. In seven out of the nine species of fungal spores or bacteria studied, the deterministic scheme ranks third. Only for *P. graminis* and *P. allii* does the deterministic scheme perform better than the stochastic, pdf-α, or soccer ball schemes. In five of the nine species of fungal spores or bacteria studied the pdf-α scheme ranks first, and in all other cases it ranks second. The soccer ball scheme ranks first in four of the nine species studied and ranks second in all other cases. Despite producing equivalent or lower WSSR values than the pdf-α scheme in all cases (*c.f.* WSSR values from Tables B.2 and B.4), the soccer ball scheme only results in smaller χ^2_{red} values in two of the species studied. The reduction in WSSR of the soccer ball scheme is insufficient to overcome the decrease in the degrees of freedom from the soccer ball scheme. These results suggest that the pdf-α scheme gives the highest accuracy when fitting laboratory freezing data of PBAPs.

Two other studies have examined the ability of different nucleation schemes to represent laboratory freezing data of PBAPs. Hartmann et al. [2013] tested the recently developed CHESS (stoCHastic modEl of similar and poiSSon distributed ice nuclei) scheme (not tested in this study) and the single-α scheme on the freezing results of *Pseudomonas syringae* and Snowmax^{TM} (an industrial formulation containing non-viable *P. syringae* cells) from multiple

studies and showed better agreement between scheme and experimental results for the CHESS scheme than the single-α scheme. Augustin et al. [2013] tested the CHESS scheme, single-α scheme, and the soccer ball scheme against the immersion freezing of ice nucleating macromolecules from two samples of Birch pollen. Results showed that the CHESS and soccer ball schemes were both able to reproduce the experimentally determined nucleation rates but that the single-α scheme was not. These results are consistent with the findings of the current study showing that the single-α scheme is least effective at representing heterogeneous freezing data of PBAPs.

5.5 Conclusions

The ability of four different nucleation schemes to represent freezing results from six species of fungal spores and three species of bacteria cells was investigated. Fitting was limited for each scheme to temperatures above $-36\,^{\circ}$C to avoid interferences with homogeneous freezing.

Results show that the single-α scheme was unable to represent the freezing behaviour of all of the samples studied. In five of the nine species studied, the pdf-α scheme provided the best fit to the experimental data. The soccer ball scheme produced fits which were equivalent to the pdf-α scheme in four out of nine species while resulting in fits which were better than the pdf-α scheme in two of the species studied. The pdf-α scheme resulted in fits which were better than the soccer ball scheme in three of the species studied. Only in two cases did the deterministic scheme provide better results than either the pdf-α or soccer ball scheme. The fitting results suggest that the pdf-α scheme can more accurately represent the laboratory freezing data of PBAPs.

Chapter 6

Conclusions and future work

6.1 Ice nucleation properties of mineral dusts

The heterogeneous ice nucleation properties of three different mineral dust species were examined using an optical microscope coupled to a humidity and temperature controlled flow cell.

In Chapter 3, the nucleation conditions of two minerals, kaolinite and illite, in the deposition mode were examined. The onset conditions were determined as a function of total surface area available for nucleation. Results showed that both kaolinite and illite were efficient ice nuclei (IN), being able to nucleate ice at supersaturations of less than 5% over the temperature range of 239–242 K. This is consistent with previous measurements of deposition ice nucleation on both kaolinite and illite [Bailey and Hallett, 2002; Chernoff and Bertram, 2010; Eastwood et al., 2008; Kanji et al., 2008; Möhler et al., 2008a,c; Salam et al., 2006; Welti et al., 2009; Zimmermann et al., 2007, 2008]. The variation in the onset conditions as a function of available surface area for nucleation showed that when only a small number of particles are available for nucleation, the onset saturation for nucleation varies between 100 and 125%.

In Chapter 4, the immersion freezing properties of two mineral dust species, kaolinite and Arizona Test Dust (ATD), were studied. Examination of these species was limited to supermicron sized particles. The results presented are the first size-selected freezing studies to focus on

supermicron dust particles. The freezing temperatures of pure water drops with differing numbers of supermicron mineral dust particles were measured using the same flow cell apparatus as for the deposition measurements in Chapter 3. Results from the freezing showed that both kaolinite and ATD induced nucleation at temperatures warmer than the homogeneous freezing temperature of pure water. ATD was shown to be a more efficient IN than kaolinite with a median freezing temperature of $-30\,^{\circ}$C compared with $-36\,^{\circ}$C for kaolinite.

6.1.1 INAS densities of supermicron mineral dust particles

Also in Chapter 4, the ice nucleation active site (INAS) densities of the supermicron dust particles were calculated and compared with other observations in the literature. INAS densities are useful for comparison of the freezing results of different particle types [Hoose and Möhler, 2012]. The INAS densities of supermicron kaolinite and ATD were shown to be lower than those of submicron particles. Overlap was observed between the results presented here and those experiments where mixtures of supermicron and submicron particles were used. Differences between the INAS densities of kaolinite in the supermicron and submicron mode may be, in part, due to the difference in source of the mineral dust particles studied. For ATD, the difference between supermicron and submicron results may be due to the processing of mineral dust particles, wherein the production of smaller sized particles may lead to greater surface imperfections in these particles. Recent work by Hiranuma et al. [2014] suggests that processing of mineral particles to smaller sizes can increase the INAS densities of these particles. This is significant since a substantial fraction of supermicron mineral dust particles have been shown to exist in the atmosphere [Maring et al., 2003]. Differences in the freezing properties of supermicron and submicron particles should be taken into account when predicting heterogeneous ice nucleation in the atmosphere.

6.2 Testing different schemes to describe atmospheric ice nucleation

In Chapter 3, the deposition freezing results on kaolinite and illite particles was used to test schemes used to describe ice nucleation in atmospheric models. Results showed that the one parameter single-α scheme was unable to describe the results of either the kaolinite or illite data. This is consistent with work by Welti et al. [2009] who showed that a single contact angle was not able to describe deposition ice nucleation on illite or kaolinite. The other schemes, pdf-α, active site, and deterministic, were all able to describe the data within experimental uncertainty. This is consistent with measurements which show that modifications to the single-α scheme are required to accurately predict heterogeneous nucleation data [Archuleta et al., 2005; Hung et al., 2003; Lüönd et al., 2010; Marcolli et al., 2007; Welti et al., 2009].

In Chapter 4 the immersion freezing results of supermicron kaolinite and ATD particles were used to test the same four schemes as in Chapter 3. The schemes were modified to take into account the variability in the number of particles contained in each drop. Results again showed that the single-α scheme was unable to reproduce freezing results from either kaolinite or ATD particles. The active site scheme was shown to be most effective at describing the experimental data with the deterministic and pdf-α schemes falling in between the single-α and active site schemes in terms of their ability to represent the data. In addition, the variation in median freezing temperature with changes in the cooling rate predicted by each scheme was compared with experimental values determined in the literature for both kaolinite and ATD. Results showed that the three stochastic schemes are consistent with the experimental results within a factor of two while the deterministic scheme is inconsistent with experimental data since no change in freezing temperature is expected for the deterministic scheme with variation in the cooling rate.

In Chapter 5, freezing results for nine different types of primary biological aerosol particles (PBAPs) taken from Haga et al. [2013, 2015] were used to test schemes similar to those described above. Immersion freezing data from six different species of fungal spore and three

species of bacteria were used. The single-α and deterministic schemes from Chapters 3 & 4 were used along with a new formulation of the "soccer ball model" [Niedermeier et al., 2014] which was used to evaluate the pdf-α and active site schemes. Results showed that the single-α scheme is unable to represent the freezing of PBAPs while the pdf-α scheme was found to be the best at representing the freezing data.

Overall, deposition and immersion freezing data for mineral dust particles and immersion freezing data for PBAPs were used to test four schemes: the single-α scheme, the pdf-α scheme, the deterministic scheme, and the active site scheme. The tests showed that the single-α scheme is unable to represent deposition nucleation on mineral dust particles or immersion freezing on either mineral dust or PBAP particles. It remains unclear which of the remaining schemes is best at describing deposition nucleation on mineral dust particles. In the case of immersion freezing, the active site scheme was most capable of describing the freezing of mineral dust particles while the pdf-α scheme was best at describing the freezing of PBAPs. The best fit of the immersion freezing of mineral dust particles was described using a three parameter scheme while the immersion freezing of PBAPs was best described using the two parameter pdf-α scheme. A possible explanation for this difference is due to the greater variability in surface properties between the mineral dust and the PBAPs. In the case of mineral dust particles, there is a great amount of irregularity in the surface structure from particle to particle. For PBAPs, each of the particles of the same species has much less surface variability since they are all created through the same biological process.

Recent work has shown that the predictions of classical nucleation theory (CNT) can vary by as many as 25 orders of magnitude depending on the values of the free parameters used [Ickes et al., 2015], most notably the interfacial energy and the energy of self-diffusion. While the values of the fits performed here will vary depending on the values of the input parameters used, the conclusions presented here are not expected to change. The fits presented here can be used to predict the freezing results in climate simulations as long as the same input parameters are used as those used here. Additionally, the relative ability of the different schemes to fit the

experimental data is not expected to depend on the parameters used in the fitting.

The single-α scheme has been used extensively to represent heterogeneous ice nucleation in atmospheric models [e.g. Hoose et al., 2010a,b; Jensen and Toon, 1997; Jensen et al., 1998; Kärcher, 1996, 1998; Kärcher et al., 1998; Khvorostyanov and Curry, 2000, 2004, 2005, 2009; Kulkarni et al., 2012; Liu et al., 2007; Morrison et al., 2005]. The results presented here along with recent modelling studies which show the cloud properties determined from atmospheric models to be dependent on the nucleation scheme used [Eidhammer et al., 2009; Ervens and Feingold, 2012; Kulkarni et al., 2012; Wang and Liu, 2014; Wang et al., 2014] suggest that the predictions of the indirect effect of IN on climate may actually be different than what has been predicted by previous modelling studies which utilize the single-α scheme. Results from testing the different schemes presented here should allow modellers to better select how heterogeneous ice nucleation is incorporated into atmospheric models. Additionally, the fitting parameters from the studies presented here may be used to describe heterogeneous freezing by certain particle types in cloud or climate models.

6.3 Future research

Our understanding of the fundamental processes involved in heterogeneous ice nucleation is still lacking and many research questions remain about ice nucleation. For example, Marcolli [2014] recently suggested that deposition nucleation may not represent a unique mode of ice nucleation but rather is homogeneous or heterogeneous immersion freezing of supercooled water condensed in pores on the particle surface. This would represent a fundamental change in our understanding of the nucleation process. A more detailed examination involving ice nucleation experiments on pore-free surfaces such as freshly cleaved mica surfaces may help determine the conditions for deposition nucleation. Additionally, molecular simulations building on the work of Croteau et al. [2010] examining the formation of ice in pores compared with flat surfaces may provide insight into deposition nucleation. In Chapter 4 the nucleating efficiency of supermicron dust particles was shown to be different than that of submicron dust

particles. Further laboratory studies examining both submicron and supermicron dust particles prepared in the same manner and measuring the freezing temperature using the same apparatus would help answer the question of size dependence on ice nucleation. As mineral dust is thought to be one of the main IN in the atmosphere [Hoose et al., 2008], it would be interesting to incorporate the results obtained from the fitting of supermicron dust particles alongside submicron dust particles. Finally, data on parameterizing PBAPs for incorporation into atmospheric models is limited. Work by Hoose et al. [2010a] suggests that PBAPs do not contribute significantly to the total atmospheric ice nucleation rate. However, recent studies have suggested that PBAPs may influence cloud properties on regional or local scales [Hazra, 2013; Gonçalves et al., 2012; Costa et al., 2014]. This may indicate a need for more information regarding the types of PBAPs responsible for ice nucleation in regional air masses and measurements of the ice nucleating ability of these particles. Field studies examining the PBAPs found in and out of clouds would allow for better determination of the specific species which may be responsible for ice formation. The freezing ability of these particles must be carefully measured and parameterized in order to be included in any modelling of regional climate and weather.

Bibliography

B. A. Albrecht. Aerosols, cloud microphysics, and fractional cloudiness. *Science (New York, N.Y.)*, 245(4923):1227–30, September 1989. doi: 10.1126/science.245.4923.1227. URL http://www.ncbi.nlm.nih.gov/pubmed/17747885. → pages 10

A. A. Andersen. New sampler for the collection, sizing, and enumeration of viable airborne particles. *Journal of Bacteriology*, 76(5):471–484, November 1958. URL http://www.pubmedcentral.nih.gov/articlerender.fcgi?artid=290224&tool=pmcentrez&rendertype=abstract. → pages 53

A. Ansmann, M. Tesche, D. Althausen, D. Müller, P. Seifert, V. Freudenthaler, B. Heese, M. Wiegner, G. Pisani, P. Knippertz, and O. Dubovik. Influence of Saharan dust on cloud glaciation in southern Morocco during the Saharan Mineral Dust Experiment. *Journal of Geophysical Research*, 113(D4):D04210, February 2008. doi: 10.1029/2007JD008785. URL http://www.agu.org/pubs/crossref/2008/2007JD008785.shtml. → pages 7, 23

A. Ansmann, M. Tesche, P. Seifert, D. Althausen, R. Engelmann, J. Fruntke, U. Wandinger, I. Mattis, and D. Müller. Evolution of the ice phase in tropical altocumulus: SAMUM lidar observations over Cape Verde. *Journal of Geophysical Research: Atmospheres*, 114:1–20, 2009. doi: 10.1029/2008JD011659. → pages 7

C. M. Archuleta, P. J. DeMott, and S. M. Kreidenweis. Ice nucleation by surrogates for atmospheric mineral dust and mineral dust/sulfate particles at cirrus temperatures. *Atmospheric Chemistry and Physics*, 5(10):2617–2634, October 2005. doi: 10.5194/acp-5-2617-2005. URL http://www.atmos-chem-phys.net/5/2617/2005/. → pages 22, 45, 105

J. D. Atkinson, B. J. Murray, M. T. Woodhouse, T. F. Whale, K. J. Baustian, K. S. Carslaw, S. Dobbie, D. O'Sullivan, and T. L. Malkin. The importance of feldspar for ice nucleation by mineral dust in mixed-phase clouds. *Nature*, 498(7454):355–358, June 2013. doi: 10.1038/nature12278. URL http://www.ncbi.nlm.nih.gov/pubmed/23760484. → pages 48

S. Augustin, H. Wex, D. Niedermeier, B. Pummer, H. Grothe, S. Hartmann, L. Tomsche, T. Clauss, J. Voigtländer, K. Ignatius, and F. Stratmann. Immersion freezing of birch pollen washing water. *Atmospheric Chemistry and Physics*, 13(21):10989–11003, November 2013. doi: 10.5194/acp-13-10989-2013. URL http://www.atmos-chem-phys.net/13/10989/2013/. → pages 86, 102

M. Bailey and J. Hallett. Nucleation effects on the habit of vapour grown ice crystals from 18 to 42C. *Quarterly Journal of the Royal Meteorological Society*, 128(583):1461–1483, July 2002. doi: 10.1002/qj.200212858304. URL http://doi.wiley.com/10.1002/qj.200212858304. → pages 32, 103

M. B. Baker and T. Peter. Small-scale cloud processes and climate. *Nature*, 451(7176): 299–300, January 2008. doi: 10.1038/nature06594. URL http://www.ncbi.nlm.nih.gov/pubmed/18202649. → pages 21

D. Barahona, J. Rodriguez, and A. Nenes. Sensitivity of the global distribution of cirrus ice crystal concentration to heterogeneous freezing. *Journal of Geophysical Research*, 115 (D23):D23213, December 2010. doi: 10.1029/2010JD014273. URL http://www.agu.org/pubs/crossref/2010/2010JD014273.shtml. → pages 23

O. Boucher, D. Randall, P. Artaxo, C. Bretherton, G. Feingold, P. Forster, V.-M. Kerminen, Y. Kondo, H. Liao, U. Lohmann, P. Rasch, S. K. Satheesh, S. Sherwood, B. Stevens, and X.-Y. Zhang. Clouds and aerosols. In T F Stocker, D Qin, G.-K. Plattner, M. Tignor, S.K. Allen, J. Boschung, A. Nauels, Y. Xia, V. Bex, and P.M. Midgley, editors, *Climate Change 2013: The Physical Science Basis. Contribution of Working Group I to the Fifth Assessment Report of the Intergovernmental Panel on Climate Change*, chapter 7. Cambridge, United Kingdom and New York, NY, USA, 2013. → pages 2, 3, 84

R. M. Bowers, C. L. Lauber, C. Wiedinmyer, M. Hamady, A. G. Hallar, R. Fall, R. Knight, and N. Fierer. Characterization of airborne microbial communities at a high-elevation site and their potential to act as atmospheric ice nuclei. *Applied and Environmental Microbiology*, 75(15):5121–30, August 2009. doi: 10.1128/AEM.00447-09. URL http://www.pubmedcentral.nih.gov/articlerender.fcgi?artid=2725505&tool=pmcentrez&rendertype=abstract. → pages 8, 85

S. L. Broadley, B. J. Murray, R. J. Herbert, J. D. Atkinson, S. Dobbie, T. L. Malkin, E. Condliffe, and L. Neve. Immersion mode heterogeneous ice nucleation by an illite rich powder representative of atmospheric mineral dust. *Atmospheric Chemistry and Physics*,

12(1):287–307, January 2012. doi: 10.5194/acp-12-287-2012. URL http://www.atmos-chem-phys.net/12/287/2012/. → pages xi, xiii, 8, 49, 50, 72, 76, 86, 98

R. E. Buchanan and N. E. Gibbons. *Bergey's manual of determinative bacteriology*. The Williams & Wilkins Company, Baltimore, 1974. → pages xii, 88

S. M. Burrows, C. Hoose, U. Pöschl, and M. G. Lawrence. Ice nuclei in marine air: biogenic particles or dust? *Atmospheric Chemistry and Physics*, 13(1):245–267, January 2013. doi: 10.5194/acp-13-245-2013. URL http://www.atmos-chem-phys.net/13/245/2013/. → pages 85

W. Cantrell and A. Heymsfield. Production of ice in tropospheric clouds: A review. *Bulletin of the American Meteorological Society*, 86(6):795–807, June 2005. doi: 10.1175/BAMS-86-6-795. URL http://journals.ametsoc.org/doi/abs/10.1175/BAMS-86-6-795. → pages 21

J.-P. Chen, A. Hazra, and Z. Levin. Parameterizing ice nucleation rates using contact angle and activation energy derived from laboratory data. *Atmospheric Chemistry and Physics*, 8 (24):7431–7449, December 2008. doi: 10.5194/acp-8-7431-2008. URL http://www.atmos-chem-phys.net/8/7431/2008/. → pages 22

D. I. Chernoff and A. K. Bertram. Effects of sulfate coatings on the ice nucleation properties of a biological ice nucleus and several types of minerals. *Journal of Geophysical Research: Atmospheres*, 115(D20):D20205, October 2010. doi: 10.1029/2010JD014254. URL http://www.agu.org/pubs/crossref/2010/2010JD014254.shtml. → pages 22, 27, 32, 51, 103

S. J. Chipera and D. L. Bish. Baseline studies of the clay minerals society source clays: Powder X-ray diffraction analyses. *Clays and Clay Minerals*, 49(5):398–409, 2001. doi: 10.1346/CCMN.2001.0490507. URL http://www.clays.org/journal/archive/volume49/49-5-398.pdf. → pages 50

B. C. Christner, R. Cai, C. E. Morris, K. S. McCarter, C. M. Foreman, M. L. Skidmore, S. N. Montross, and D. C. Sands. Geographic, seasonal, and precipitation chemistry influence on the abundance and activity of biological ice nucleators in rain and snow. *Proceedings of the National Academy of Sciences of the United States of America*, 105(48):18854–9, December 2008a. doi: 10.1073/pnas.0809816105. URL http://www.pubmedcentral.nih.gov/articlerender.fcgi?artid=2596265&tool=pmcentrez&rendertype=abstract. → pages 8, 85

B. C. Christner, C. E. Morris, C. M. Foreman, R. Cai, and D. C. Sands. Ubiquity of biological ice nucleators in snowfall. *Science (New York, N.Y.)*, 319(5867):1214, February 2008b. doi: 10.1126/science.1149757. URL http://www.pubmedcentral.nih.gov/articlerender.fcgi?artid=2596265&tool=pmcentrez&rendertype=abstracthttp://www.ncbi.nlm.nih.gov/pubmed/18309078. → pages 8, 85

T. Claquin, M. Schulz, and Y. J. Balkanski. Modeling the mineralogy of atmospheric dust sources. *Journal of Geophysical Research: Atmospheres*, 104(D18):22243–22256, 1999. doi: 10.1029/1999JD900416. URL http://www.agu.org/pubs/crossref/1999/1999JD900416.shtml. → pages 23, 50

P. J. Connolly, O. Möhler, P. R. Field, H. Saathoff, R. Burgess, T. Choularton, and M. Gallagher. Studies of heterogeneous freezing by three different desert dust samples. *Atmospheric Chemistry and Physics*, 9(8):2805–2824, April 2009. doi: 10.5194/acp-9-2805-2009. URL http://www.atmos-chem-phys.net/9/2805/2009/. → pages 13, 23, 43, 44, 48, 49, 50, 68, 77

H. A. Constantinidou, S. S. Hirano, L. S. Baker, and C. D. Upper. Atmospheric dispersal of ice nucleation-active bacteria: The role of rain. *Phytopathology*, 80(10):934, 1990. doi: 10.1094/Phyto-80-934. URL http://www.apsnet.org/publications/phytopathology/backissues/Documents/1990Abstracts/Phyto80_934.htm. → pages 8, 85

T. S. Costa, F. L. T. Gonçalves, M. A. Yamasoe, J. A. Martins, and C. E. Morris. Bacterial ice nuclei impact cloud lifetime and radiative properties and reduce atmospheric heat loss in the BRAMS simulation model. *Environmental Research Letters*, 9(8):084020, August 2014. doi: 10.1088/1748-9326/9/8/084020. URL http://stacks.iop.org/1748-9326/9/i=8/a=084020?key=crossref.50c64372d900cc86bb4a74f1936bb204. → pages 5, 85, 108

T. Croteau, A. K. Bertram, and G. N. Patey. Adsorption and structure of water on kaolinite surfaces: possible insight into ice nucleation from grand canonical monte carlo calculations. *The Journal of Physical Chemistry A*, 112(43):10708–10712, October 2008. doi: 10.1021/jp805615q. URL http://www.ncbi.nlm.nih.gov/pubmed/18785690. → pages 43

T. Croteau, A. K. Bertram, and G. N. Patey. Observations of high-density ferroelectric ordered water in kaolinite trenches using Monte Carlo simulations. *The Journal of Physical Chemistry A*, 114(32):8396–8405, August 2010. doi: 10.1021/jp104643p. URL http://www.ncbi.nlm.nih.gov/pubmed/20701348. → pages 43, 107

D. J. Cziczo, D. M. Murphy, P. K. Hudson, and D. S. Thomson. Single particle measurements of the chemical composition of cirrus ice residue during CRYSTAL-FACE. *Journal of Geophysical Research: Atmospheres*, 109(D4):D04201, 2004. doi: 10.1029/2003JD004032. URL http://www.agu.org/pubs/crossref/2004/2003JD004032.shtml. → pages 7, 23, 48

D. J. Cziczo, K. D. Froyd, S. J. Gallavardin, O. Moehler, S. Benz, H. Saathoff, and D. M. Murphy. Deactivation of ice nuclei due to atmospherically relevant surface coatings. *Environmental Research Letters*, 4(4):044013, October 2009. doi: 10.1088/1748-9326/4/4/044013. URL http://iopscience.iop.org/1748-9326/4/4/044013/. → pages 50

D. J. Cziczo, K. D. Froyd, C. Hoose, E. J. Jensen, M. Diao, M. A. Zondlo, J. B. Smith, C. H. Twohy, and D. M. Murphy. Clarifying the dominant sources and mechanisms of cirrus cloud formation. *Science (New York, N.Y.)*, 340(6138):1320–1324, June 2013. doi: 10.1126/science.1234145. URL http://www.ncbi.nlm.nih.gov/pubmed/23661645. → pages 7, 48

G. De Boer, H. Morrison, M. D. Shupe, and R. Hildner. Evidence of liquid dependent ice nucleation in high-latitude stratiform clouds from surface remote sensors. *Geophysical Research Letters*, 38(January):1–5, 2011. doi: 10.1029/2010GL046016. → pages 7

N. DeLeon-Rodriguez, T. L. Lathem, L. M. Rodriguez-R, J. M. Barazesh, B. E. Anderson, A. J. Beyersdorf, L. D. Ziemba, M. Bergin, A. Nenes, and K. T. Konstantinidis. Microbiome of the upper troposphere: species composition and prevalence, effects of tropical storms, and atmospheric implications. *Proceedings of the National Academy of Sciences of the United States of America*, 110(7):2575–80, February 2013. doi: 10.1073/pnas.1212089110. URL http://www.pubmedcentral.nih.gov/articlerender.fcgi?artid=3574924&tool=pmcentrez&rendertype=abstract. → pages 4

P. J. DeMott. Quantitative descriptions of ice formation mechanisms of silver iodide-type aerosols. *Atmospheric Research*, 38(1-4):63–99, September 1995. doi: 10.1016/0169-8095(94)00088-U. URL http://www.sciencedirect.com/science/article/pii/016980959400088U. → pages 77

P. J. DeMott. Laboratory studies of cirrus cloud processes. In D. K. Lynch, K. Sassen, D. O'C. Starr, and G. Stephens, editors, *Cirrus*, pages 102–136. Oxford University Press, New York, 2002. → pages 21

P. J. DeMott, D. J. Cziczo, A. J. Prenni, D. M. Murphy, S. M. Kreidenweis, D. S. Thomson, R. Borys, and D. C. Rogers. Measurements of the concentration and composition of nuclei for cirrus formation. *Proceedings of the National Academy of Sciences of the United States of America*, 100(25):14655–14660, December 2003a. doi: 10.1073/pnas.2532677100. URL http://www.pnas.org/content/100/25/14655. → pages 7, 23, 48

P. J. DeMott, K. Sassen, M. R. Poellot, D. Baumgardner, D. C. Rogers, S. D. Brooks, A. J. Prenni, and S. M. Kreidenweis. African dust aerosols as atmospheric ice nuclei. *Geophysical Research Letters*, 30(14):1732, 2003b. doi: 10.1029/2003GL017410. URL http://www.agu.org/pubs/crossref/2003/2003GL017410.shtml. → pages 7, 48

P. J. DeMott, A. J. Prenni, X. Liu, S. M. Kreidenweis, M. D. Petters, C. H. Twohy, M. S. Richardson, T. Eidhammer, and D. C. Rogers. Predicting global atmospheric ice nuclei distributions and their impacts on climate. *Proceedings of the National Academy of Sciences of the United States of America*, 107(25):11217–11222, June 2010. doi: 10.1073/pnas.0910818107. URL http://www.pnas.org/content/107/25/11217. → pages xiv, 12, 13, 47, 84

K. L. Denman, G. Brasseur, A. Chidthaisong, P. Ciais, P. M. Cox, R. E. Dickinson, D. Hauglustaine, C. Heinze, E. Holland, D. Jacob, U. Lohmann, S. Ramachandran, P. L. da Silva Dias, S. C. Wofsy, and X. Zhang. Couplings between changes in the climate system and biogeochemistry. In S Solomon, D Qin, M Manning, Z Chen, M Marquis, KB Averyt, M Tignor, and HL Miller, editors, *Climate Change 2007: The Physical Science Basis. Contribution of Working Group I to the Fourth Assessment Report of the Intergovernmental Panel on Climate Change*, chapter Couplings, pages 499–587. Cambridge University Press, Cambridge, UK, 2007. → pages 10, 47

V. R. Després, J. A. Huffman, S. M. Burrows, C. Hoose, A. S. Safatov, G. Buryak, J. Fröhlich-Nowoisky, W. Elbert, M. O. Andreae, U. Pöschl, and R. Jaenicke. Primary biological aerosol particles in the atmosphere: a review. *Tellus B*, 64, February 2012. doi: 10.3402/tellusb.v64i0.15598. URL http://www.tellusb.net/index.php/tellusb/article/view/15598. → pages xiii, 3, 4, 5, 9, 85

K. Diehl and S. Wurzler. Heterogeneous drop freezing in the immersion mode: Model calculations considering soluble and insoluble particles in the drops. *Journal of the Atmospheric Sciences*, 61(16):2063–2072, August 2004. doi: 10.1175/1520-0469(2004)061⟨2063:HDFITI⟩2.0.CO;2. URL http://journals.ametsoc.org/doi/abs/10.1175/1520-0469%282004%29061%3C2063%3AHDFITI%3E2.0.CO%3B2. → pages 86

K. Diehl and S. Wurzler. Air parcel model simulations of a convective cloud: Bacteria acting as immersion ice nuclei. *Atmospheric Environment*, 44(36):4622–4628, November 2010. doi: 10.1016/j.atmosenv.2010.08.003. URL http://linkinghub.elsevier.com/retrieve/pii/S1352231010006564. → pages 48

K. Diehl, M. Simmel, and S. Wurzler. Numerical sensitivity studies on the impact of aerosol properties and drop freezing modes on the glaciation, microphysics, and dynamics of clouds. *Journal of Geophysical Research*, 111(D7):D07202, 2006. doi: 10.1029/2005JD005884. URL http://doi.wiley.com/10.1029/2005JD005884. → pages 86

M. Dymarska, B. J. Murray, L. Sun, M. L. Eastwood, D. A. Knopf, and A. K. Bertram. Deposition ice nucleation on soot at temperatures relevant for the lower troposphere. *Journal of Geophysical Research: Atmospheres*, 111(D4):D04204, 2006. doi: 10.1029/2005JD006627. URL http://www.agu.org/pubs/crossref/2006/2005JD006627.shtml. → pages 24, 27, 51

M. L. Eastwood, S. Cremel, C. Gehrke, E. Girard, and A. K. Bertram. Ice nucleation on mineral dust particles: Onset conditions, nucleation rates and contact angles. *Journal of Geophysical Research: Atmospheres*, 113(D22):D22203, November 2008. doi: 10.1029/2008JD010639. URL http://www.agu.org/pubs/crossref/2008/2008JD010639.shtml. → pages 22, 24, 27, 32, 43, 44, 48, 51, 75, 103, 136

M. L. Eastwood, S. Cremel, M. Wheeler, B. J. Murray, E. Girard, and A. K. Bertram. Effects of sulfuric acid and ammonium sulfate coatings on the ice nucleation properties of kaolinite particles. *Geophysical Research Letters*, 36(2):L02811, January 2009. doi: 10.1029/2008GL035997. URL http://www.agu.org/pubs/crossref/2009/2008GL035997.shtml. → pages 22, 27, 51

M. Ebert, A. Worringen, N. Benker, S. Mertes, E. Weingartner, and S. Weinbruch. Chemical composition and mixing-state of ice residuals sampled within mixed phase clouds. *Atmospheric Chemistry and Physics*, 11(6):2805–2816, March 2011. doi: 10.5194/acp-11-2805-2011. URL http://www.atmos-chem-phys.net/11/2805/2011/. → pages 7, 48

T. Eidhammer, P. J. DeMott, and S. M. Kreidenweis. A comparison of heterogeneous ice nucleation parameterizations using a parcel model framework. *Journal of Geophysical Research*, 114(D6):D06202, March 2009. doi: 10.1029/2008JD011095. URL http://www.agu.org/pubs/crossref/2009/2008JD011095.shtml. → pages 48, 63, 68, 85, 107

J. P. Engelbrecht and E. Derbyshire. Airborne mineral dust. *Elements*, 6:241–246, 2010. doi: 10.2113/gselements.6.4.241. → pages 2

B. Ervens and G. Feingold. On the representation of immersion and condensation freezing in cloud models using different nucleation schemes. *Atmospheric Chemistry and Physics*, 12 (13):5807–5826, July 2012. doi: 10.5194/acp-12-5807-2012. URL http://www.atmos-chem-phys.net/12/5807/2012/. → pages 48, 63, 65, 68, 85, 107

N. H. Fletcher. Size effect in heterogeneous nucleation. *The Journal of Chemical Physics*, 29 (3):572–576, 1958. doi: 10.1063/1.1744540. URL http://link.aip.org/link/?JCPSA6/29/572/1. → pages 13, 36, 49, 63

N. H. Fletcher. Entropy effect in ice crystal nucleation. *The Journal of Chemical Physics*, 30 (6):1476, 1959. doi: 10.1063/1.1730221. URL http://link.aip.org/link/?JCPSA6/30/1476/1http://link.aip.org/link/JCPSA6/v30/i6/p1476/s1&Agg=doi. → pages 36

N. H. Fletcher. Active sites and ice crystal nucleation. *Journal of the Atmospheric Sciences*, 26(6):1266–1271, November 1969. doi: 10.1175/1520-0469(1969)026⟨1266:ASAICN⟩2.0.CO;2. URL http://journals.ametsoc.org/doi/abs/10.1175/1520-0469(1969)026⟨1266:ASAICN⟩2.0.CO;2. → pages 13, 22, 23, 39, 49, 66, 91

A. P. Fornea, S. D. Brooks, J. B. Dooley, and A. Saha. Heterogeneous freezing of ice on atmospheric aerosols containing ash, soot, and soil. *Journal of Geophysical Research*, 114 (D13):D13201, July 2009. doi: 10.1029/2009JD011958. URL http://www.agu.org/pubs/crossref/2009/2009JD011958.shtml. → pages 22

P. Forster, V. Ramaswamy, P. Artaxo, T. Berntsen, R. Betts, D. W. Fahey, J. Haywood, J. Lean, D. C. Lowe, G. Myhre, J. Nganga, R. Prinn, G. Raga, M. Schulz, and R. van Dorland. Changes in atmospheric constituents and in radiative forcing. In S Solomon, D Quin, M Manning, Z Chen, M Marquis, KB Averyt, M Tignor, and HL Miller, editors, *Climate Change 2007: The Physical Science Basis. Contribution of Working Group I to the Fourth Assessment Report of the Intergovernmental Panel on Climate Change*. Cambridge University Press, United Kingdom and New York, NY, USA, 2007. URL http://meteosat.com/ipcc4/Ch02_SOD_Text_TSU_FINAL.pdf. → pages 2

B. Friedman, G. Kulkarni, J. Beránek, A. Zelenyuk, J. A. Thornton, and D. J. Cziczo. Ice nucleation and droplet formation by bare and coated soot particles. *Journal of Geophysical*

Research: Atmospheres, 116(D17):D17203, September 2011. doi: 10.1029/2011JD015999. URL http://www.agu.org/pubs/crossref/2011/2011JD015999.shtml. → pages 50, 79

E. Garcia, T. C. J. Hill, A. J. Prenni, P. J. DeMott, G. D. Franc, and S. M. Kreidenweis. Biogenic ice nuclei in boundary layer air over two U.S. High Plains agricultural regions. *Journal of Geophysical Research: Atmospheres*, 117(D18):n/a–n/a, September 2012. doi: 10.1029/2012JD018343. URL http://doi.wiley.com/10.1029/2012JD018343. → pages 8, 85

R. A. Glaccum and J. M. Prospero. Saharan aerosols over the tropical North Atlantic - Mineralogy. *Marine Geology*, 37(3-4):295–321, September 1980. doi: 10.1016/0025-3227(80)90107-3. URL http://www.sciencedirect.com/science/article/pii/0025322780901073. → pages 50

F. L. T. Gonçalves, J. A. Martins, R. I. Albrecht, C. A. Morales, M. A. Silva Dias, and C. E. Morris. Effect of bacterial ice nuclei on the frequency and intensity of lightning activity inferred by the BRAMS model. *Atmospheric Chemistry and Physics*, 12(13):5677–5689, July 2012. doi: 10.5194/acp-12-5677-2012. URL http://www.atmos-chem-phys.net/12/5677/2012/. → pages 5, 85, 108

B. Z. Gorbunov and N. A. Kakutkina. Ice crystal formation on aerosol particles with a non-uniform surface. *Journal of Aerosol Science*, 13(1):21–28, January 1982. doi: 10.1016/0021-8502(82)90004-0. URL http://linkinghub.elsevier.com/retrieve/pii/0021850282900040. → pages 23, 39

J. D. Hader, T. P. Wright, and M. D. Petters. Contribution of pollen to atmospheric ice nuclei concentrations. *Atmospheric Chemistry and Physics*, 14(11):5433–5449, June 2014. doi: 10.5194/acp-14-5433-2014. URL http://www.atmos-chem-phys.net/14/5433/2014/. → pages 78, 80, 82

D. I. Haga, R. Iannone, M. J. Wheeler, R. Mason, E. A. Polishchuk, T. Fetch, B. J. van der Kamp, I. G. McKendry, and A. K. Bertram. Ice nucleation properties of rust and bunt fungal spores and their transport to high altitudes, where they can cause heterogeneous freezing. *Journal of Geophysical Research: Atmospheres*, 118(13):7260–7272, July 2013. doi: 10.1002/jgrd.50556. URL http://doi.wiley.com/10.1002/jgrd.50556. → pages v, ix, xi, xx, 4, 51, 78, 86, 87, 89, 90, 95, 105

D. I. Haga, V. E. Irish, M. J. Wagstaff, M. J. Wheeler, R. Mason, J. Chen, N. DeLeon-Rodriguez, K. T. Konstantinidis, T. L. Lathem, B. E. Anderson, A. Nenes, D. Horne, and A. K. Bertram. Ice nucleation in droplets containing bacteria that have been

identified in the atmosphere: Immersion freezing results and atmospheric implications. *in press*, 2015. → pages v, ix, xii, xx, 86, 87, 88, 89, 91, 95, 105

J.-H. Han, H.-M. Hung, and S. T. Martin. Size effect of hematite and corundum inclusions on the efflorescence relative humidities of aqueous ammonium nitrate particles. *Journal of Geophysical Research*, 107(D10), 2002. doi: 10.1029/2001JD001054. URL http://www.agu.org/pubs/crossref/2002/2001JD001054.shtml. → pages 23, 39

S. Hartmann, S. Augustin, T. Clauss, H. Wex, T. Šantl Temkiv, J. Voigtländer, D. Niedermeier, and F. Stratmann. Immersion freezing of ice nucleation active protein complexes. *Atmospheric Chemistry and Physics*, 13(11):5751–5766, June 2013. doi: 10.5194/acp-13-5751-2013. URL http://www.atmos-chem-phys.net/13/5751/2013/. → pages 13, 86, 101

A. Hazra. Role of mineral dust, soot, and bacteria in cloud and precipitation formation processes over Indian subcontinent using an atmospheric general circulation model. *Journal of Atmospheric and Solar-Terrestrial Physics*, 98:74–85, June 2013. doi: 10.1016/j.jastp.2013.02.019. URL http://linkinghub.elsevier.com/retrieve/pii/S1364682613000680. → pages 5, 85, 108

D. A. Hegg and M. B. Baker. Nucleation in the atmosphere. *Reports on Progress in Physics*, 72(5):056801, May 2009. doi: 10.1088/0034-4885/72/5/056801. URL http://stacks.iop.org/0034-4885/72/i=5/a=056801?key=crossref.f411bc4f77ac97b6cda15ee45dc74b87. → pages 21

J. Heintzenberg, K. Okada, and J. Ström. On the composition of non-volatile material in upper tropospheric aerosols and cirrus crystals. *Atmospheric Research*, 41(1):81–88, June 1996. doi: 10.1016/0169-8095(95)00042-9. URL http://linkinghub.elsevier.com/retrieve/pii/0169809595000429. → pages 7, 23

H. Herich, T. Tritscher, A. Wiacek, M. Gysel, E. Weingartner, U. Lohmann, U. Baltensperger, and D. J. Cziczo. Water uptake of clay and desert dust aerosol particles at sub- and supersaturated water vapor conditions. *Physical Chemistry Chemical Physics*, 11(36): 7804–7909, September 2009. doi: 10.1039/b901585j. URL http://www.ncbi.nlm.nih.gov/pubmed/19727482http://www.ncbi.nlm.nih.gov/pubmed/19727486. → pages 52

S. S. Hirano and C. D. Upper. Bacteria in the leaf ecosystem with emphasis on Pseudomonas syringae–a pathogen, ice nucleus, and epiphyte. *Microbiology and Molecular Biology*

Reviews, 64(3):624–653, September 2000. doi: 10.1128/MMBR.64.3.624-653.2000. URL http://www.pubmedcentral.nih.gov/articlerender.fcgi?artid=99007&tool=pmcentrez&rendertype=abstracthttp://mmbr.asm.org/cgi/doi/10.1128/MMBR.64.3.624-653.2000. → pages 9

N. Hiranuma, N. Hoffmann, A. Kiselev, A. Dreyer, K. Zhang, G. Kulkarni, T. Koop, and O. Möhler. Influence of surface morphology on the immersion mode ice nucleation efficiency of hematite particles. *Atmospheric Chemistry and Physics*, 14(5):2315–2324, March 2014. doi: 10.5194/acp-14-2315-2014. URL http://www.atmos-chem-phys.net/14/2315/2014/. → pages 79, 80, 82, 104

T. E. Hoffer. A laboratory investigation of droplet freezing. *Journal of Meteorology*, 18(6):766–778, December 1961. doi: 10.1175/1520-0469(1961)018⟨0766:ALIODF⟩2.0.CO;2. URL http://journals.ametsoc.org/doi/abs/10.1175/1520-0469(1961)018⟨0766:ALIODF⟩2.0.CO;2. → pages 50, 60

C. Hoose and O. Möhler. Heterogeneous ice nucleation on atmospheric aerosols: A review of results from laboratory experiments. *Atmospheric Chemistry and Physics*, 12(20):9817–9854, October 2012. doi: 10.5194/acp-12-9817-2012. URL http://www.atmos-chem-phys.net/12/9817/2012/. → pages 7, 8, 48, 50, 77, 78, 80, 82, 85, 104

C. Hoose, U. Lohmann, R. Erdin, and I. Tegen. The global influence of dust mineralogical composition on heterogeneous ice nucleation in mixed-phase clouds. *Environmental Research Letters*, 3(2):025003, April 2008. doi: 10.1088/1748-9326/3/2/025003. URL http://iopscience.iop.org/1748-9326/3/2/025003/. → pages 23, 48, 108

C. Hoose, J. E. Kristjánsson, and S. M. Burrows. How important is biological ice nucleation in clouds on a global scale? *Environmental Research Letters*, 5(2):024009, April 2010a. doi: 10.1088/1748-9326/5/2/024009. URL http://iopscience.iop.org/1748-9326/5/2/024009/. → pages 5, 22, 48, 63, 85, 107, 108

C. Hoose, J. E. Kristjánsson, J.-P. Chen, and A. Hazra. A classical-theory-based parameterization of heterogeneous ice nucleation by mineral dust, soot, and biological particles in a global climate model. *Journal of the Atmospheric Sciences*, 67(8):2483–2503, August 2010b. doi: 10.1175/2010JAS3425.1. URL http://journals.ametsoc.org/doi/abs/10.1175/2010JAS3425.1. → pages 22, 48, 63, 85, 107

J.T. Houghton, Y. Ding, D.J. Griggs, M. Noguer, P.J. van der Linden, X. Dai, K. Maskell, and C.A. Johnson, editors. *Climate Change 2001: The scientific basis. Contribution of Working*

Group I to the Third Assessment Report of the Intergovernmental Panel on Climate Change. Cambridge University Press, United Kingdom and New York, NY, USA, 2001. → pages 21

C. R. Hoyle, V. Pinti, A. Welti, B. Zobrist, C. Marcolli, B. Luo, Á. Höskuldsson, H. B. Mattsson, O. Stetzer, T. Thorsteinsson, G. Larsen, and T. Peter. Ice nucleation properties of volcanic ash from Eyjafjallajökull. *Atmospheric Chemistry and Physics*, 11(18): 9911–9926, September 2011. doi: 10.5194/acp-11-9911-2011. URL http://www.atmos-chem-phys.net/11/9911/2011/. → pages 50, 60

X. L. Hu and A. Michaelides. Ice formation on kaolinite: Lattice match or amphoterism? *Surface Science*, 601(23):5378–5381, December 2007. doi: 10.1016/j.susc.2007.09.012. URL http://linkinghub.elsevier.com/retrieve/pii/S0039602807008692. → pages 43

J. A. Huffman, A. J. Prenni, P. J. DeMott, C. Pöhlker, R. H. Mason, N. H. Robinson, J. Fröhlich-Nowoisky, Y. Tobo, V. R. Després, E. Garcia, D. J. Gochis, E. Harris, I. Müller-Germann, C. Ruzene, B. Schmer, B. Sinha, D. A. Day, M. O. Andreae, J. L. Jimenez, M. Gallagher, S. M. Kreidenweis, A. K. Bertram, and U. Pöschl. High concentrations of biological aerosol particles and ice nuclei during and after rain. *Atmospheric Chemistry and Physics*, 13(13):6151–6164, July 2013. doi: 10.5194/acp-13-6151-2013. URL http://www.atmos-chem-phys.net/13/6151/2013/. → pages 8, 85

H.-M. Hung, A. Malinowski, and S. T. Martin. Kinetics of heterogeneous ice nucleation on the surfaces of mineral dust cores inserted into aqueous ammonium sulfate particles. *The Journal of Physical Chemistry A*, 107(9):1296–1306, March 2003. doi: 10.1021/jp021593y. URL http://pubs.acs.org/doi/abs/10.1021/jp021593y. → pages 22, 45, 105

R. Iannone, D. I. Chernoff, A. Pringle, S. T. Martin, and A. K. Bertram. The ice nucleation ability of one of the most abundant types of fungal spores found in the atmosphere. *Atmospheric Chemistry and Physics*, 11(3):1191–1201, February 2011. doi: 10.5194/acp-11-1191-2011. URL http://www.atmos-chem-phys.net/11/1191/2011/. → pages xx, 51, 56, 89, 90, 91, 95

L. Ickes, A. Welti, C. Hoose, and U. Lohmann. Classical nucleation theory of homogeneous freezing of water: thermodynamic and kinetic parameters. *Phys. Chem. Chem. Phys.*, 17 (8):5514–5537, 2015. ISSN 1463-9076. doi: 10.1039/C4CP04184D. URL http://xlink.rsc.org/?DOI=C4CP04184D. → pages 106

K. Isono. On ice-crystal nuclei and other substances found in snow crystals. *Journal of Meteorology*, 12:456–462, 1955. doi: 10.1175/1520-0469(1955)012⟨0456:OICNAO⟩2.0.CO;2. → pages 7

K. Isono, M. Komabayasi, and A. Ono. The nature and origin of ice nuclei in the atmosphere. *Journal of the Meteorological Society of Japan*, 37(6):211–233, 1959. URL http://scholar.google.com/scholar?hl=en&btnG=Search&q=intitle:The+Nature+and+the+Origin+of+Ice+Nuclei+in+the+Atmosphere#0. → pages 7, 48

D. J. Jacob. *Introduction to atmospheric chemistry*. Princeton University Press, Princeton, NJ, 1999. → pages 9, 11

R. Jaenicke. Abundance of cellular material and proteins in the atmosphere. *Science (New York, N.Y.)*, 308(5718):73, April 2005. doi: 10.1126/science.1106335. URL http://www.ncbi.nlm.nih.gov/pubmed/15802596. → pages 3

K. Jayaweera and P. Flanagan. Investigations on biogenic ice nuclei in the Arctic atmosphere. *Geophysical Research Letters*, 9(1):94–97, January 1982. doi: 10.1029/GL009i001p00094. URL http://doi.wiley.com/10.1029/GL009i001p00094. → pages 8, 85

E. J. Jensen and O. B. Toon. The potential impact of soot particles from aircraft exhaust on cirrus clouds. *Geophysical Research Letters*, 24(3):249–252, 1997. doi: 10.1029/96GL03235. URL http://www.agu.org/pubs/crossref/1997/96GL03235.shtml. → pages 22, 63, 107

E. J. Jensen, O. B. Toon, D. L. Westphal, S. Kinne, and A. J. Heymsfield. Microphysical modeling of cirrus: 1. Comparison with 1986 FIRE IFO measurements. *Journal of Geophysical Research: Atmospheres*, 99(D5):10421–10442, 1994. doi: 10.1029/93JD02334. URL http://doi.wiley.com/10.1029/93JD02334. → pages 63

E. J. Jensen, O. B. Toon, R. F. Pueschel, J. Goodman, G. W. Sachse, B. E. Anderson, K. R. Chan, D. Baumgardner, and R. C. Miake-Lye. Ice crystal nucleation and growth in contrails forming at low ambient temperatures. *Geophysical Research Letters*, 25(9):1371–1374, 1998. doi: 10.1029/97GL03592. URL http://www.agu.org/pubs/crossref/1998/97GL03592.shtml. → pages 22, 63, 107

Z. A. Kanji and J. P. D. Abbatt. Ice nucleation onto Arizona test dust at cirrus temperatures: Effect of temperature and aerosol size on onset relative humidity. *The Journal of Physical Chemistry A*, 114(2):935–941, January 2010. doi: 10.1021/jp908661m. URL http://pubs.acs.org/doi/abs/10.1021/jp908661m. → pages 33, 51

Z. A. Kanji, O. Florea, and J. P. D. Abbatt. Ice formation via deposition nucleation on mineral dust and organics: Dependence of onset relative humidity on total particulate surface area. *Environmental Research Letters*, 3(2):025004, April 2008. doi: 10.1088/1748-9326/3/2/025004. URL http://stacks.iop.org/1748-9326/3/i=2/a=025004?key=crossref.0411a868f7543ea0bb122b2fdafa23ce. → pages 32, 103

Z. A. Kanji, P. J. DeMott, O. Möhler, and J. P. D. Abbatt. Results from the University of Toronto continuous flow diffusion chamber at ICIS 2007: instrument intercomparison and ice onsets for different aerosol types. *Atmospheric Chemistry and Physics*, 11(1):31–41, January 2011. doi: 10.5194/acp-11-31-2011. URL http://www.atmos-chem-phys.net/11/31/2011/. → pages

B. Kärcher. Aircraft-generated aerosols and visible contrails. *Geophysical Research Letters*, 23(15):1933–1936, 1996. doi: 10.1029/96GL01853. URL http://www.agu.org/pubs/crossref/1996/96GL01853.shtml. → pages 22, 63, 107

B. Kärcher. Physicochemistry of aircraft-generated liquid aerosols, soot, and ice particles 1. Model description. *Journal of Geophysical Research: Atmospheres*, 103(D14): 17111–17128, 1998. doi: 10.1029/98JD01044. URL http://www.agu.org/pubs/crossref/1998/98JD01044.shtml. → pages 22, 63, 107

B. Kärcher and U. Lohmann. A parameterization of cirrus cloud formation: Heterogeneous freezing. *Journal of Geophysical Research*, 108(D14), 2003. doi: 10.1029/2002JD003220. URL http://www.agu.org/pubs/crossref/2003/2002JD003220.shtml. → pages 12

B. Kärcher, R. Busen, A. Petzold, F. P. Schröder, U. Schumann, and E. J. Jensen. Physicochemistry of aircraft-generated liquid aerosols, soot, and ice particles: 2. Comparison with observations and sensitivity studies. *Journal of Geophysical Research: Atmospheres*, 103(D14):17129–17147, July 1998. doi: 10.1029/98JD01045. URL http://www.agu.org/pubs/crossref/1998/98JD01045.shtml. → pages 22, 63, 107

V. I. Khvorostyanov and J. A. Curry. A new theory of heterogeneous ice nucleation for application in cloud and climate models. *Geophysical Research Letters*, 27(24):4081–4084, 2000. doi: 10.1029/1999GL011211. URL http://www.agu.org/pubs/crossref/2000/1999GL011211.shtml. → pages 23, 63, 107

V. I. Khvorostyanov and J. A. Curry. The theory of ice nucleation by heterogeneous freezing of deliquescent mixed CCN. Part I: Critical radius, energy, and nucleation rate. *Journal of the Atmospheric Sciences*, 61(22):2676–2691, November 2004. doi: 10.1175/JAS3266.1. URL http://journals.ametsoc.org/doi/abs/10.1175/JAS3266.1. → pages 23, 63, 107

V. I. Khvorostyanov and J. A. Curry. The theory of ice nucleation by heterogeneous freezing of deliquescent mixed CCN. Part II: Parcel model simulation. *Journal of the Atmospheric Sciences*, 62(2):261–285, February 2005. doi: 10.1175/JAS-3367.1. URL http://journals.ametsoc.org/doi/abs/10.1175/JAS-3367.1. → pages 23, 63, 107

V. I. Khvorostyanov and J. A. Curry. Critical humidities of homogeneous and heterogeneous ice nucleation: Inferences from extended classical nucleation theory. *Journal of Geophysical Research: Atmospheres*, 114(D4):D04207, February 2009. doi: 10.1029/2008JD011197. URL http://www.agu.org/pubs/crossref/2009/2008JD011197.shtml. → pages 23, 63, 107

H. Klein, S. Nickovic, W. Haunold, U. Bundke, B. Nillius, M. Ebert, S. Weinbruch, L. Schuetz, Z. Levin, L. A. Barrie, and H. Bingemer. Saharan dust and ice nuclei over Central Europe. *Atmospheric Chemistry and Physics*, 10(21):10211–10221, November 2010. doi: 10.5194/acp-10-10211-2010. URL http://www.atmos-chem-phys.net/10/10211/2010/. → pages 7, 23

D. A. Knopf and T. Koop. Heterogeneous nucleation of ice on surrogates of mineral dust. *Journal of Geophysical Research: Atmospheres*, 111(D12):D12201, 2006. doi: 10.1029/2005JD006894. URL http://www.agu.org/pubs/crossref/2006/2005JD006894.shtml. → pages 48, 51, 79

K. A. Koehler, S. M. Kreidenweis, P. J. DeMott, M. D. Petters, A. J. Prenni, and O. Möhler. Laboratory investigations of the impact of mineral dust aerosol on cold cloud formation. *Atmospheric Chemistry and Physics*, 10(23):11955–11968, December 2010. doi: 10.5194/acp-10-11955-2010. URL http://www.atmos-chem-phys.net/10/11955/2010/. → pages 23, 51, 52

T. Koop and B. Zobrist. Parameterizations for ice nucleation in biological and atmospheric systems. *Physical Chemistry Chemical Physics*, 11(46):10839–10850, December 2009. doi: 10.1039/b914289d. URL http://pubs.rsc.org/en/Content/ArticleLanding/2009/CP/b914289d. → pages 51

T. Koop, A. Kapilashrami, L. T. Molina, and M. J. Molina. Phase transitions of sea-salt/water mixtures at low temperatures: Implications for ozone chemistry in the polar marine boundary layer. *Journal of Geophysical Research: Atmospheres*, 105(D21):26393–26402, November 2000. doi: 10.1029/2000JD900413. URL http://doi.wiley.com/10.1029/2000JD900413. → pages 51

G. Kulkarni and S. Dobbie. Ice nucleation properties of mineral dust particles: Determination of onset RHi, IN active fraction, nucleation time-lag, and the effect of active sites on contact angles. *Atmospheric Chemistry and Physics*, 10(1):95–105, January 2010. doi: 10.5194/acp-10-95-2010. URL http://www.atmos-chem-phys.net/10/95/2010/. → pages 23

G. Kulkarni, J. Fan, J. M. Comstock, X. Liu, and M. Ovchinnikov. Laboratory measurements and model sensitivity studies of dust deposition ice nucleation. *Atmospheric Chemistry and Physics*, 12(16):7295–7308, August 2012. doi: 10.5194/acp-12-7295-2012. URL http://www.atmos-chem-phys.net/12/7295/2012/. → pages 48, 63, 65, 68, 85, 107

M. Kumai. Snow crystals and the identification of the nuclei in the Northern United States of America. *Journal of Meteorology*, 18(2):139–150, April 1961. doi: 10.1175/1520-0469(1961)018⟨0139:SCATIO⟩2.0.CO;2. URL http://www.osti.gov/energycitations/product.biblio.jsp?osti_id=6918489http://journals.ametsoc.org/doi/abs/10.1175/1520-0469(1961)018⟨0139:SCATIO⟩2.0.CO;2. → pages 7, 48

M. Kumai and K. E. Francis. Nuclei in Snow and Ice Crystals on the Greenland Ice Cap under Natural and Artificially Stimulated Conditions. *Journal of the Atmospheric Sciences*, 19(6): 474–481, November 1962. doi: 10.1175/1520-0469(1962)019⟨0474:NISAIC⟩2.0.CO;2. URL http://journals.ametsoc.org/doi/abs/10.1175/1520-0469(1962)019⟨0474:NISAIC⟩2.0.CO;2. → pages 7

R. Li and Q.-L. Min. Impacts of mineral dust on the vertical structure of precipitation. *Journal of Geophysical Research*, 115(D9):D09203, May 2010. doi: 10.1029/2009JD011925. URL http://www.agu.org/pubs/crossref/2010/2009JD011925.shtml. → pages 7, 23

D. R. Lide, editor. *CRC Handbook of Chemistry and Physics*. CRC Press LLC, 82 edition, 2001. → pages xiv, 18, 37

J. Lindemann, H. A. Constantinidou, W. R. Barecht, and C. D. Upper. Plants as sources of airborne bacteria, including ice nucleation-active bacteria. *Applied and Environmental Microbiology*, 44(5):1059, 1982. URL http://aem.asm.org/content/44/5/1059.short. → pages 8, 85

X. Liu, J. E. Penner, S. J. Ghan, and M. Wang. Inclusion of ice microphysics in the NCAR Community Atmospheric Model Version 3 (CAM3). *Journal of Climate*, 20(18): 4526–4547, September 2007. doi: 10.1175/JCLI4264.1. URL http://journals.ametsoc.org/doi/abs/10.1175/JCLI4264.1. → pages 63, 107

U. Lohmann. A glaciation indirect aerosol effect caused by soot aerosols. *Geophysical Research Letters*, 29(4), 2002. doi: 10.1029/2001GL014357. URL http://www.agu.org/pubs/crossref/2002/2001GL014357.shtml. → pages 11

U. Lohmann and K. Diehl. Sensitivity studies of the importance of dust ice nuclei for the indirect aerosol effect on stratiform mixed-phase clouds. *Journal of the Atmospheric Sciences*, 63(3):968–982, March 2006. doi: 10.1175/JAS3662.1. URL http://journals.ametsoc.org/doi/abs/10.1175/JAS3662.1. → pages 48, 84

U. Lohmann and J. Feichter. Global indirect aerosol effects: A review. *Atmospheric Chemistry and Physics*, 5(3):715–737, March 2005. doi: 10.5194/acp-5-715-2005. URL http://www.atmos-chem-phys.net/5/715/2005/. → pages 10, 47, 84

F. Lüönd, O. Stetzer, A. Welti, and U. Lohmann. Experimental study on the ice nucleation ability of size-selected kaolinite particles in the immersion mode. *Journal of Geophysical Research*, 115(D14):D14201, July 2010. doi: 10.1029/2009JD012959. URL http://www.agu.org/pubs/crossref/2010/2009JD012959.shtml. → pages 13, 22, 23, 38, 39, 40, 42, 43, 44, 45, 48, 49, 50, 60, 65, 66, 67, 68, 72, 76, 79, 86, 91, 101, 105

L. R. Maki and E. L. Galyan. Ice nucleation induced by Pseudomonas syringae. *Applied and Environmental Microbiology*, 28(3):456–459, 1974. URL http://aem.asm.org/content/28/3/456.short. → pages 9

L. R. Maki and K. J. Willoughby. Bacteria as biogenic sources of freezing nuclei. *Journal of Applied Meteorology*, 17(7):1049–1053, July 1978. doi: 10.1175/1520-0450(1978)017⟨1049:BABSOF⟩2.0.CO;2. URL http://journals.ametsoc.org/doi/abs/10.1175/1520-0450%281978%29017%3C1049%3ABABSOF%3E2.0.CO%3B2. → pages 9, 85

C. Marcolli. Deposition nucleation viewed as homogeneous or immersion freezing in pores and cavities. *Atmospheric Chemistry and Physics*, 14(4):2071–2104, February 2014. doi: 10.5194/acp-14-2071-2014. URL http://www.atmos-chem-phys.net/14/2071/2014/. → pages 107

C. Marcolli, S. Gedamke, T. Peter, and B. Zobrist. Efficiency of immersion mode ice nucleation on surrogates of mineral dust. *Atmospheric Chemistry and Physics*, 7(19): 5081–5091, October 2007. doi: 10.5194/acp-7-5081-2007. URL http://www.atmos-chem-phys.net/7/5081/2007/. → pages 13, 22, 23, 38, 39, 42, 45, 48, 49, 51, 65, 72, 76, 79, 80, 86, 101, 105

H. Maring, D. K. Savoie, M. A. Izaguirre, L. Custals, and J. S. Reid. Mineral dust aerosol size distribution change during atmospheric transport. *Journal of Geophysical Research: Atmospheres*, 108(D19):8592, 2003. doi: 10.1029/2002JD002536. URL http://doi.wiley.com/10.1029/2002JD002536. → pages 82, 104

S. T. Martin, J. H. Han, and H. M. Hung. The size effect of hematite and corundum inclusions on the efflorescence relative humidities of aqueous ammonium sulfate particles. *Geophysical Research Letters*, 28(13):2601–2604, 2001. URL http://www.seas.harvard.edu/environmental-chemistry/publications/SizeEffectGRL.pdf. → pages 23

Q.-L. Min, R. Li, B. Lin, E. Joseph, S. Wang, Y. Hu, V. Morris, and F. Chang. Evidence of mineral dust altering cloud microphysics and precipitation. *Atmospheric Chemistry and Physics*, 9(9):3223–3231, May 2009. doi: 10.5194/acp-9-3223-2009. URL http://www.atmos-chem-phys.net/9/3223/2009/. → pages 7, 23

O. Möhler, P. J. DeMott, G. Vali, and Z. Levin. Microbiology and atmospheric processes: the role of biological particles in cloud physics. *Biogeosciences*, 4(6):1059–1071, December 2007. doi: 10.5194/bg-4-1059-2007. URL http://www.biogeosciences.net/4/1059/2007/. → pages 9

O. Möhler, S. Benz, H. Saathoff, M. Schnaiter, R. Wagner, J. Schneider, S. Walter, V. Ebert, and S. Wagner. The effect of organic coating on the heterogeneous ice nucleation efficiency of mineral dust aerosols. *Environmental Research Letters*, 3(2):025007, April 2008a. doi: 10.1088/1748-9326/3/2/025007. URL http://stacks.iop.org/1748-9326/3/i=2/a=025007?key=crossref.d9430010506fa5292539821f7ee92ca3. → pages 32, 103

O. Möhler, D. G. Georgakopoulos, C. E. Morris, S. Benz, V. Ebert, S. Hunsmann, H. Saathoff, M. Schnaiter, and R. Wagner. Heterogeneous ice nucleation activity of bacteria: New laboratory experiments at simulated cloud conditions. *Biogeosciences*, 5(5):1425–1435, October 2008b. doi: 10.5194/bg-5-1425-2008. URL http://www.biogeosciences.net/5/1425/2008/. → pages 89

O. Möhler, J. Schneider, S. Walter, A. J. Heymsfield, C. Schmitt, and Z. J. Ulanowski. How coating layers influence the deposition mode ice nucleation on mineral particles. In *15th Int. Conf. Clouds and Precipitation*, Cancun, Mexico, 2008c. → pages 32, 103

C. E. Morris, D. C. Sands, B. A. Vinatzer, C. Glaux, C. Guilbaud, A. Buffière, S. Yan, H. Dominguez, and B. M. Thompson. The life history of the plant pathogen Pseudomonas

syringae is linked to the water cycle. *The ISME journal*, 2(3):321–34, March 2008. doi: 10.1038/ismej.2007.113. URL http://www.ncbi.nlm.nih.gov/pubmed/18185595. → pages 9, 85

H. Morrison, J. A. Curry, and V. I. Khvorostyanov. A new double-moment microphysics parameterization for application in cloud and climate models. Part I: Description. *Journal of the Atmospheric Sciences*, 62(6):1665–1677, June 2005. doi: 10.1175/JAS3446.1. URL http://journals.ametsoc.org/doi/abs/10.1175/JAS3446.1. → pages 22, 63, 107

J. W. Mullin. *Crystallization*. Butterworth-Heinemann, Oxford, UK, 4th ed edition, 2001. ISBN 0750648333. → pages 16

B. J. Murray and A. K. Bertram. Formation and stability of cubic ice in water droplets. *Physical Chemistry Chemical Physics*, 8(1):186–92, January 2006. doi: 10.1039/b513480c. URL http://www.ncbi.nlm.nih.gov/pubmed/16482260. → pages 37

B. J. Murray, D. A. Knopf, and A. K. Bertram. The formation of cubic ice under conditions relevant to Earth's atmosphere. *Nature*, 434(7030):202–5, March 2005. doi: 10.1038/nature03403. URL http://www.ncbi.nlm.nih.gov/pubmed/15758996. → pages 37

B. J. Murray, S. L. Broadley, T. W. Wilson, J. D. Atkinson, and R. H. Wills. Heterogeneous freezing of water droplets containing kaolinite particles. *Atmospheric Chemistry and Physics*, 11(9):4191–4207, May 2011. doi: 10.5194/acp-11-4191-2011. URL http://www.atmos-chem-phys.net/11/4191/2011/. → pages 15, 23, 45, 48, 49, 50, 60, 68, 73, 74, 75, 76, 79, 80, 86

B. J. Murray, D. O'Sullivan, J. D. Atkinson, and M. E. Webb. Ice nucleation by particles immersed in supercooled cloud droplets. *Chemical Society Reviews*, 41(19):6519–6554, October 2012. doi: 10.1039/c2cs35200a. URL http://www.ncbi.nlm.nih.gov/pubmed/22932664. → pages xiii, 3, 8, 16, 77, 84, 85

D. Niedermeier, S. Hartmann, R. A. Shaw, D. Covert, T. F. Mentel, J. Schneider, L. Poulain, P. Reitz, C. Spindler, T. Clauss, A. Kiselev, E. Hallbauer, H. Wex, K. Mildenberger, and F. Stratmann. Heterogeneous freezing of droplets with immersed mineral dust particles - measurements and parameterization. *Atmospheric Chemistry and Physics*, 10(8): 3601–3614, April 2010. doi: 10.5194/acp-10-3601-2010. URL http://www.atmos-chem-phys.net/10/3601/2010/. → pages 23, 48, 49, 51, 60, 68, 75, 76, 79, 86

D. Niedermeier, S. Hartmann, T. Clauss, H. Wex, A. Kiselev, R. C. Sullivan, P. J. DeMott, M. D. Petters, P. Reitz, J. Schneider, E. Mikhailov, B. Sierau, O. Stetzer, B. Reimann, U. Bundke, R. A. Shaw, A. Buchholz, T. F. Mentel, and F. Stratmann. Experimental study of the role of physicochemical surface processing on the IN ability of mineral dust particles. *Atmospheric Chemistry and Physics*, 11(21):11131–11144, November 2011a. doi: 10.5194/acp-11-11131-2011. URL http://www.atmos-chem-phys.net/11/11131/2011/. → pages 51, 60

D. Niedermeier, R. A. Shaw, S. Hartmann, H. Wex, T. Clauss, J. Voigtländer, and F. Stratmann. Heterogeneous ice nucleation: Exploring the transition from stochastic to singular freezing behavior. *Atmospheric Chemistry and Physics*, 11(16):8767–8775, August 2011b. doi: 10.5194/acp-11-8767-2011. URL http://www.atmos-chem-phys.net/11/8767/2011/. → pages xi, 13, 23, 39, 49, 66, 76, 91

D. Niedermeier, B. Ervens, T. Clauss, J. Voigtländer, H. Wex, S. Hartmann, and F. Stratmann. A computationally efficient description of heterogeneous freezing: A simplified version of the Soccer ball model. *Geophysical Research Letters*, 41(2):736–741, January 2014. doi: 10.1002/2013GL058684. URL http://doi.wiley.com/10.1002/2013GL058684. → pages 13, 92, 106

M. Niemand, O. Möhler, B. Vogel, H. Vogel, C. Hoose, P. Connolly, H. Klein, H. Bingemer, P. DeMott, J. Skrotzki, and T. Leisner. A particle-surface-area-based parameterization of immersion freezing on desert dust particles. *Journal of the Atmospheric Sciences*, 69(10): 3077–3092, October 2012. doi: 10.1175/JAS-D-11-0249.1. URL http://journals.ametsoc.org/doi/abs/10.1175/JAS-D-11-0249.1. → pages 13, 51, 77, 79

M. T. Parsons, J. Mak, S. R. Lipetz, and A. K. Bertram. Deliquescence of malonic, succinic, glutaric, and adipic acid particles. *Journal of Geophysical Research*, 109(D6):D06212, 2004. doi: 10.1029/2003JD004075. URL http://www.agu.org/pubs/crossref/2004/2003JD004075.shtml. → pages 24

V. T. J. Phillips, P. J. DeMott, and C. Andronache. An empirical parameterization of heterogeneous ice nucleation for multiple chemical species of aerosol. *Journal of the Atmospheric Sciences*, 65(9):2757–2783, September 2008. doi: 10.1175/2007JAS2546.1. URL http://journals.ametsoc.org/doi/abs/10.1175/2007JAS2546.1. → pages 5, 13, 85, 86

V. T. J. Phillips, C. Andronache, B. Christner, C. E. Morris, D. C. Sands, A. Bansemer, A. Lauer, C. McNaughton, and C. Seman. Potential impacts from biological aerosols on ensembles of continental clouds simulated numerically. *Biogeosciences*, 6(6):987–1014,

June 2009. doi: 10.5194/bg-6-987-2009. URL http://www.biogeosciences.net/6/987/2009/. → pages 13

V. Pinti, C. Marcolli, B. Zobrist, C. R. Hoyle, and T. Peter. Ice nucleation efficiency of clay minerals in the immersion mode. *Atmospheric Chemistry and Physics*, 12(13):5859–5878, July 2012. doi: 10.5194/acp-12-5859-2012. URL http://www.atmos-chem-phys.net/12/5859/2012/. → pages 48, 50, 79, 80

R. L. Pitter and H. R. Pruppacher. A wind tunnel investigation of freezing of small water drops falling at terminal velocity in air. *Quarterly Journal of the Royal Meteorological Society*, 99(421):540–550, July 1973. doi: 10.1002/qj.49709942111. URL http://doi.wiley.com/10.1002/qj.49709942111. → pages 50, 60

K. A. Pratt, P. J. DeMott, J. R. French, Z. Wang, D. L. Westphal, A. J. Heymsfield, C. H. Twohy, A. J. Prenni, and K. A. Prather. In situ detection of biological particles in cloud ice-crystals. *Nature Geoscience*, 2(6):398–401, May 2009. doi: 10.1038/ngeo521. URL http://www.nature.com/doifinder/10.1038/ngeo521. → pages 9, 85

A. J. Prenni, M. D. Petters, S. M. Kreidenweis, C. L. Heald, S. T. Martin, P. Artaxo, R. M. Garland, A. G. Wollny, and U. Pöschl. Relative roles of biogenic emissions and Saharan dust as ice nuclei in the Amazon basin. *Nature Geoscience*, 2(6):402–405, May 2009. doi: 10.1038/ngeo517. URL http://www.nature.com/doifinder/10.1038/ngeo517. → pages 7, 9, 23, 48, 85

A. J. Prenni, Y. Tobo, E. Garcia, P. J. DeMott, J. A. Huffman, C. S. McCluskey, S. M. Kreidenweis, J. E. Prenni, C. Pöhlker, and U. Pöschl. The impact of rain on ice nuclei populations at a forested site in Colorado. *Geophysical Research Letters*, 40(1):227–231, January 2013. doi: 10.1029/2012GL053953. URL http://doi.wiley.com/10.1029/2012GL053953. → pages 9, 85

H. R. Pruppacher and J. D. Klett. *Microphysics of clouds and precipitation*. Kluwer Academic Publishers, Dordrecht, 2nd edition, 1997. ISBN 0-7923-4211-9. → pages xiv, 6, 7, 8, 11, 18, 20, 22, 33, 36, 37, 48, 49, 56, 63, 64

W. S. Rasband. ImageJ, 1997-2014. URL http://imagej.nih.gov/ij/. → pages 55

P. C. Reist. *Aerosol science and technology*. McGraw-Hill, Inc., 2nd edn. edition, 1992. → pages 29

P. Reitz, C. Spindler, T. F. Mentel, L. Poulain, H. Wex, K. Mildenberger, D. Niedermeier, S. Hartmann, T. Clauss, F. Stratmann, R. C. Sullivan, P. J. DeMott, M. D. Petters, B. Sierau,

and J. Schneider. Surface modification of mineral dust particles by sulphuric acid processing: implications for ice nucleation abilities. *Atmospheric Chemistry and Physics*, 11(15):7839–7858, August 2011. doi: 10.5194/acp-11-7839-2011. URL http://www.atmos-chem-phys.net/11/7839/2011/. → pages 51

M. S. Richardson, P. J. DeMott, S. M. Kreidenweis, D. J. Cziczo, E. J. Dunlea, J. L. Jimenez, D. S. Thomson, L. L. Ashbaugh, R. D. Borys, D. L. Westphal, G. S. Casuccio, and T. L. Lersch. Measurements of heterogeneous ice nuclei in the western United States in springtime and their relation to aerosol characteristics. *Journal of Geophysical Research: Atmospheres*, 112(D2):D02209, January 2007. doi: 10.1029/2006JD007500. URL http://www.agu.org/pubs/crossref/2007/2006JD007500.shtml. → pages 7, 48

P. Roberts and J. Hallett. A laboratory study of the ice nucleating properties of some mineral particulates. *Quarterly Journal of the Royal Meteorological Society*, 94(399):25–34, January 1968. doi: 10.1002/qj.49709439904. URL http://doi.wiley.com/10.1002/qj.49709439904. → pages 48, 50, 79

A. Salam, U. Lohmann, B. Crenna, G. Lesins, P. Klages, D. Rogers, R. Irani, A. MacGillivray, and M. Coffin. Ice nucleation studies of mineral dust particles with a new continuous flow diffusion chamber. *Aerosol Science and Technology*, 40(2):134–143, February 2006. doi: 10.1080/02786820500444853. URL http://www.informaworld.com/openurl?genre=article&doi=10.1080/02786820500444853&magic=crossref||D404A21C5BB053405B1A640AFFD44AE3http://www.tandfonline.com/doi/abs/10.1080/02786820500444853. → pages 32, 103

K. Sassen. Indirect climate forcing over the western US from Asian dust storms. *Geophysical Research Letters*, 29(10):2–5, 2002. doi: 10.1029/2001GL014051. URL http://www.agu.org/pubs/crossref/2002/2001GL014051.shtml. → pages 7, 23

K. Sassen, P. J. DeMott, J. M. Prospero, and M. R. Poellot. Saharan dust storms and indirect aerosol effects on clouds: CRYSTAL-FACE results. *Geophysical Research Letters*, 30(12):1633, 2003. doi: 10.1029/2003GL017371. URL http://www.agu.org/pubs/crossref/2003/2003GL017371.shtml. → pages 7, 23, 48

R. W. Saunders, O. Möhler, M. Schnaiter, S. Benz, R. Wagner, H. Saathoff, P. J. Connolly, R. Burgess, B. J. Murray, M. Gallagher, R. Wills, and J. M. C. Plane. An aerosol chamber investigation of the heterogeneous ice nucleating potential of refractory nanoparticles. *Atmospheric Chemistry and Physics*, 10(3):1227–1247, February 2010. doi:

10.5194/acp-10-1227-2010. URL http://www.atmos-chem-phys.net/10/1227/2010/. → pages 23

P. Seifert, A. Ansmann, I. Mattis, U. Wandinger, M. Tesche, R. Engelmann, D. Müller, C. Pérez, and K. Haustein. Saharan dust and heterogeneous ice formation: Eleven years of cloud observations at a central European EARLINET site. *Journal of Geophysical Research: Atmospheres*, 115(D20):D20201, October 2010. doi: 10.1029/2009JD013222. URL http://www.agu.org/pubs/crossref/2010/2009JD013222.shtml. → pages 7, 23, 48

J. H. Seinfeld and S. N. Pandis. *Atmospheric chemistry and physics: From air pollution to climate change*. John Wiley & Sons, Inc., Hoboken, New Jersey, 2 edition, 2006. ISBN 978-0-471-72017-1. → pages 1, 9, 11, 17

A. Sesartic, U. Lohmann, and T. Storelvmo. Bacteria in the ECHAM5-HAM global climate model. *Atmospheric Chemistry and Physics*, 12(18):8645–8661, September 2012. doi: 10.5194/acp-12-8645-2012. URL http://www.atmos-chem-phys.net/12/8645/2012/. → pages 85

A. Sesartic, U. Lohmann, and T. Storelvmo. Modelling the impact of fungal spore ice nuclei on clouds and precipitation. *Environmental Research Letters*, 8(1):014029, March 2013. doi: 10.1088/1748-9326/8/1/014029. URL http://stacks.iop.org/1748-9326/8/i=1/a=014029?key=crossref.88a72028f40efa4d07daaef5c00b97b5. → pages 85

R. A. Shaw, A. J. Durant, and Y. Mi. Heterogeneous surface crystallization observed in undercooled water. *The Journal of Physical Chemistry B*, 109(20):9865–8, May 2005. doi: 10.1021/jp0506336. URL http://www.ncbi.nlm.nih.gov/pubmed/16852192. → pages 15

R. C. Sullivan, M. D. Petters, P. J. DeMott, S. M. Kreidenweis, H. Wex, D. Niedermeier, S. Hartmann, T. Clauss, F. Stratmann, P. Reitz, J. Schneider, and B. Sierau. Irreversible loss of ice nucleation active sites in mineral dust particles caused by sulphuric acid condensation. *Atmospheric Chemistry and Physics*, 10(23):11471–11487, December 2010. doi: 10.5194/acp-10-11471-2010. URL http://www.atmos-chem-phys.net/10/11471/2010/. → pages 79

T. Y. Tanaka and M. Chiba. A numerical study of the contributions of dust source regions to the global dust budget. *Global and Planetary Change*, 52:88–104, 2006. doi: 10.1016/j.gloplacha.2006.02.002. → pages 2

A. C. Targino, R. Krejci, K. J. Noone, and P. Glantz. Single particle analysis of ice crystal residuals observed in orographic wave clouds over Scandinavia during INTACC

experiment. *Atmospheric Chemistry and Physics*, 6(7):1977–1990, June 2006. doi: 10.5194/acp-6-1977-2006. URL http://www.atmos-chem-phys.net/6/1977/2006/. → pages 7, 48

Y. Tobo, A. J. Prenni, P. J. DeMott, J. A. Huffman, C. S. McCluskey, G. Tian, C. Pöhlker, U. Pöschl, and S. M. Kreidenweis. Biological aerosol particles as a key determinant of ice nuclei populations in a forest ecosystem. *Journal of Geophysical Research: Atmospheres*, 118(17):10,100–10,110, September 2013. doi: 10.1002/jgrd.50801. URL http://doi.wiley.com/10.1002/jgrd.50801. → pages 86

C. H. Twohy and M. R. Poellot. Chemical characteristics of ice residual nuclei in anvil cirrus clouds: Evidence for homogeneous and heterogeneous ice formation. *Atmospheric Chemistry and Physics*, 5(8):2289–2297, August 2005. doi: 10.5194/acp-5-2289-2005. URL http://www.atmos-chem-phys.net/5/2289/2005/. → pages 7, 23

S. Twomey. Pollution and the planetary albedo. *Atmospheric Environment*, 8(12):1251–1256, December 1974. doi: 10.1016/0004-6981(74)90004-3. URL http://linkinghub.elsevier.com/retrieve/pii/0004698174900043. → pages 10

G. Vali. Quantitative evaluation of experimental results on the heterogeneous freezing nucleation of supercooled liquids. *Journal of the Atmospheric Sciences*, 28(3):402–409, April 1971. doi: 10.1175/1520-0469(1971)028⟨0402:QEOERA⟩2.0.CO;2. URL http://journals.ametsoc.org/doi/abs/10.1175/1520-0469%281971%29028%3C0402%3AQEOERA%3E2.0.CO%3B2. → pages 77

G. Vali. Nucleation terminology. *Journal of Aerosol Science*, 16(6):575–576, 1985. doi: 10.1016/0021-8502(85)90009-6. URL http://linkinghub.elsevier.com/retrieve/pii/0021850285900096. → pages xiii, 5, 6, 22, 48

G. Vali. Freezing rate due to heterogeneous nucleation. *Journal of the Atmospheric Sciences*, 51(13):1843–1856, July 1994. doi: 10.1175/1520-0469(1994)051⟨1843:FRDTHN⟩2.0.CO;2. URL http://adsabs.harvard.edu/abs/1994JAtS...51.1843Vhttp://journals.ametsoc.org/doi/abs/10.1175/1520-0469%281994%29051%3C1843%3AFRDTHN%3E2.0.CO%3B2. → pages 16

G. Vali. Repeatability and randomness in heterogeneous freezing nucleation. *Atmospheric Chemistry and Physics*, 8(16):5017–5031, August 2008. doi: 10.5194/acp-8-5017-2008. URL http://www.atmos-chem-phys.net/8/5017/2008/. → pages 15, 16, 72, 101

G. Vali. Interpretation of freezing nucleation experiments: Singular and stochastic; sites and surfaces. *Atmospheric Chemistry and Physics*, 14(11):5271–5294, June 2014. doi: 10.5194/acp-14-5271-2014. URL http://www.atmos-chem-phys.net/14/5271/2014/. → pages 15, 16, 72, 101

G. Vali and E. J. Stansbury. Time-dependent characteristics of the heterogeneous nucleation of ice. *Canadian Journal of Physics*, 44(3):477–502, March 1966. doi: 10.1139/p66-044. URL http://www.nrcresearchpress.com/doi/abs/10.1139/p66-044. → pages 16

G. Vali, M. Christensen, R. W. Fresh, E. L. Galyan, L. R. Maki, and R. C. Schnell. Biogenic ice nuclei. Part II: Bacterial Sources. *Journal of the Atmospheric Sciences*, 33(8): 1565–1570, August 1976. doi: 10.1175/1520-0469(1976)033⟨1565:BINPIB⟩2.0.CO;2. URL http://journals.ametsoc.org/doi/abs/10.1175/1520-0469%281976%29033%3C1565%3ABINPIB%3E2.0.CO%3B2. → pages 9

B. Vonnegut and M. Baldwin. Repeated nucleation of a supercooled water sample that contains silver iodide particles. *Journal of Climate and Applied Meteorology*, 23(3): 486–490, March 1984. doi: 10.1175/1520-0450(1984)023⟨0486:RNOASW⟩2.0.CO;2. URL http://journals.ametsoc.org/doi/abs/10.1175/1520-0450(1984)023⟨0486:RNOASW⟩2.0.CO;2. → pages 15

Y. Wang and X. Liu. Immersion freezing by natural dust based on a soccer ball model with the Community Atmospheric Model version 5: climate effects. *Environmental Research Letters*, 9(12):124020, 2014. ISSN 1748-9326. doi: 10.1088/1748-9326/9/12/124020. URL http://stacks.iop.org/1748-9326/9/i=12/a=124020?key=crossref.62715e4343d591224296a3de99f05d15. → pages 48, 85, 107

Y. Wang, X. Liu, C. Hoose, and B. Wang. Different contact angle distributions for heterogeneous ice nucleation in the Community Atmospheric Model version 5. *Atmospheric Chemistry and Physics*, 14(19):10411–10430, October 2014. ISSN 1680-7324. doi: 10.5194/acp-14-10411-2014. URL http://www.atmos-chem-phys-discuss.net/14/7141/2014/http://www.atmos-chem-phys.net/14/10411/2014/. → pages 48, 85, 107

A. Welti, F. Lüönd, O. Stetzer, and U. Lohmann. Influence of particle size on the ice nucleating ability of mineral dusts. *Atmospheric Chemistry and Physics*, 9(18):6705–6715, September 2009. doi: 10.5194/acp-9-6705-2009. URL http://www.atmos-chem-phys.net/9/6705/2009/. → pages 28, 32, 45, 50, 51, 79, 103, 105

A. Welti, F. Lüönd, Z. A. Kanji, O. Stetzer, and U. Lohmann. Time dependence of immersion freezing: An experimental study on size selected kaolinite particles. *Atmospheric Chemistry and Physics*, 12(20):9893–9907, October 2012. doi: 10.5194/acp-12-9893-2012. URL http://www.atmos-chem-phys.net/12/9893/2012/. → pages 15, 48, 49, 60, 65, 67, 68, 72, 76, 86, 91, 101

C. D. Westbrook and A. J. Illingworth. Evidence that ice forms primarily in supercooled liquid clouds at temperatures ¿-27C. *Geophysical Research Letters*, 38(May):1–4, 2011. doi: 10.1029/2011GL048021. → pages 7

M. J. Wheeler and A. K. Bertram. Deposition nucleation on mineral dust particles: A case against classical nucleation theory with the assumption of a single contact angle. *Atmospheric Chemistry and Physics*, 12(2):1189–1201, January 2012. doi: 10.5194/acp-12-1189-2012. URL http://www.atmos-chem-phys.net/12/1189/2012/. → pages 48, 49, 51, 65, 72, 75, 76, 86, 101

M. J. Wheeler, D. I. Haga, R. H. Mason, V. E. Irish, M. J. Wagstaff, R. Iannone, and A. K. Bertram. Testing different schemes for describing immersion freezing of water drops containing primary biological aerosol particles. 2015a. → pages

M. J. Wheeler, R. H. Mason, K. Steunenberg, M. J. Wagstaff, C. Chou, and A. K. Bertram. Immersion freezing of supermicron mineral dust particles: Freezing results, testing different schemes for describing ice nucleation results, and ice nucleation active site densities. *Journal of Physical Chemistry A*, 119(19):4358–4372, 2015b. doi: 10.1021/jp507875q. → pages 86, 101

J. Wolberg. *Data analysis using the method of least squares*. Springer-Verlag, Heidelberg, 2006. ISBN 3-540-25674-1. → pages 69, 95

T. P. Wright, M. D. Petters, J. D. Hader, T. Morton, and A. L. Holder. Minimal cooling rate dependence of ice nuclei activity in the immersion mode. *Journal of Geophysical Research: Atmospheres*, 118(18):10,535–10,543, September 2013. doi: 10.1002/jgrd.50810. URL http://doi.wiley.com/10.1002/jgrd.50810. → pages 15, 73, 74

J. D. Yakobi-Hancock, L. A. Ladino, and J. P. D. Abbatt. Feldspar minerals as efficient deposition ice nuclei. *Atmospheric Chemistry and Physics*, 13(22):11175–11185, November 2013. doi: 10.5194/acp-13-11175-2013. URL http://www.atmos-chem-phys.net/13/11175/2013/. → pages 48

F. Zimmermann, M. Ebert, A. Worringen, L. Schütz, and S. Weinbruch. Environmental scanning electron microscopy (ESEM) as a new technique to determine the ice nucleation capability of individual atmospheric aerosol particles. *Atmospheric Environment*, 41(37): 8219–8227, December 2007. doi: 10.1016/j.atmosenv.2007.06.023. URL http://linkinghub.elsevier.com/retrieve/pii/S1352231007005882. → pages 32, 103

F. Zimmermann, S. Weinbruch, L. Schütz, H. Hofmann, M. Ebert, K. Kandler, and A. Worringen. Ice nucleation properties of the most abundant mineral dust phases. *Journal of Geophysical Research*, 113(D23):D23204, December 2008. doi: 10.1029/2008JD010655. URL http://www.agu.org/pubs/crossref/2008/2008JD010655.shtml. → pages 32, 48, 50, 79, 103

B. Zobrist, T. Koop, B. P. Luo, C. Marcolli, and T. Peter. Heterogeneous ice nucleation rate coefficient of water droplets coated by a nonadecanol monolayer. *Journal of Physical Chemistry C*, 111(5):2149–2155, February 2007. doi: 10.1021/jp066080w. URL http://pubs.acs.org/cgi-bin/doilookup/?10.1021/jp066080w. → pages 56, 64

Appendix A

Sensitivity study of the deposition nucleation of kaolinite and illite

We have performed an additional series of calculations to assess the sensitivity of the results in Chapter 3 to the assumption of spherical particles. In Chapter 3 we assumed the surface area of a particle was equal to the geometric surface area (i.e. the particles are spherical). Here we reanalyze the results with the assumption that the surface area equals the geometric surface area multiplied by 50 [Eastwood et al., 2008], as an upper limit to the surface area.

Table A.1: Fit parameters obtained for kaolinite assuming the surface area equals the geometric surface area multiplied by 50. Best fits were obtained by minimizing the weighted sum of squared residuals (WSSR) between the experimental data and the fit function.

Scheme	Parameter	Value	WSSR[a]
single-α	α	12.77°	9.444
pdf-α	μ_α	0°	3.934
	σ_α	26.66°	
active site	b	$1.24 \times 10^8 \mathrm{m}^{-2}$	5.091
	β_1	0.01	
	β_2	0.001	
deterministic	A_1	$4.63 \times 10^4 \mathrm{cm}^{-2}$	0.718
	A_2	-0.8845	

[a] Weighted sum of squared residuals

Table A.2: Fit parameters obtained for illite assuming the surface area equals the geometric surface area multiplied by 50. Best fits were obtained by minimizing the weighted sum of squared residuals (WSSR) between the experimental data and the fit function.

Scheme	Parameter	Value	WSSR[a]
single-α	α	22.19°	9.778
pdf-α	μ_α	29.52°	0.0464
	σ_α	13.0°	
active site	b	$1.44 \times 10^8 \mathrm{m}^{-2}$	0.538
	β_1	0.1305	
	β_2	1.0×10^{-4}	
deterministic	A_1	$3.55 \times 10^4 \mathrm{cm}^{-2}$	0.0190
	A_2	-0.9480	

[a] Weighted sum of squared residuals

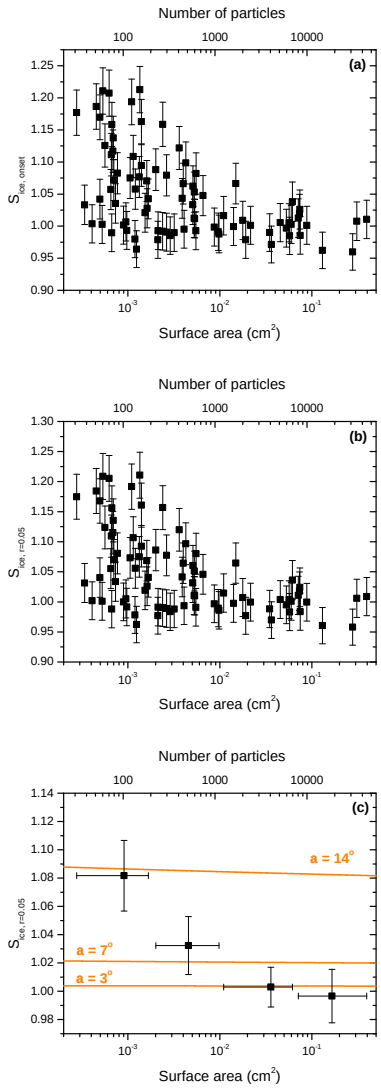

Figure A.1: Results for kaolinite particles: (**a**) individual onset measurements, (**b**) individual $S_{\mathrm{ice,r=0.05}}$ results and (**c**) average $S_{\mathrm{ice,r=0.05}}$. The average values are calculated for four equally sized bins and the horizontal error bars show the range of data points in each bin. The surface area values in (**c**) represent the average surface area of the points in each bin. Error in $S_{\mathrm{ice,onset}}$ is given as experimental error in measurements of saturation. Error in $S_{\mathrm{ice,r=0.05}}$ is based on the difference between $S_{\mathrm{ice,onset}}$ and $S_{\mathrm{ice,previous}}$ as well as the uncertainty in measuring $S_{\mathrm{ice,onset}}$. Error in the average $S_{\mathrm{ice,r=0.05}}$ represents the 95 % confidence interval. Predictions are shown using the single-α scheme (orange lines) calculated using Eq. (3.7). In addition to surface area, the corresponding number of particles calculated from A_{avg} is also shown. The surface area was assumed to be the geometric surface area multiplied by a factor of 50.

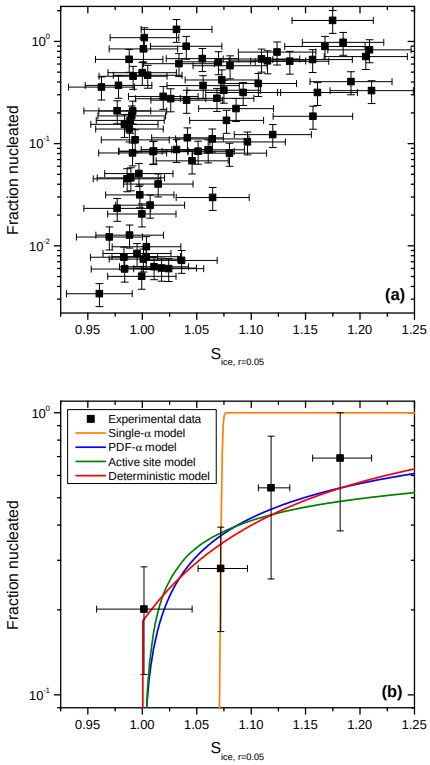

Figure A.2: Fraction of particles nucleated as a function of $S_{\mathrm{ice,r=0.05}}$ for kaolinite. Panel (**a**) shows the nucleated fraction for the individual experimental results. The y-error was calculated from the uncertainty in the value of $\bar{D}_g$. The x-error represents the uncertainty in $S_{\mathrm{ice,r=0.05}}$. Panel (**b**) shows the average nucleated fraction calculated for four size bins. The range of the data points in each bin is given as the horizontal error and data points represent the average of the $S_{\mathrm{ice,r=0.05}}$ values within each bin. The y-error bar in panel (**b**) represents the 95 % confidence interval of the average nucleated fraction. Fits are shown for the single-α, pdf-α, active site, and deterministic schemes. The surface area was assumed to be the geometric surface area multiplied by a factor of 50.

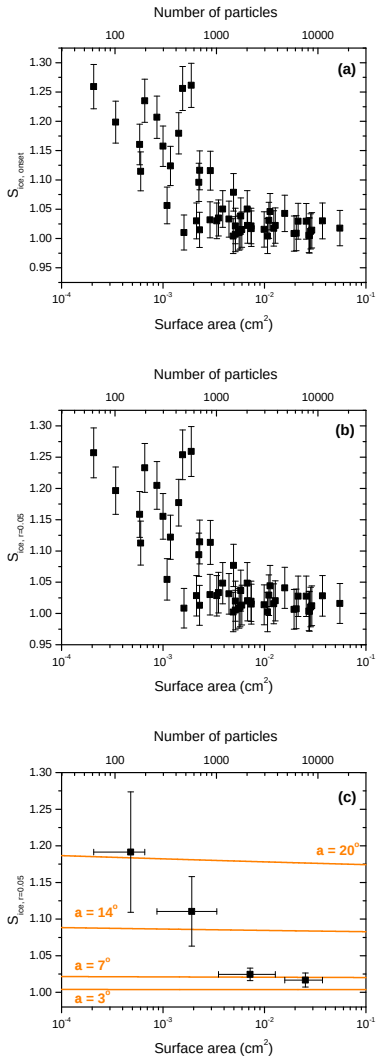

Figure A.3: Results for illite particles: (**a**) individual onset measurements, (**b**) individual $S_{\mathrm{ice,r=0.05}}$ results and (**c**) average $S_{\mathrm{ice,r=0.05}}$. The average values are calculated for four equally sized bins and the horizontal error bars show the range of data points in each bin. The surface area values in (**c**) represent the average surface area of the points in each bin. Error in $S_{\mathrm{ice,onset}}$ is given as experimental error in measurements of saturation. Error in $S_{\mathrm{ice,r=0.05}}$ is based on the difference between $S_{\mathrm{ice,onset}}$ and $S_{\mathrm{ice,previous}}$ as well as the uncertainty in measuring $S_{\mathrm{ice,onset}}$. Error in the average $S_{\mathrm{ice,r=0.05}}$ represents the 95 % confidence interval. Predictions are shown using the single-α scheme (orange lines) calculated using Eq. (3.7). In addition to surface area, the corresponding number of particles calculated from A_{avg} is also shown. The surface area was assumed to be the geometric surface area multiplied by a factor of 50.

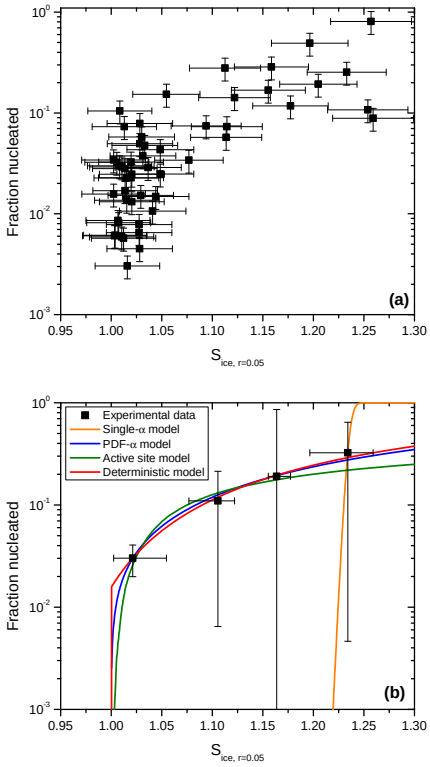

Figure A.4: Fraction of particles nucleated as a function of $S_{\mathrm{ice,r=0.05}}$ for illite. Panel (**a**) shows the nucleated fraction for the individual experimental results. The y-error was calculated from the uncertainty in the value of $\bar{D}_g$. The x-error represents the uncertainty in $S_{\mathrm{ice,r=0.05}}$. Panel (**b**) shows the average nucleated fraction calculated for four size bins. The range of the data points in each bin is given as the horizontal error and data points represent the average of the $S_{\mathrm{ice,r=0.05}}$ values within each bin. The y-error bar in panel (**b**) represents the 95 % confidence interval of the average nucleated fraction. Fits are shown for the single-α, pdf-α, active site, and deterministic schemes. The surface area was assumed to be the geometric surface area multiplied by a factor of 50.

Appendix B

Fitting PBAP Data

Fraction frozen plots from Section 5.4 above are replotted here using a linearly scaled ordinate axis. Also shown are the fitting results from each of the schemes investigated along with the fitting results plotted on a linearly scaled ordinate axis. Finally, the distributions of particles per drop measured in the freezing experiments is plotted for each of the species studied.

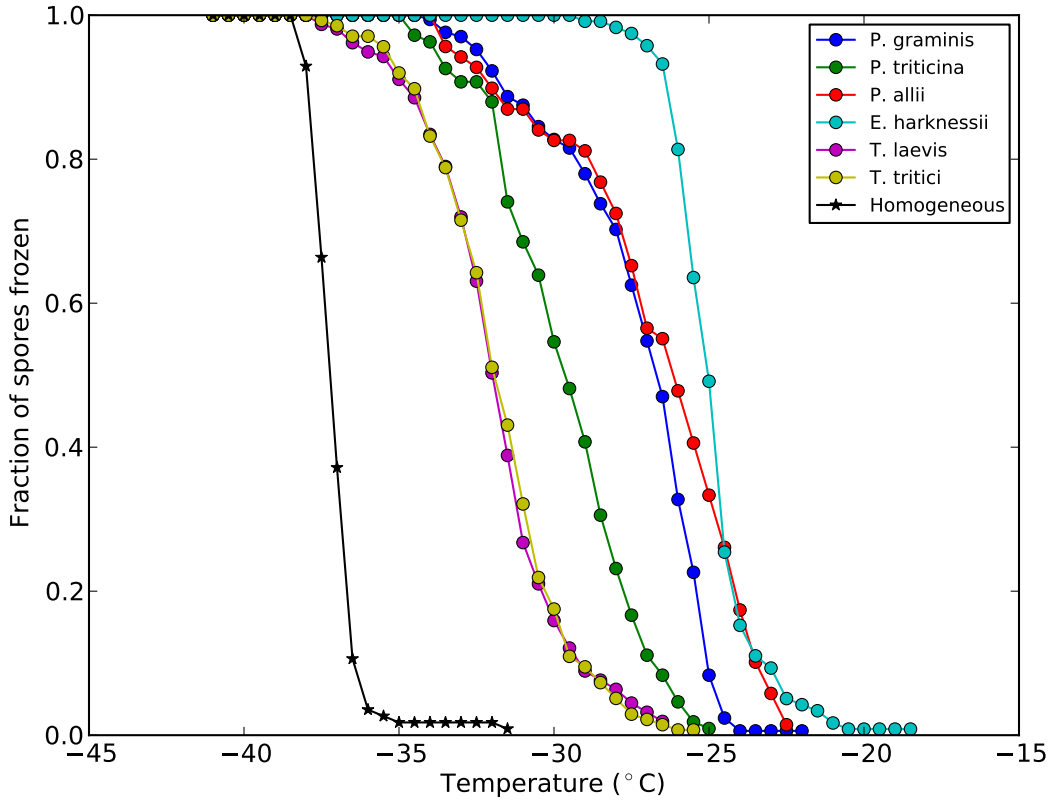

Figure B.1: Fraction of spore containing drops frozen calculated from immersion freezing results for all fungal spores studied plotted on a linear scale.

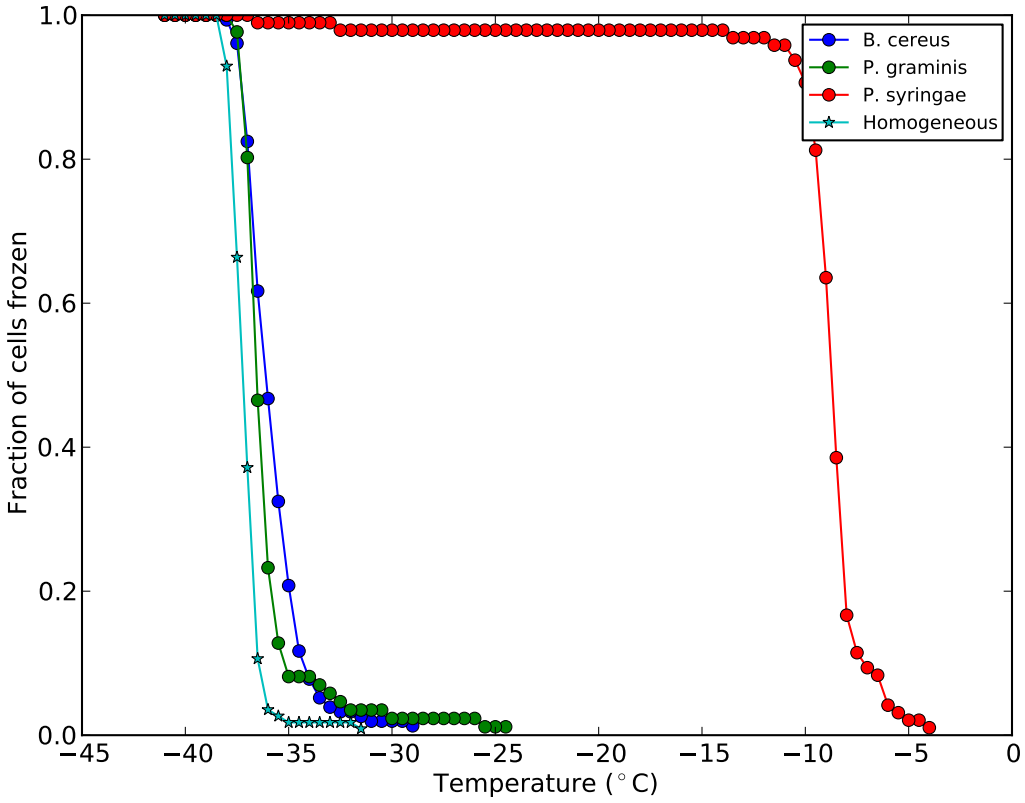

Figure B.2: Fraction of bacteria containing drops frozen calculated from immersion freezing results for all bacteria studied plotted on a linear scale.

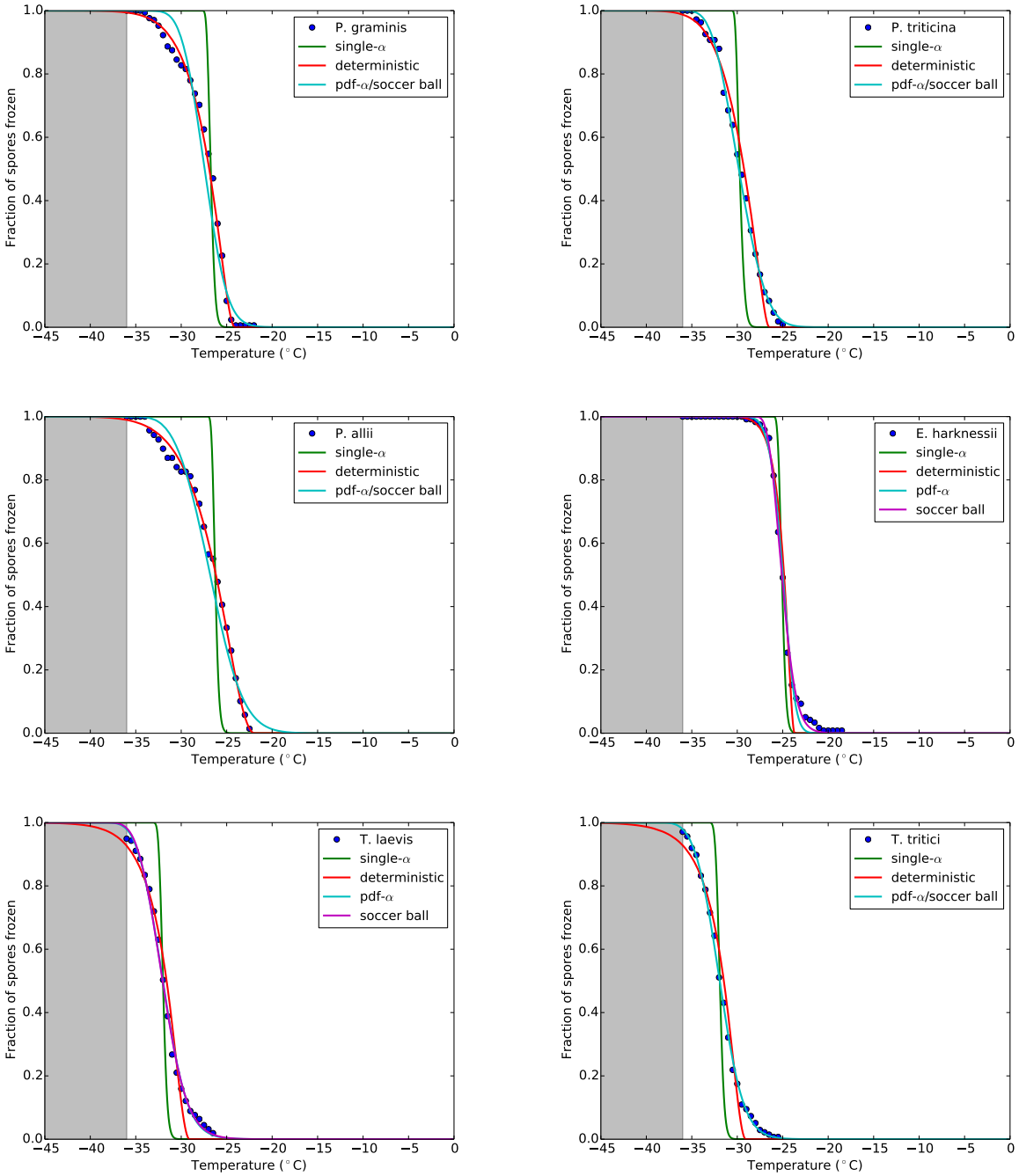

Figure B.3: Fit results for all fungal spores studied plotted on a linear scale. The shaded region represents the region where homogeneous freezing was observed and where fits to the experimental data were not considered. Experimental freezing data is shown as filled circles, while best fits are shown as solid lines for each of the four schemes studied.

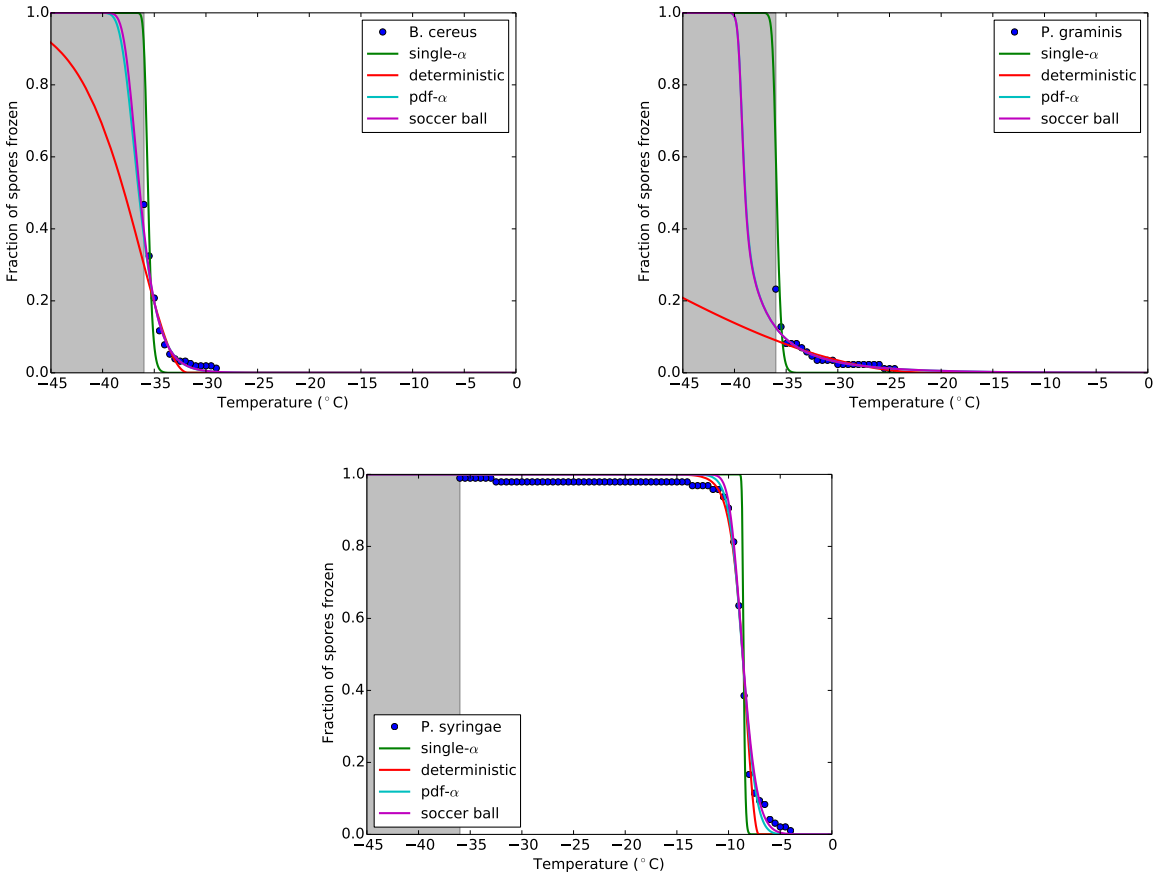

Figure B.4: Fit results for all bacteria studied plotted on a linear scale. The shaded region represents the region where homogeneous freezing was observed and where fits to the experimental data were not considered. Experimental freezing data is shown as filled circles, while best fits are shown as solid lines for each of the four schemes studied.

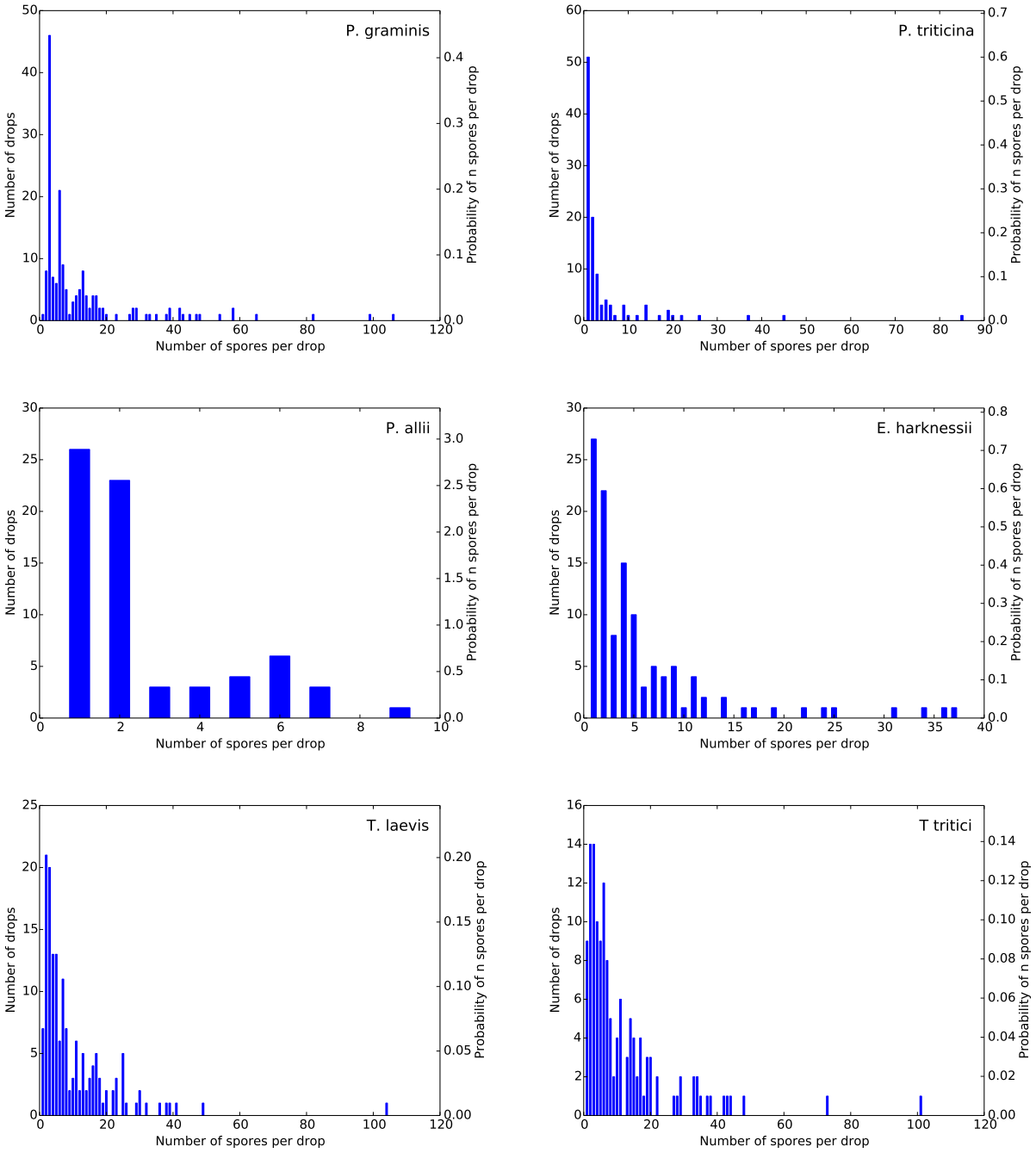

Figure B.5: Distribution of spores per drop calculated for each of the fungi studied. The left ordinate shows the individual number of drops observed as a function of the number of spores per drop. The right ordinate shows the fraction of drops containing n spores per drop. This corresponds to $P(n)$ from Eq. (5.1), (5.6) & (5.8).

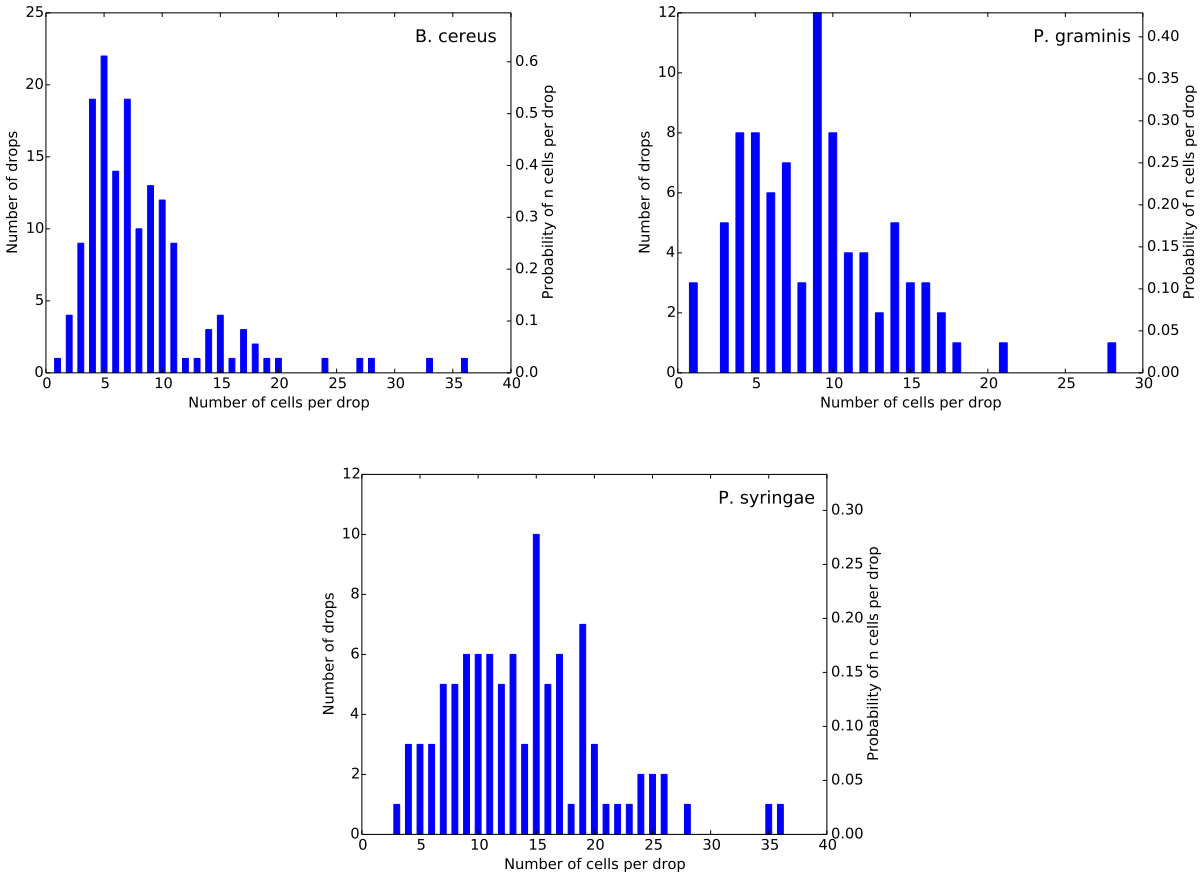

Figure B.6: Distribution of bacteria per drop calculated for each of the species studied. The left ordinate shows the individual number of drops observed as a function of the number of bacteria per drop. The right ordinate shows the fraction of drops containing n bacteria per drop. This corresponds to $P(n)$ from Eq. (5.1), (5.6) & (5.8).

Table B.1: Fitting results for the single-α scheme for all species studied

Particle Type	Species	α	WSSR	χ^2_{red}
Fungi	*P. graminis*	75.7°	681.70	25.248
	P. triticina	83.9°	675.19	32.152
	P. allii	73.9°	992.15	38.160
	E. harknessii	71.3°	263.13	7.739
	T. laevis	92.8°	560.61	31.145
	T. tritici	92.6°	567.06	28.353
Bacteria	*B. cereus*	105.2°	105.07	8.083
	P. graminis	106.7°	137.63	6.256
	P. syringae	35.0°	435.58	6.914

Table B.2: Fitting results for the pdf-α scheme for all species studied.

Particle Type	Species	μ_α	σ_α	WSSR	χ^2_{red}
Fungi	*P. graminis*	85.3°	6.4°	179.40	6.900
	P. triticina	87.8°	6.5°	21.57	1.079
	P. allii	79.7°	7.9°	126.86	5.075
	E. harknessii	73.1°	2.7°	52.38	1.587
	T. laevis	104.5°	10.0°	14.51	0.853
	T. tritici	104.1°	9.7°	5.56	0.293
Bacteria	*B. cereus*	127.1°	14.2°	11.43	0.953
	P. graminis	199.7°	44.0°	3.90	0.186
	P. syringae	41.2°	3.9°	175.81	2.836

Table B.3: Fitting results for the deterministic scheme for all species studied

Particle Type	Species	$A_1\,(\mathrm{cm}^{-2})$	$A_2\,(^\circ\mathrm{C})$	WSSR	χ^2_{red}
Fungi	*P. graminis*	1506.95	24.07	22.41	0.862
	P. triticina	3416.80	26.45	71.04	3.552
	P. allii	1504.41	21.93	32.04	1.282
	E. harknessii	11450.8	23.68	105.69	3.203
	T. laevis	1916.86	29.08	112.51	6.618
	T. tritici	1789.52	29.05	101.07	5.319
Bacteria	*B. cereus*	15971	31.70	30.37	2.531
	P. graminis	420.14	20.71	10.05	0.478
	P. syringae	263390	7.06	198.93	3.209

Table B.4: Fitting results for the soccer ball scheme for all species studied.

Particle Type	Species	n_{site}	μ_α	σ_α	WSSR	χ^2_{red}
Fungi	*P. graminis*	1	85.3°	6.4°	179.40	7.176
	P. triticina	1	87.8°	6.5°	21.57	1.135
	P. allii	1	79.7°	7.9°	126.86	5.286
	E. harknessii	100000000	108.3°	8.3°	29.46	0.921
	T. laevis	2	109.3°	11.2°	14.26	0.891
	T. tritici	1	104.1°	9.7°	5.56	0.309
Bacteria	*B. cereus*	1298	168.7°	19.2°	10.08	0.916
	P. graminis	5	236.0°	49.0°	3.88	0.194
	P. syringae	98779108	87.4°	9.5°	173.12	2.838